Experimental Investigation of Charge Transport and Heat Dissipation in Atomic-Scale Junctions

by

Woochul Lee

A dissertation submitted in partial fulfillment
of the requirements for the degree of
Doctor of Philosophy
(Mechanical Engineering)
in the University of Michigan
2014

Doctoral Committee:

Associate Professor Pramod Sangi Reddy, Chair
Professor Cagliyan Kurdak
Assistant Professor Xiaogan Liang
Professor Edgar Meyhofer

© Woochul Lee 2014
All Rights Reserved

Dedicated to my parents, sister, and wife for their endless love and trust.

Acknowledgements

I started my graduate study with a dream of achieving goals, curiosity, and a little bit of fear. Over the past five and a half years, I have been fortunate to work with excellent mentors and coworkers. Without them, I would not have achieved my goals at the University of Michigan.

First of all, I am indebted to my advisor, Prof. Pramod Reddy, for providing me an opportunity to work with him and teaching me the value and process of research. His passion for research inspired me and I was able to pursue challenging and important research questions. His eagerness to answer big questions in the field influenced me and changed my way of looking at research. Without his guidance, I would not have found a fun and rewarding moment in the research. I appreciate all the time he spent teaching me to become a better writer and presenter.

I am thankful to Prof. Edgar Meyhofer for his valuable advice when I was frustrated with being stuck on numerous research problems during my graduate study. He taught me how to deal with these problems and how to enjoy the research process. He also provided me valuable career advice. I thank all my dissertation committee members for their support and advice.

I am grateful to have worked with excellent collaborators. Dr. Kyeongtae Kim taught me Scanning Thermal Microscopy and various experimental skills. From the moment that we worked together, passionate discussions and debates have continued. I have enjoyed our discussions and debates, and I strongly believe that our discussions have made me a better researcher by deepening my thinking process and encouraging me to explain my ideas coherently. I would like to extend my thanks to my collaborators, Prof. Juan Carlos

Cuevas, Prof. Fabian Pauly, Wonho Jeong, Dr. Youngsang Kim, and Linda Zotti for insightful discussions related to my research.

I was fortunate to interact with Prof. Reddy's group members. Thanks to them, I enjoyed working in the laboratory. I would like to express thanks to Aaron Tan, Seid Sadat, Yi Jie Chua, Yashar Ganjeh, Bai Song, Dakotah Thompson, Anthony Fiorino, Longji Cui, and Ahmet Mazacioglu.

I would like to thank my family for their endless love. My parents and my sister supported me and gave me courage to keep moving forward throughout my life. Finally, without my wife, Juliana, I would have not finished my Ph.D. She always supported me and inspires me to be a better person.

Table of Contents

List of Figures

Abstract

Atomic-scale junctions, which comprise a single-molecule or a chain of atoms bridging two metal electrodes, hold great potential for the advancement of technology. These junctions are believed to offer a range of unique properties for creating novel technological applications because quantum mechanical effects persist even at room temperature.

I first describe the design and specifications of a custom-made scanning tunneling microscope that enabled the creation of mechanically stable single-molecule junctions at room temperature. With this instrument, I experimentally investigated charge transport in a series of single-molecule junctions, created by trapping single-molecules of hexanedithiol/octanedithiol/decanedithiol between gold electrodes. My results show that single-molecule junctions can be stably trapped for durations in excess of one minute, at least two orders of magnitude longer than what previous work had demonstrated. Next, I experimentally identified the low-bias conductance of single-molecule junctions using statistical analysis and found that the low-bias conductance exponentially decreases with increasing the length of alkanedithiol molecules. I also performed transition voltage spectroscopy in these alkanedithiol single-molecule junctions to determine the energetic separation between the Fermi level and the frontier molecular orbital. Experimental results confirmed that the energetic separation between the Fermi level and the frontier molecular orbital is independent of the length of the alkanedithol molecules.

Subsequently, I investigated heat dissipation in atomic-scale junctions resulting from charge transport. Toward this goal, stiff scanning tunneling probes with an integrated nanoscale-thermocouple at the tip are developed. Using this custom-fabricated probe with the scanning tunneling microscope break junction technique, I stably formed Au-Benzenediamine-Au junction, Au-Benzenediisonitrile-Au junction, and Au-Au atomic junctions and measured heat dissipation in the electrodes of atomic-scale junctions with the integrated nanoscale-thermocouple at the tip of the probe. These measurements show that heat dissipation in the electrodes of molecular junctions, whose electronic transmission characteristics are strongly dependent on energy, is asymmetric (that is, heat dissipation in the electrodes is unequal). In contrast, Au-Au atomic junctions, whose electronic transmission characteristics show weak energy dependence, do not exhibit appreciable asymmetry in their heat dissipation. I found that experimental results are consistent with the Landauer formalism for heat dissipation.

Chapter 1

Introduction

1.1 Molecular Electronics

While the semiconductor industry is continuing to reduce the size of electronic circuit elements, use of individual organic molecules or an assembly of organic molecules with electrodes (typically metals) to develop a hybrid device can be an additional promising approach toward realizing the ultimate smallest scale of nanoelectronics. The field that focuses on charge and thermal transport properties of the latter subject is *Molecular Electronics* [1]. To be more specific, the field of molecular electronics aims to understand charge and thermal transport properties in molecular junctions such as single-molecule junctions and multiple-molecule junctions, as depicted in Figure 1.1. The length of molecules typically ranges from 1 nm to 10 nm. In this dissertation, when I deal with short molecules whose sizes are just about 1 nm, I will use the terms molecular junctions and atomic-scale junctions interchangeably.

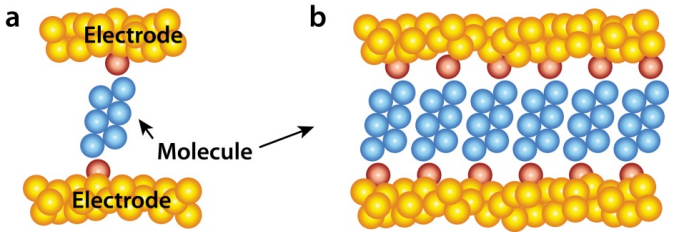

Figure 1.1 Illustration of molecular junctions. (a) Single-molecule junction where a single molecule is bridged between two electrodes (typically metal electrodes). (b)Multiple-molecule junction where an assembly of molecules is bridged between two electrodes (typically metal electrodes).

Molecular electronics is one of the most promising fields in nanotechnology and nanoscience since unique transport properties resulting from quantum mechanical effects can be employed for creating novel technological applications such as energy conversion devices, electronic devices, and sensors [2-4]. Molecular electronics is of great importance not only from the fundamental science point of view but also from the technological point of view. From the fundamental science point of view, molecular electronics explores charge and thermal transport at atomic and molecular length scale, where charge and thermal transport properties are fundamentally different from those properties in bulk materials and, more specifically, the underlying physics is dominated by quantum mechanical effects [2,5]. However, at the current stage fundamental transport properties at atomic and molecular scales are not well understood and numerous interesting and important fundamental questions remain to be answered [6]. Therefore, molecular electronics has gained increasing attention as an ideal platform to understand and control fundamental transport properties at the molecular and even atomic scale [1].

From the technological point of view, molecular electronics has several advantages. First, the size of molecules used to create molecular electronic devices is 1 nm or a few nm, the smallest limit of electronic devices. Although currently molecular electronics might seem far away from practical realization of a technology, future technological advances will almost certainly shrink the device dimensions to the single-digit nanometer regime. Therefore, understanding charge and thermal transport in atomic-scale junctions, which are approximately one nanometer in size, is critical for developing and optimizing future technologies. In principle, an almost unlimited number of molecular structures could be conceived and potentially synthesized. Careful understanding and engineering the

properties of molecules, which are the functional parts in molecular electronic devices, can open a tremendous number of opportunities regarding novel electronic functions and tailored transport properties. One can also utilize the various electrical, mechanical, optical, and thermal properties of molecular junctions resulting from the nanometer scale effects and the quantum mechanical effects to create novel devices that cannot be realized in conventional solid state devices [1]. It has also been suggested that molecule-based thermoelectric energy conversion devices and memristors—non-volatile memory which is based on resistance switching—could have great potential for practical devices [4]. Furthermore, understanding charge and thermal transport at the atomic or molecular scale will certainly help researchers understand and design complex systems through a bottom-up approach.

The history of the molecular electronics field can be traced back to the 1970s. In 1971, the electrical conductivity was experimentally measured on monolayers of cadmium salts of fatty acid $CH_3(CH_2)_{n-2}COOH$ of various molecular lengths. The study showed that the conductivity exponentially decreased as molecular lengths increased, suggesting that the mechanism of charge transport through organic monolayers is electron tunneling [7]. In 1974, an electronic circuit component using a single organic molecule, a rectifier, was proposed by Aviram and Ratner [8], and this pioneering theoretical work is considered the first work at the single-molecule level.

Although interesting theoretical questions were investigated after Aviram and Ratner's work, there were no experimental tools available to test and verify their ideas. In 1981, the Scanning Tunneling Microscope (STM) was invented by Gerd Binning and Heinrich Rohrer [9]. The STM has enabled researchers to obtain topography at individual-atom

level as well as manipulate individual atoms. Consequently, STM has had tremendous impacts in various nanotechnology fields. Since its invention, STM has offered great opportunities to experimentally examine single molecules and study charge transport properties in single-molecules. Furthermore, several experimental tools and techniques to interface single-molecules or an assembly of molecules with metal electrodes have been developed [10-14]. These experimental tools and techniques are the Mechanically Controllable Break Junction (MCBJ) technique [10], the Scanning Tunneling Microscope Break Junction (STMBJ) technique [11], the Electromigrated Break Junction (EBJ) technique [12], and the Contact Probe-Atomic Force Microscope (CP-AFM) technique [14]. I will describe some of these experimental techniques in more detail later in this dissertation. Since these novel experimental tools and techniques have been introduced to the molecular electronics field, charge transport properties through single-molecules or multiple molecules in contact with metal electrodes have been extensively investigated through experimentation. At the same time as these technological advances have been achieved in the experimental side, computations and theories to understand the charge and thermal transport have also significantly advanced [1,15]. Contributions from both theoretical and experimental advances have enabled researchers to study charge and thermal transport characteristics in molecular junctions. I will describe a theoretical framework to understand charge and thermal transport properties in molecular junctions and discuss some of the interesting experimental and theoretical studies in Chapter 2.

1.2 QUESTIONS ADDRESSED IN THE DISSERTATION

Understanding charge and thermal transport in molecular junctions is crucial for uncovering the underlying physics and for realizing molecular electronic devices at the

ultimate smallest length scale. Numerous aspects of charge transport in molecular junctions have been investigated using the several tools and techniques mentioned above. Each technique has distinct advantages and disadvantages, and is particularly suitable for specific studies. Among various techniques, the Scanning Tunneling Microscope Break Junction (STMBJ) technique is ideal for both charge and thermal transport studies because the STM tip and the substrate are thermally well isolated, and this technique is able to easily create a large number of single-molecule junctions. However, the inability to stably trap molecular junctions for sufficiently long duration using the STMBJ technique has prevented further investigations of charge transport in molecular junctions and, more importantly, has posed a barrier to enable experimental investigations of energy dissipation and thermal conduction in molecular junctions because of the even greater difficulties involved in the study of energy dissipation and thermal conduction. In order to overcome this experimental challenge, a new tool had to be developed to stably trap molecular junctions long enough. In Chapter 3, I will describe a custom-designed Scanning Tunneling Microscope capable of trapping molecular junctions for more than 1 minute, at least two orders of magnitude more stable in trapping time than what other studies have previously demonstrated.

One of many questions that molecular electronics community is trying to address is how to experimentally characterize the detailed electronic structure of molecular junctions. Recently, Transition Voltage Spectroscopy (TVS), an experimental technique developed by Beebe *et al*., has been introduced to estimate the energetic separation between the Fermi level and the closest molecular orbital [16,17]. TVS has attracted many researchers because it is a relatively simple method—the only required information is the current-

voltage (*I-V*) characteristics of molecular junctions. However, TVS has been leveraged nearly exclusively for an assembly of asymmetric molecules [16-18] or for single-molecule junctions at low temperatures (4.2 K) [19,20]. To elucidate the energetic separation between the Fermi level and the closest molecular orbital for symmetric single-molecule junctions at room temperature, I experimentally studied TVS on symmetric alkanedithiol single-molecules with different chain lengths interfaced between gold metal electrodes at room temperature, and this study will be discussed in Chapter 3.

In conjunction with charge transport, heat (energy) dissipation in molecular junctions is an important problem since heat dissipation is ubiquitous in the charge transport process. While charge transport in atomic and molecular junction has been actively studied over the past decade [10,11,20,21], research on heat dissipation in such junctions has only recently begun [22-24]. In one of the recent studies, the local effective temperature of single-molecule junctions was indirectly inferred from the bond strength of the junction, and the results showed that as voltage bias increases the local effective temperature of the junction increases but then decreases at some point [22]. This temperature decrease is attributed to the electron-electron interaction. Another study using Surface Enhanced Raman Spectroscopy (SERS) to determine the effective temperatures for the vibrational modes as well as the electrons showed that the effective temperature can exceed a couple of hundred degrees centigrade as voltage bias is applied only up to a few hundreds of millivolts [24]. However, these experimental studies were not able to experimentally prove or test the heat dissipation characteristics that the Landauer model [25,26], a well-known quantum transport theory, predicts.

One of the major unresolved questions in the molecular electronics and nanoscale thermal transport community pertains to the nature of heat dissipation in atomic-scale junctions, specifically where heat is dissipated in atomic-scale junctions. Answering this question will provide new insight into fundamental energy transport characteristics in atomic-scale junctions. This insight will significantly contribute to not only the field of molecular electronics but also the field of nanoscale thermal transport, where understanding of energy dissipation in molecular electronic devices or mesoscopic devices is essential. However, this question was unanswerable owing to the lack of experimental tools 1) to stably trap the atomic-scale junctions and 2) to directly measure local temperature changes resulting from the heat dissipation. I will present my experimental effort to overcome the experimental challenges in Chapter 3 and Chapter 4 and discuss my experimental results on heat dissipation properties in atomic-scale junctions in Chapter 4. I will also describe why unique heat dissipation properties arise in atomic-scale junctions in Chapter 4.

1.3 ORGANIZATION OF THE DISSERTATION

In this dissertation, I will present experimental work on the study of charge transport and heat (energy) dissipation characteristics in atomic-scale junctions and describe nanoscale experimental tools I developed to enable the aforementioned challenging study. This dissertation is organized as followings.

In Chapter 2, I will discuss the theoretical framework to describe charge and energy transport in atomic and molecular junctions. I will also briefly introduce recent advances of experimental tools and techniques to study charge and energy transport properties in

such junctions. Then, I will review past experimental and computational studies to better understand the charge and energy transport in atomic and molecular junctions.

In Chapter 3, I will first describe a custom-built Scanning Tunneling Microscope (STM) operating at room temperature and under high-vacuum condition to enable the creation of stable single-molecule junctions. I will then present my experimental study using the custom-built STM on charge transport properties such as the electrical conductance and on characterizing electronic structure, such as energetic separation between the Fermi level and the closest molecular orbital, for various symmetric single-molecule junctions—hexanedithiol, octanedithiol, and decanedithiol bridging two gold metal electrodes at room temperature.

In Chapter 4, I will describe experimental study to understand the nature of heat dissipation in atomic-scale junctions, specifically where heat is dissipated in atomic-scale junctions. I will first describe custom-fabricated nanoscale-thermocouple integrated scanning tunneling probes. These probes are employed both to create atomic and molecular junctions between gold electrodes and to measure the local heat dissipation in the electrode of atomic-scale junctions as charge transports through the atomic and molecular junctions. I will then discuss experimental results of heat dissipation for three kinds of atomic-scale junctions, Au-1,4-Benzenediisonitrile-Au junctions, Au-1,4-Benzenediamine-Au junctions, and Au-Au atomic junctions. I will also compare experimental results with theoretical calculations based on the Landauer model and density functional theory, and explain the relationship between heat dissipation properties (symmetric and asymmetric heat dissipation) of atomic-scale junctions and the electronic

structure of atomic-scale junctions. I will conclude with a description of detailed experimental methods and characterizations of the custom-fabricated probes.

In Chapter 5, I will present the key findings of this dissertation and discuss some of interesting and important future work that can be extended from the work described in this dissertation.

Chapter 2

Charge and Energy Transport Properties of Single-Molecule Junctions

Reproduced with permission from *Annual Review of Heat Transfer*
Woochul Lee, Bai Song, and Pramod Reddy, *Annual Review of Heat Transfer*, 2013, Vol. 16, 259-285 [27]. Copyright 2013, Begell House, Inc.

2.1 INTRODUCTION

Unusual charge and energy transport phenomena—with important technological applications—are expected to arise in molecular junctions that are created by trapping short nanometer-sized organic molecules between inorganic electrodes [5,28,29]. A variety of interesting phenomena such as negative differential electric resistance [30,31], rectification of electric current [32-34], switching [35,36], and field-effect gating [20] have all been observed in specifically tailored molecular junctions and present great potential for advancing electronic applications. More interestingly, recent computational studies [37-41] have also suggested that it should be possible to create junctions with large thermoelectric efficiencies using suitably tailored organic molecules.

In fact, using the techniques of organic chemistry one can synthesize millions of molecules with different molecular structures. These organic molecules can in principle be used to build a huge variety of electronic devices and materials with a range of desirable properties. However, before such devices and materials are created, it is

necessary to understand the charge and energy transport properties of nanometer-sized molecular junctions. In this chapter, we will first provide a brief description of the Landauer approach [26,42] that is widely used to describe charge and energy transfer in nanoscale molecular junctions. Further, we will describe some of the recent computational work which suggests that molecular junctions can be tailored to achieve large thermoelectric efficiencies. In addition to this, we will also present past theoretical and computational work on thermal transport in single molecule junctions and single polymer chains. Subsequently, we will describe the experimental techniques currently available to probe the thermoelectric properties (both the Seebeck coefficient and the electrical conductance) of single molecule junctions and describe some of the interesting results obtained from such studies. Finally, we will discuss the challenges in experimentally probing thermal transport in single molecule junctions and suggest some potential approaches to overcome this challenging instrumentation problem.

2.2 Theoretical Framework for Describing Charge and Energy Transfer in Molecular Junctions

The Landauer model has been widely used to characterize charge and heat transfer in the ballistic regime [26]. Here, we will first introduce the formalism used to describe the electrical response of molecular junctions to an applied voltage differential (Figure 2.1a). We will also extend this analysis to describe the open circuit voltage of junctions with temperature differentials applied across them (Figure 2.1b). Finally, we present the formalism used to describe heat currents in molecular junctions (Figure 2.1c). We note that the description provided here is relatively brief, since a more detailed explanation of the Landauer model is available in many review articles [5,43] and textbooks [26,44].

In order to understand the electrical conductance and Seebeck coefficient of molecular junctions, it is instructive to visualize the electronic structure of a molecule before and after it makes contact with electrodes. When a single molecule is not interacting with its surroundings, its energy levels are discrete. Further, if the molecule is in its ground state, all the energy levels below a certain orbital called the lowest unoccupied molecular orbital (LUMO) are occupied and all the orbitals above the highest occupied molecular orbital (HOMO) are empty. When a molecule is in contact with two metal electrodes as shown in Figure 2.2a, the energy levels in the spatial location of the molecule realign and broaden due to interaction with the electrodes [26]. In such a junction, all the energy levels below the equilibrium chemical potential (E_f) of the electrodes are occupied and all the energy levels above are empty.

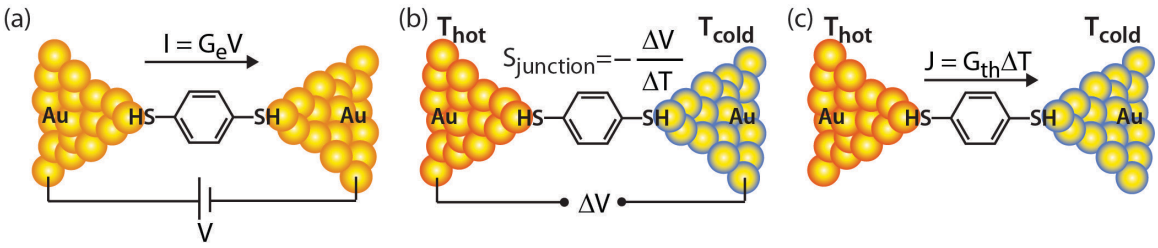

Figure 2.1 (a) Single molecule junction under an applied voltage bias. (b) A single molecule junction with a temperature differential applied across it resulting in a voltage differential. (c) The heat current in a molecular junctions due to applied temperature differential.

If a voltage bias (V) is applied between the electrodes (as shown in Figure 2.2b), a non-equilibrium scenario arises where the left and right electrodes are at different chemical potentials μ_L and μ_R, respectively. For the configuration shown in Figure 2.2b, $\mu_L = E_f + eV$ (e is the charge of an electron) and $\mu_R = E_f$. In such a scenario, the electron

distributions in the left and the right electrodes are given by the Fermi-Dirac distributions $f_L(E)$ and $f_R(E)$,

$$f_{L/R} = \left[1 + \exp\left(\frac{E - \mu_{L/R}}{k_B T_{L/R}}\right)\right]^{-1} \tag{2.1}$$

where E is any given energy, k_B is the Boltzmann constant and T_L, T_R are the temperatures of the left and right electrodes, respectively. The distributions $f_L(E)$ and $f_R(E)$ in the two electrodes are usually different due to differences in temperature or voltage. At any given energy, E, if the local density of states in the molecule is $D(E)$, then the left electrode tries to maintain on the average $2D(E)f_L(E)$ electrons, whereas the right electrode tries to maintain on the average $2D(E)f_R(E)$ electrons, the factor of two arising from electron spin degeneracy. This difference in agenda between the left and right electrodes leads to a flow of electrons in the metal-molecule-metal junction.

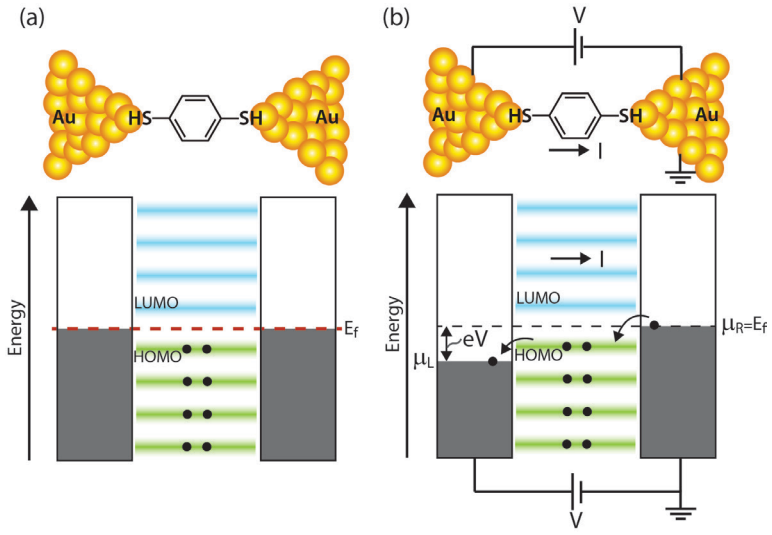

Figure 2.2 (a) A molecular junction at zero bias is shown along with the electronic structure of the junction (b) A junction under a voltage bias (V). An electrical current flows from the left to the right electrodes through the molecular junction.

2.2.1 Electrical Conductance of Molecular Junctions

In general the electric current (I) from the left to the right electrode (Figure 2.1a, Figure 2.2b), through a molecular junction, can be described in the Landauer formalism[26] by the following expression:

$$I = \frac{2e}{h} \int_{-\infty}^{\infty} \tau(E)\left(f_L - f_R\right) dE \,. \tag{2.2}$$

Here, $\tau(E)$ is the energy-dependent transmission function, which assumes values between zero and one, h is the Planck constant and e is the charge of an electron. In general, $\tau(E)$ is dependent on several other variables such as the applied bias [45], magnetization of the electrode s[46,47], and electric fields that may be present due to a gate electrode [26,48]. Furthermore, the transmission function is also sensitive to the details of molecular structure [11,49], chemical composition of the electrodes [50], and the contact chemistry [51]. To simplify notation, such dependencies are not explicitly shown in Eq. (2.2).

When the applied bias voltage is small, Eq. (2.2) can be approximated[26] to obtain

$$I \sim \frac{2e^2}{h} \tau\left(E = E_f\right) V \,, \tag{2.3}$$

where $\tau(E=E_f)$ is the transmission function at the chemical potential. This equation suggests that the electrical conductance (G_e) of a molecular junction is $(2e^2/h) \times \tau(E=E_f)$. It can be seen that the key to achieving a large electrical conductance is to have a large transmission function at the chemical potential.

2.2.2 Thermoelectric Properties of Molecular Junctions

The Seebeck coefficient of a molecular junction is defined as the ratio of the open circuit voltage across a junction ($\Delta V = V_L - V_R$, where V_L and V_R are the voltages of the left and right electrodes respectively) to the temperature differential ($\Delta T = T_L - T_R$) applied across the junction,

$$S_{junction} = -\frac{\Delta V}{\Delta T}. \tag{2.4}$$

The Seebeck coefficient of the junction can also be related to the transmission function by the following expression[52,53],

$$S_{junction} = -\frac{\pi^2 k_B^2 T}{3|e|} \frac{\partial \ln[\tau(E)]}{\partial E}\bigg|_{E=E_f} . \tag{2.5}$$

This suggests that a large Seebeck coefficient is achieved if the derivative of the transmission function at the chemical potential is large. We note that the expression given in Eq. (2.5) is obtained from Eq. (2.2) by assuming that the applied temperature differential is very small ($\Delta T \to 0$). For large applied temperature differentials, the resultant thermoelectric voltage can be obtained directly using Eq. (2.2). Although the Landauer approach described above is convenient and provides computational simplicity, it has some inadequacies resulting from its inability to account for electron-electron interactions in more detail than that possible under a mean-field approximation. These are described in more detail in a recent review by Dubi and Di Ventra [5].

2.2.3 Thermal Transport in Molecular Junctions

Thermal energy can be transported across molecular junctions both by electrons and phonons and can be described in the Landauer formalism. The heat current due to electrons ($J_{electrons}$), for a small temperature bias ($\Delta T \to 0$), can be represented by [25,54]

$$J_{electrons} = \frac{2}{h}\int_{-\infty}^{\infty}\left(E - E_f\right)\tau\left(E\right)\left(f_L - f_R\right)dE\,. \tag{2.6}$$

Here f_L and f_R again represent the Fermi-Dirac distributions of the left and right electrodes, respectively. The heat current due to phonons ($J_{phonons}$) can be represented using the following expression in the Landauer formalism [55],

$$J_{phonons} = \int_{0}^{\infty}(h\upsilon)\tau(\upsilon)\left(g_L - g_R\right)d\upsilon \tag{2.7}$$

where $\tau(\upsilon)$ is the frequency-dependent transmission function for phonons and can be obtained using atomistic Green's function techniques [55], υ is the frequency of the phonon, and g_L, g_R are the Bose-Einstein distributions of the left and the right electrodes respectively, and are given by

$$g_{L/R} = \left[\exp\left(\frac{h\upsilon}{k_B T_{L/R}}\right) - 1\right]^{-1}, \tag{2.8}$$

where h is the Planck's constant and T_L, T_R represent the temperatures of the left and right electrodes respectively.

The above discussion provides a simple framework to describe thermoelectric and thermal transport phenomena in molecular junctions. However, obtaining the energy-dependent transmission function of electrons, and the frequency-dependent transmission

function of phonons, is computationally challenging and is usually performed under several approximations [26]. In the next section, we will describe some recent computational results that illustrate the promise of molecular junctions for energy conversion applications.

2.3 Computational Studies of Thermoelectric and Thermal Transport Properties of Molecular Junctions

It is well known that for achieving efficient thermoelectric energy conversion it is necessary to simultaneously achieve a large electrical conductance and Seebeck coefficient [42]. The efficiency of thermoelectric materials in converting heat into electrical energy is characterized by the figure of merit (ZT),

$$ZT = \frac{S^2 \sigma T}{k}, \tag{2.9}$$

where S is the Seebeck coefficient of the material, σ is the electrical conductivity and k is the thermal conductivity, which includes contributions to heat transport by both electrons and phonons.

An equivalent figure of merit can be defined for molecular junctions as

$$ZT = \frac{S^2 G_e T}{G_{th}}, \tag{2.10}$$

where G_e represents the electrical conductance, and G_{th} represents the thermal conductance of the molecular junctions. It is clear from the discussion in section 2.2 that a large figure of merit can be obtained by appropriately tuning the magnitude and the slope of the transmission function at the chemical potential.

2.3.1 Computational Study of Thermoelectric Effects in Molecular Junctions

Recently, various groups have computationally probed [37,39,40,56-58] the thermoelectric properties of molecular junctions and have described various tailored molecular systems where large values of the figure of merit can be potentially achieved. Here, we briefly summarize some of these results. Finch *et al.*[39] recently probed the thermoelectric properties of CSW-470-bipyridine molecule (Figure 2.3a) sandwiched between gold electrodes. By using density functional theory and a non-equilibrium Green's function (NEGF) formalism, they showed that the transmission function of the molecular junction could be tuned to have a large peak at the chemical potential by controlling the rotation of the side group about the C-C bond (see Figure 2.3a). Such a peak (Figure 2.3b) in the transmission function is predicted due to Fano resonances [59] that arise from the presence of degenerate energy levels in the molecular backbone and the side groups. The results from this work show that by controlling the orientation of the side group, with respect to the backbone of the molecule, it is indeed possible to achieve extremely large values of the figure of merit (>10, see Figure 2.3c). We note that, in this study, the contribution of phonons to thermal transport was neglected, resulting in an overestimation of the figure of merit. However, because the thermal conductance of molecular junctions is expected to be small (~10-100 pW/K, discussed in detail later), the results obtained in this work are not expected to change significantly even if the phononic contribution is included.

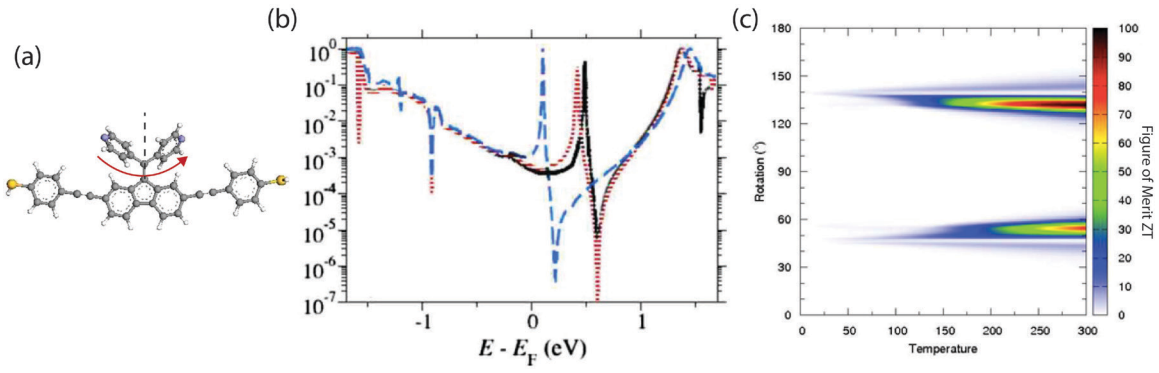

Figure 2.3 (a) A molecule with a side group that can rotate about the C-C bond connecting it to the backbone. (b) The transmission function as the side group is rotated. (c) The predicted values of the figure of merit (ZT) for various orientations of the side group at different temperatures. Reproduced with permission from [39] , Copyright 2009 by the American Physical Society

In addition to this work, Bergfield *et al.* [37] computationally studied thermoelectric effects in polyphenyl ether-based molecular junctions. Their studies suggested that the molecular junctions created by trapping polyphenyl ether molecules between gold electrodes demonstrate a sharp peak in the transmission function arising from quantum interference effects. Their results also suggest that large values of figure of merit ($ZT > 4$) can be accomplished in molecular systems.

In this context, it is important to note a theoretical prediction made by Mahan and Sofo [60] that suggests that a bulk material with a Dirac delta-shaped density of states very near to the chemical potential would result in an extremely large *ZT*, which according to them would represent the best thermoelectric material conceivable. However, subsequent studies [61] established the fact that while a Dirac delta-shaped density of states enables reversible operation of a thermoelectric device, the power output would be zero. Similar arguments also apply to molecular devices, where it has been shown that a Dirac delta-

shaped transmission function would enable the creation of a thermoelectric device operating at Carnot efficiency [62-64]. However, the power output of such a junction would be zero. This suggests that for operation at large powers, a sharp peak in the transmission function is not desirable. In fact, it is necessary to engineer the transmission function appropriately so as to maximize the power output. Recent work by Nakpathomkun *et al*. [65] and Karlstrom *et al.* [40] has elucidated this fact and is described below.

If the goal is to achieve maximum power output, the relevant limit is the Curzon-Ahlborn limit [66], which suggests that the maximum efficiency (η_{CA}) of a heat engine operating under conditions such that the power output is maximized is given by

$$\eta_{CA} = \frac{\eta_C}{2} + \frac{\eta_C^2}{8} + O\left(\eta_C^3\right) + \ldots \quad , \tag{2.11}$$

where η_C is the Carnot efficiency. In this context, Nakpathokun *et al.* [65] recently considered a molecular junction/quantum dot system where the transmission function is well approximated by a Lorentzian:

$$\tau(E) = \frac{(\Gamma/2)^2}{(E - E_o)^2 + (\Gamma/2)^2} \tag{2.12}$$

where Γ is the full width at half maximum of the transmission function and the E_o is the energy about which the Lorentzian is centered. From their analysis, they showed that the power output becomes zero when the Lorentzian is very sharp (i.e when $\Gamma \rightarrow 0$). Furthermore, they showed that the power output is maximized by appropriately choosing both Γ and the energetic separation between E_o and E_f (the chemical potential). In spite of such optimization, it was shown that transmission functions shaped as a Lorentzian

cannot be used to achieve operation at the Curzon-Ahlborn limit. This is because a Lorentzian transmission function does not effectively filter the flow of electrons due to the presence of a long low-energy tail which leads to an undesirable electric current in a direction opposite to that of thermoelectric currents (see Ref. [65] for more details).

In order to overcome this challenge, Karlstrom *et al.* [40] have suggested an ingenious approach which takes advantage of quantum interference in a two-level system where both the energy levels are located on the same side of the chemical potential (Figure 2.4a shows two energy levels above E_f) and are coupled to the electrodes with different parities. For such a system, they show that if the coupling strengths of the two energy levels to the electrodes differ by a factor of a^2, the transmission function takes the following functional form

$$\tau(E) = \Gamma^2 \left| \frac{1}{(E - E_f) + E_1 + i\Gamma} - \frac{a^2}{(E - E_f) + E_2 + ia^2\Gamma} \right|^2 . \qquad (2.13)$$

From this expression it is clear that, if $E_2 \approx a^2 E_1$, then the value of the transmission function is zero at E_f and is large for a finite range of energies above E_f (Figure 2.4b). Since this transmission function shows a sharp gradient at the chemical potential but has a finite width, it enables operation at large power outputs. In fact, detailed calculations given in Ref. [40] suggest that efficiencies can reach a value very close to the Curzon-Ahlborn limit (Figure 2.4c). In addition to proposing this model system, Karlstrom *et al.* [40] have also suggested the possibility of realizing such a two-level system via a zinc porphine system (Figure 2.4d) that is in contact with gold electrodes.

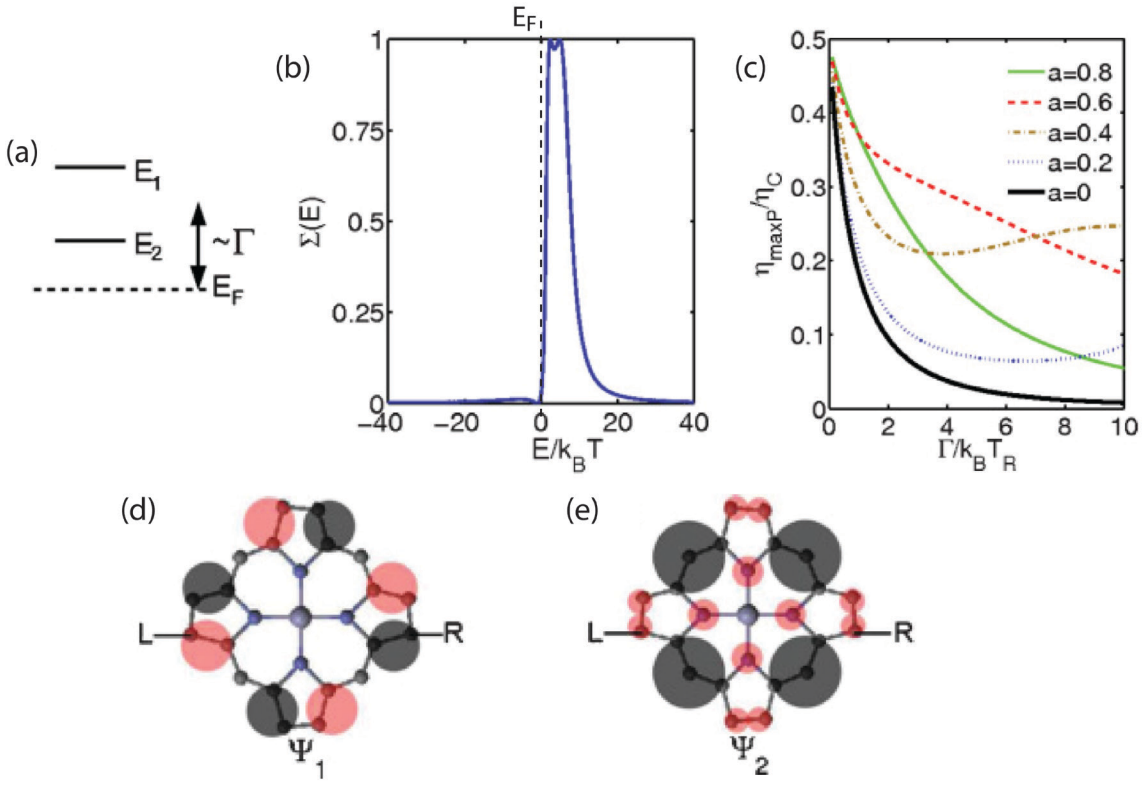

Figure 2.4 (a) A two-level system with both energy levels above the chemical potential. (b) The transmission function obtained for appropriately chosen values of $E_1 = 5.8k_BT$ and $E_2 = 1.47k_BT$ (T =300 K). (c) The efficiency of the device at maximum power output as a function of the coupling strength. (d, e) The wave functions of a zinc porphine molecular junction that could potentially be employed to obtain operation at high power outputs. Reproduced with permission from Ref. [40], Copyright 2011 by the American Physical Society.

The brief description of computational studies provided above represents a small sample of examples that highlight the interesting phenomena arising in molecular junctions. These studies clearly demonstrate that molecular junctions provide an ideal platform for the construction of nanoscale energy-conversion engines that approach the Carnot limit or the Curzon-Ahlborn limit. Experimental probing/demonstration of such engines would

provide deep insights into the nature of non-equilibrium processes and energy-conversion at the nanoscale.

2.3.2 Computational Study of Thermal Transport in Molecular Junctions

The study of heat transport in molecules/molecular junctions has its origins in the pioneering work of Fermi, Pasta and Ulam (FPU) [67] over half a century ago. By showing that a simple anharmonic one-dimensional (1D) chain of particles can be nonergodic, the FPU study implied the possibility of infinite thermal conductivity and has been extensively explored ever since. Here, we briefly summarize some important results. A detailed review on low-dimensional anomalous heat conduction is given by Lepri *et al*. [68].

Casher and Lebowitz [69] used a nonequilibrium statistical mechanics approach to show that the thermal conductance of a harmonic chain of particles with different masses is independent of the length, pointing explicitly to a divergent thermal conductivity. More recently, Lepri *et al*. [70,71] proposed via numerical simulations that the thermal conductivity of nonlinear 1D lattices could diverge as N^{β} where N is the number of lattice points ($N >> 1$) and the exponent β is ~0.4 for 1D lattices.

In addition to research on model systems, realistic systems such as molecules have also been studied. For example, Segal *et al*. [72] used a generalized Langevin equation approach to study the length dependence of thermal conductance in alkane molecular junctions. Their studies indicate an increase in the thermal conductance with increasing chain length for chains containing less than five carbon atoms (Figure 2.5a). However, for molecules with more than 10 carbon atoms, the calculated thermal conductance

remains essentially constant as the length goes up to 20 carbon atoms. Further, these trends were found to hold for a range of temperatures, i.e., 50 K, 300 K and 1000 K, the specific values of the conductance being tens of picowatts per Kelvin (pW/K). These results were also found to be relatively invariant even when the effect of electron-phonon coupling was considered [73].

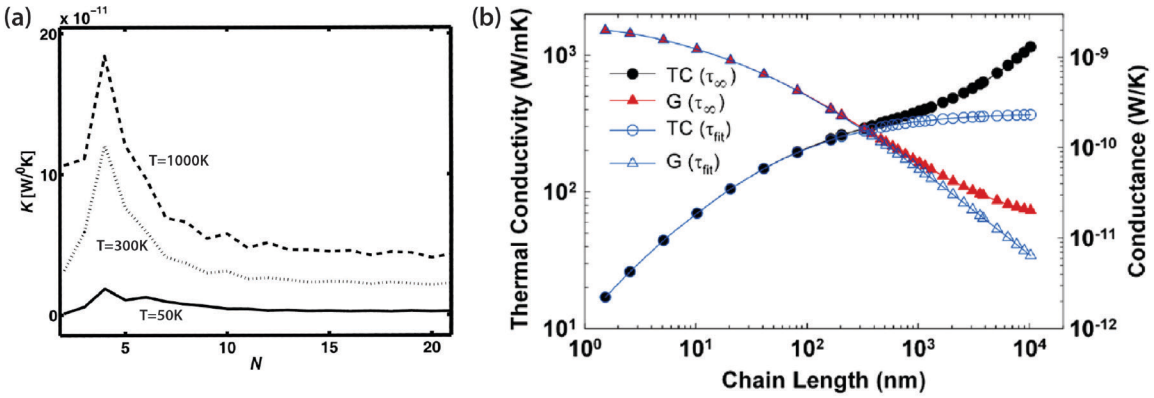

Figure 2.5 (a) The computed the thermal conductance for alkane chains of different lengths at different temperatures (b) The computed thermal conductance and the corresponding thermal conductivity for single-polyethylene chains of varying lengths. Reproduced with permission from: (a), Ref. [72], Copyright 2003 by the American Institute of Physics; (b), Ref. [74], Copyright 2008 by the American Physical Society.

In addition to studies on alkane molecular junctions, Henry and Chen performed equilibrium molecular dynamics simulations combined with Green-Kubo analysis to estimate the thermal conductivity of a single polyethylene chain (Figure 2.5b). Their results suggest that the thermal conductivity of a single chain could be three orders of magnitude larger than that of a typical bulk polymeric material, and even divergent in some cases [74]. This behavior was explained by invoking the phonon-phonon correlations existing in 1D lattices, which suppress the allowable scattering events in comparison to a 3D bulk material [75,76]. Their results were partially verified by

performing measurements on aligned polyethelyne fibers with diameters in the range of 50 -500 nm [77].

Sasikumar and Keblinski [78] studied heat transfer across molecular junctions formed by alkane chains covalently bonded to crystalline silicon. Their studies used nonequilibrium molecular dynamics and showed that straight chains that have all their constituents in a trans conformation have the highest thermal conductance. Further, they showed that as the number of gauche conformations (kinks) increases, the chain thermal conductance reduces, indicating that gauche conformations act as strong phonon scattering centers. The typical values of chain thermal conductance are tens of pW/K, in agreement with former results [72]. Their study also probed the differences in thermal conductance between a straight chain junction and a junction in a kinked configuration and found that junctions with straight chains have a significantly larger thermal conductance than junctions with kinked chains.

Another area of active study concerns heat generation and thermoelectric effects in molecular electronic devices. Understanding and controlling heat generation and flow in molecular junctions is of vital importance since local heating may cause structural instabilities undermining the junction integrity. One of the first studies of heating in current carrying molecular junctions was by Segal *et al*. [79] where they found that classical heat conduction theories would underestimate the local temperature raise in junctions. Later, Galperin *et al*. [73,80] proposed a unified description of heat generation and transport in junctions using a nonequilibrium Green's function formalism, allowing for a comprehensive and consistent investigation of the effects of different parameters.

Their studies indeed confirm that the temperature within a junction could exceed 1000 K even under small bias voltages (~0.5 V).

Recently, Ward *et al.* [24] have developed a surface-enhanced Raman spectroscopy-based experimental technique for probing the effective temperatures of the vibrational modes that are excited in molecular junctions during electron flow. Using this technique they probed the effective vibrational temperature, under an applied bias, for an aromatic and aliphatic molecule-based junction at a temperature of 80 K. Their results indeed suggest that the non-equilibrium temperature of vibrational modes could be substantially higher (~600 K) than the ambient temperature. In addition to these measurements they have also probed the effective temperature of the electrons, details of which can be found in Ref. [24]. Finally, the possibility of current-induced cooling was also discussed recently [81]. One proposed mechanism is the cooling of electrodes due to depletion of high-energy electrons, which subsequently leads to the cooling of molecules strongly coupled with the electrode. We note that experimental evidence of current-induced cooling has also been reported [82-84].

In addition to this, computational studies have also studied possible strategies to control the flow of heat. For example, Segal *et al*. [85,86] suggested that heat conduction through a molecular chain bridging two thermal reservoirs at different temperatures can be asymmetric for forward and reversed temperature biases when two conditions are simultaneously satisfied: the interactions dominating heat conduction should be nonlinear, and the molecular junction should be asymmetric. It was reported that rectification in such systems could be as high as 50% in some cases. Further, studies by Segal *et al*. [85] showed that negative differential thermal conductance (NDTC) is

possible in molecular junctions and has a similar origin as heat rectification, the difference being that NDTC requires a strong molecule-reservoir coupling while asymmetry in junction structure may not be necessary.

2.4 Experimental Techniques for Probing the Charge and Thermoelectric Properties of Molecular Junctions

A range of experimental techniques [11,12,49,83,87,88] have been developed recently to study the charge transport properties of single and multiple molecule junctions. Some of the widely used techniques include the electromigrated break junction (EBJ) technique [12], the mechanically controllable break junction (MCBJ) technique [83], the scanning tunneling microscope-break junction (STM-BJ) technique [11,49,87-89], and the contact probe-atomic force microscope (CP-AFM) technique [90,91]. These techniques often complement each other and are uniquely suited for specific studies. Among all these techniques, the STM-BJ technique (invented by Xu and Tao [11]) provides one of the most convenient approaches for performing a large number (>1000) of two terminal single-molecule transport measurements in a short time (<1 hour), enabling a statistical interpretation of results. Further, with some modification, the STM-BJ technique also enables thermoelectric studies [21,92-95] of a large number of single molecule junctions in a short time. Therefore, we will focus on describing this technique in detail. In addition to the STM-BJ technique, the CP-AFM technique can also be used for probing the thermoelectric properties of molecular junctions [18] and will be described in detail.

2.4.1 Formation of Metal-Molecule-Metal Junctions

The first step in both the STM-BJ and the CP-AFM techniques is to form a monolayer of chemically bound molecules on a metallic surface (Figure 2.6). This step is accomplished by exposing a suitable metal surface to a solution containing organic molecules terminated with reactive chemical groups, like thiols (-SH) or amines ($-NH_2$). On contact with the metal surface, these reactive groups chemically bind to the metal surface through the formation of a thiol-metal or an amine-metal bond [96]. For example, when a gold surface is exposed to a liquid or a gas containing thiol terminated organic molecules (at room temperature) the molecules bind strongly with gold through a thiol-gold bond (Figure 2.6a). If the environment contains a sufficiently large concentration of organic molecules, the gold surface is completely covered in a short time (minutes). Given sufficient time (hrs), the organic molecules (with some exceptions) spontaneously self-assemble into an ordered lattice (Figure 2.6b) [96]. Molecules bound to a substrate in such a manner can readily be used to form single-molecule junctions by employing the STM-BJ technique or multiple-molecule junctions by using the CP-AFM technique.

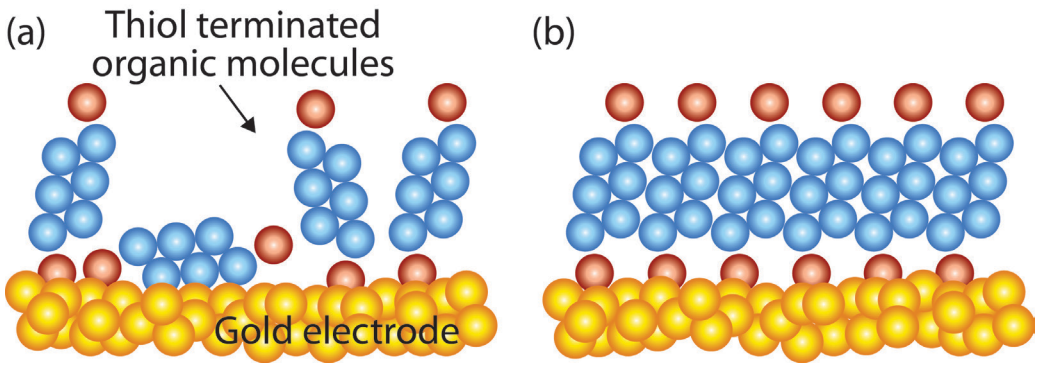

Figure 2.6 (a) Thiol terminated organic molecules chemically bind to the metal(gold) surface (b) A monolayer of organic molecules self-assembled on a gold surface.

2.4.2 Scanning tunneling microscope break junction (STM-BJ) technique

The first step in creating single molecule junctions using the STM-BJ technique [11,87] is to coat a metallic (e.g., gold) surface with linear organic molecules terminated on both ends with metal binding groups (-SH, -NH_2). This molecule-coated surface is placed in the proximity of a sharp STM tip (Figure 2.7a) and the STM tip (e.g., made of gold) is slowly driven at ~5 nm/s towards the metal substrate. During this process, a voltage bias is applied between the STM tip and the substrate and the current through the STM tip is constantly monitored. When the current reaches a large predetermined value (determined heuristically [87]), it indicates the formation of a large number of metal (substrate)-molecule-metal (tip) bridges due to the chemical interaction between the end groups of the molecules and the tip. When the STM tip is withdrawn slowly (~1 to 5 nm/s) from the substrate, the molecules trapped between the gold electrodes start breaking away one at a time until a single molecule is trapped between the electrodes (Figure 2.7b illustrates this process). Figure 2.7c shows the conductance (G) of the junction during this process of withdrawal. It can be seen that the conductance decreases in quantam steps, indicating that the molecules are breaking off one at a time. Each step corresponds to the breaking of one or more molecules. Ultimately, the last molecule trapped in the junctions also breaks away, resulting in a current below the detection limit [11,87]. The withdrawal process can be stopped when the last molecule is trapped thus forming a metal-single molecule-metal junction. The amount of time that the single molecule can be trapped depends on the stability of the STM tip and is influenced by vibrations and thermal drift. Recent work by Lee *et al.* [89] suggests that single molecule junctions can be stably maintained for more than a minute at room temperature by using a custom designed

scanning tunneling microscope (Figure 2.8) that minimizes thermal drift as well as the effect of environmental perturbations.

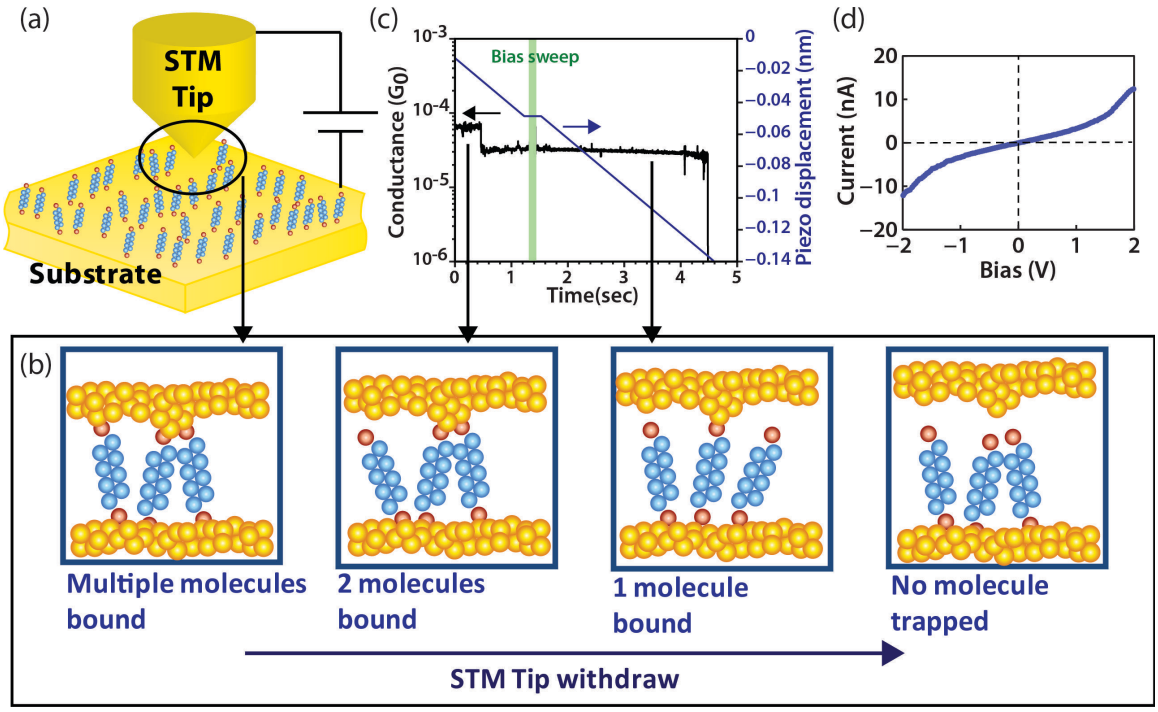

Figure 2.7 (a) STM tip in proximity to molecule coated substrate. (b) The process of forming a single-molecule junction. (c) The conductance of a molecular junction as the STM tip is withdrawn at ~5 nm/s ($G_0 = 2e^2/h$ is the quantum of charge conductance ~1/12.9 kΩ). (d) A current-voltage characteristic of a molecular junction. Reproduced with permission from [89], Copyright 2011 by the Institute of Physics.

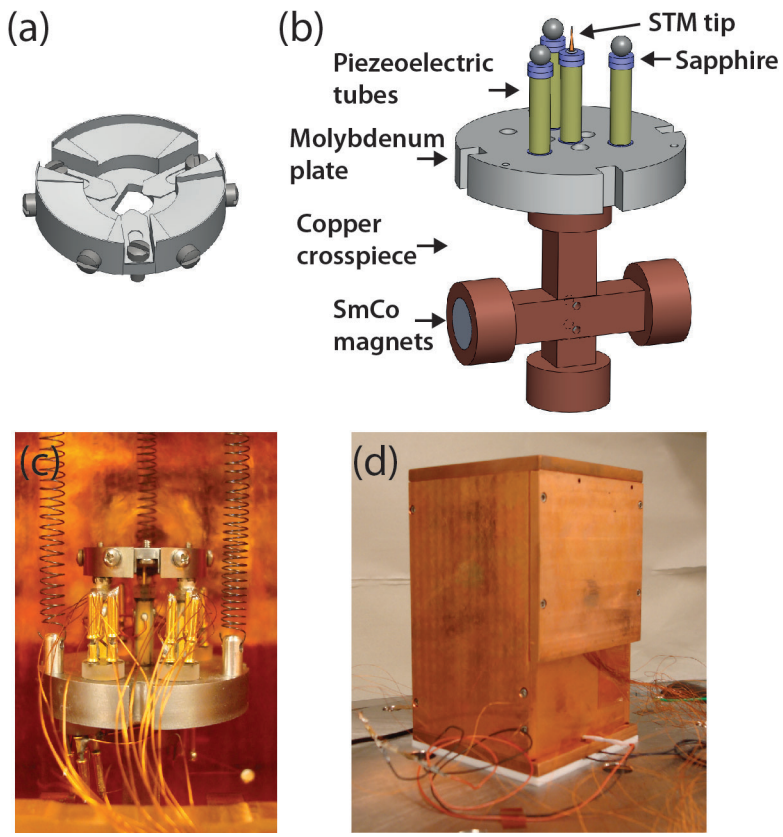

Figure 2.8 STM scanner assembly and radiation shield. (a) Schematic of the sample plate. (b) Schematic of the Besocke scanner featuring four piezoelectric tubes. (c) The assembly of the sample plate and the STM scanner. (d) The copper enclosure (radiation shield) which houses the scanner. Reproduced with permission from [89], Copyright 2011 by the Institute of Physics.

2.4.3 Measurement of the electrical conductance of single molecule junctions

When a voltage bias is applied across a molecular junction, an electric current flows through the molecules trapped in the junction because this provides the path of least resistance to electrons. The electrical conductance and charge transport properties of molecular junctions have been measured by several groups [11,49,87] to elucidate the relationship between molecular structure of junctions and their electrical transport properties. In order to illustrate the use of the STM-BJ technique to study electrical

conductance, we describe an experimental study where the electrical conductance of a series of molecules (Figure 2.9a, hexanedithiol (HDT), octanedithiol (ODT) and decanedithiol (DDT)) was measured by Lee *et al.* [89], following a procedure originally developed in the pioneering work of Xu and Tao [11].

In order to obtain a statistically meaningful measure of the electrical conductance, ~1000 experiments were performed for each type of molecule to obtain conductance traces as described above. The obtained conductance traces (Figure 2.9b shows seven representative traces of Au-ODT-Au junctions) were analyzed by building a histogram [11]. The conductance histogram obtained from ~1000 junctions formed using ODT molecules, without any data selection, is shown in Figure 2.9c. The most probable value of the conductance of an Au-ODT-Au junction is obtained from a Gaussian fit to the histogram and corresponds to a value of $\sim 2.16 \times 10^{-5}\ G_0$, where $G_0 = 2e^2/h$ is the quantum of electrical conductance (e is the charge of an electron and h is the Planck constant). Further, the full width at half maximum (FWHM) of the histogram is found to be $\sim 6.6 \times 10^{-5}\ G_0$ and represents the uncertainty in the measured conductance. Similar experiments performed with HDT and DDT molecules suggest that the conductance of the Au-HDT-Au junctions is $\sim 2.7 \times 10^{-4}\ G_0$ and that of Au-DDT-Au junctions is $\sim 5.2 \times 10^{-6}\ G_0$. The measured electrical resistance of the molecular junctions is shown in Figure 2.9d and is found to increase exponentially with increasing length. Such a rapid decrease in the electrical conductance occurs due to the exponential decrease in the probability of transmission with an increasing chain length and is well explained by a simple tunneling barrier model [97]. We note that several groups have confirmed that the features in the conductance traces do not arise when control experiments are performed on a clean Au

surface. Histograms obtained in one such control experiment are shown in Figure 2.9c and do not feature a peak.

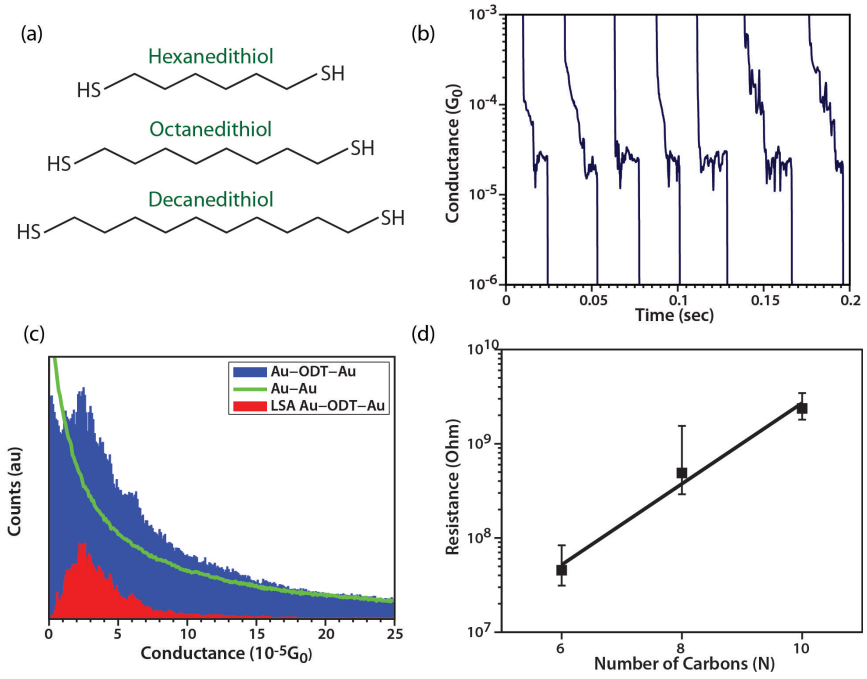

Figure 2.9 (a) The series of molecules that were used in the electrical resistance studies (b) Representative conductance traces obtained in individual measurements. (c) Histograms constructed from a 1000 individual measurements without any data selection. (d) The measured resistance of molecular junctions is found to increase exponentially with length. Reproduced with permission from [89], Copyright 2011 by the Institute of Physics.

2.4.4 Measurement of current-voltage (*I-V*) characteristics of single molecule junctions

In addition to measuring the electrical conductance of molecular junctions, it is also possible to measure their current-voltage (*I-V*) characteristics, which are essential for performing additional spectroscopic studies [89]. In order to obtain the *I-V* characteristics of single molecule junctions, the withdrawal process (described earlier) is stopped when

the conductance equals that of a single molecule junction. Subsequently, the voltage bias is varied linearly while monitoring the electric current flowing through the junction. Figure 2.7c shows a conductance trace reflecting the procedure described above. The region highlighted in green (Figure 2.7c) represents the location where the voltage sweep is performed. The *I-V* characteristic obtained in one such experiment is shown in the Figure 2.7d.

2.4.5 Measurement of the Seebeck Coefficient (thermopower) of a Single Molecule Junction

A technique to study thermoelectric effects in molecular junctions has been recently developed by Reddy and coworkers [21]. This is based on a modification of the STM-BJ technique. The key to making this measurement is the setting up of a temperature differential, ΔT, across the molecular junction. In Figure 2.10a, a single molecule junction formed by using the STM-BJ technique is depicted. The key difference is that the metal-coated substrate is heated, while the gold STM tip is kept at room temperature by putting it in contact with a large thermal reservoir at room temperature. This creates a tip-substrate temperature differential, ΔT. This is possible because the molecular junction thermal conductance is sufficiently smaller than the thermal conductance between the gold STM tip and the thermal reservoir with which it is in contact [21,98]. Therefore, the gold tip is at the reservoir temperature and the heat flow from the hot substrate to the tip does not cause the tip temperature to increase. The experimental procedure to measure the Seebeck coefficient involves the trapping of multiple molecules between the electrodes following the procedure described above in the STM-BJ technique. After this is achieved, the voltage bias and the current amplifier that are used to monitor the current

are disconnected and a high input-impedance custom-built voltage amplifier is connected (see Figure 2.10a) to measure the tip-substrate Seebeck voltage induced by ΔT. The tip is then slowly withdrawn until all the molecules trapped in the junction break off. During this process, the output voltage ΔV is continuously monitored with the tip grounded; when the last molecule breaks off the Seebeck voltage differential vanishes [21]. The results obtained in a series of such measurements using a Benzenedithiol (BDT) molecule trapped between gold electrodes are shown in Figure 2.10b for various temperature differentials ranging from 0 K to 30 K. This output voltage ΔV, due to the temperature differential ΔT, is a measure of the Seebeck coefficient, which is obtained from the equation $S_{junction} = -\Delta V / \Delta T$ [21] to be +8.7 ± 2.1 μV/K. We note that a variation of the Seebeck coefficient measurement technique described above has also been developed recently by Widawsky *et al.* [95] where the thermoelectric properties were probed by measuring the electrical currents resulting from thermoelectric voltages.

2.4.6 Contact Probe-Atomic Force Microscopy Technique (CP-AFM)

In the CP-AFM technique, the top surface of an ordered monolayer of molecules is put in mechanical contact with a metal-coated AFM tip, as shown in Figure 2.11a. This leads to the formation of a junction where ~10 to 100 molecules are trapped between the metal-coated AFM tip and the flat metallic substrate; the number is determined by the radius of the tip [91]. The metal coating on the tip can be chosen to be different from the metallic substrate. If the terminal groups of the organic molecules contacting the metal-coated AFM tip are selected accordingly, they form specific chemical bonds with the AFM tip as opposed to just having a mechanical contact [90]. In this way, it is possible to study the effect of chemical bonding on transport through the junction.

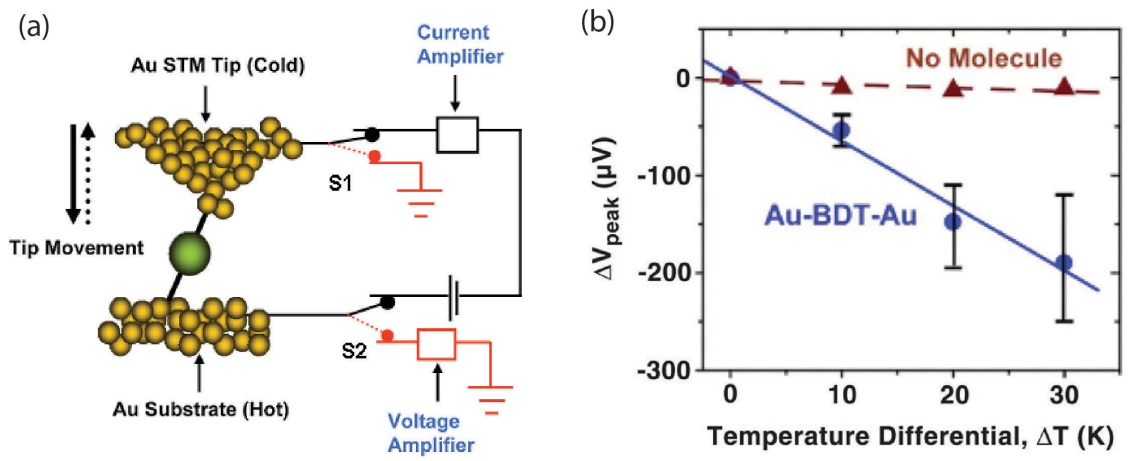

Figure 2.10 (a) A single molecule junction formed by using the STM-BJ technique; the bottom electrode is heated, while the top electrode is thermally anchored to a cold reservoir. (b) The results obtained in a series of thermoelectric voltage measurements using a Benzenedithiol (BDT) molecule trapped between gold electrodes are shown for various temperature differentials ranging from 0 K to 30 K. Reproduced with permission from [21], Copyright 2007 by the American Association for the Advancement of Science.

2.4.7 Measurement of the electrical conductance and current-voltage (*I-V*) characteristics of molecular junctions

When a voltage bias is applied across a molecular junction formed using the CP-AFM technique, a current flows through the junction as shown in Figure 2.11a. The voltage applied across the junction can be varied to obtain the current-voltage (*I-V*) characteristics of the molecular junction. A typical *I-V* characteristic obtained by trapping a 1,1′, 4′,1″-terphenyl-4-thiol (TPT) molecule between gold electrodes is shown in Figure 2.11b. Given the wide variety of molecules that can be self-assembled on surfaces, the CP-AFM technique has been extensively used to understand the effect of (1) the length of

the molecules, and (2) terminal groups of the molecules on the electrical conductance of molecular junctions [90,91,99].

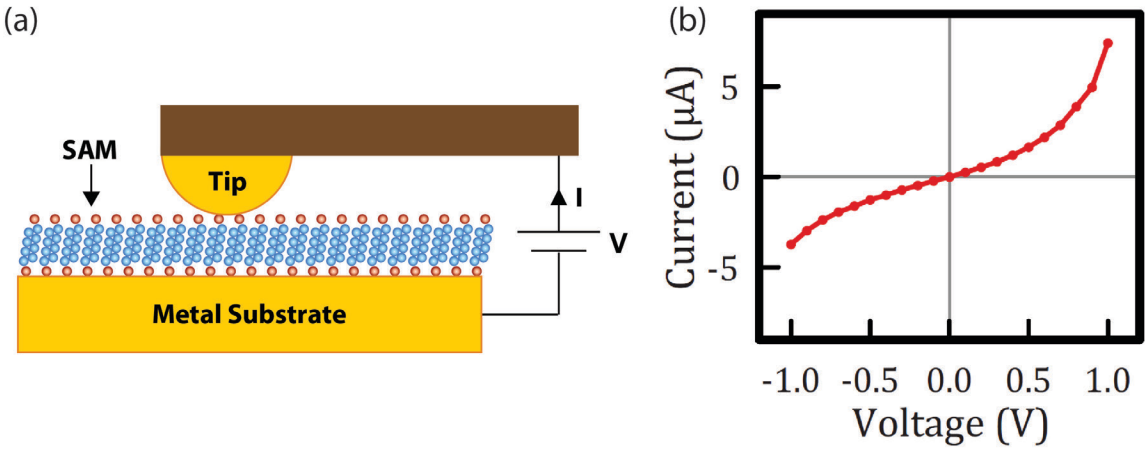

Figure 2.11 (a) The formation of a multiple molecule junctions using the CP-AFM technique; a metal coated AFM tip is placed in soft mechanical contact with a metal electrode coated with a monolayer of molecules (b) The measured current-voltage (I-V) characteristics of a Au-TPT-Au molecular junction. Reproduced with permission from [18], Copyright 2008 by the American Institute of Physics.

2.4.8 Measurement of the Seebeck Coefficient (Thermopower) of Molecular Junctions Using the CP-AFM Technique

In order to measure the Seebeck coefficient of molecular junctions, Tan *et al*. [18,48] made two additions to the CP-AFM technique (Figure 2.12a). These include (1) an electrical heater that is attached to the substrate on which the molecules are self assembled, making it possible to heat the substrate to an elevated temperature $T+\Delta T$ (Figure 2.12a) and (2) a short (~ 125 μm long, 35 μm wide, and 1 μm thick) silicon cantilever coated with gold, instead of a silicon nitride cantilever traditionally employed in CP-AFM, is chosen and anchored to a thermal reservoir at a temperature T. Given the

large thermal conductivity of silicon [100] (~150 W/m·K) and the relatively poor thermal conductivity of the surrounding air (~0.024 W/m·k), thermal modeling [45] suggested that the temperature of the metal-coated cantilever tip, which is in contact with molecules must be between T and $T + 0.05\Delta T$. This implies that at least 95% of the temperature differential (ΔT) occurs across the molecules trapped in between the metal electrodes.

The thermoelectric voltage of the junction was measured by connecting a custom-built high-input impedance voltage amplifier between the gold-coated AFM cantilever and the gold-coated substrate. The measured thermoelectric voltages (ΔV) for junctions created by trapping TPT molecules between gold electrodes are shown in Figure 2.12b. The magnitude of the measured thermoelectric voltage was found to increase linearly when the temperature differential (ΔT) applied across the molecular junction was increased from 0 K to 12 K in steps of 3 K. These experiments suggest that the Seebeck coefficient of a Au-TPT-Au junction is +16.9 ± 1.4 μV/K. Control experiments were also performed where the thermopower of a Au-Au junction with a resistance of ~98 Ω was measured. The thermoelectric voltage measured in these control experiments was found to depend on the resistance of the junction [101] and varied between 0.1 μV/K for low contact resistances (mΩ) and a maximum of ~1.3 μV/K at ~100 Ω. These values were much smaller than the thermoelectric voltage measured for Au-TPT-Au junctions (Figure 2.12b), clearly demonstrating that the thermoelectric voltage arises due to the molecules in the molecular junctions.

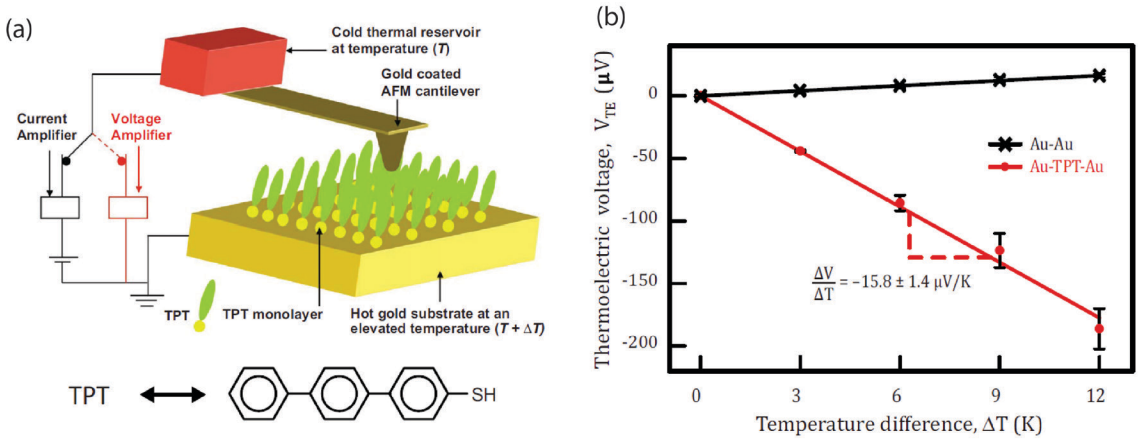

Figure 2.12 (a) The thermoelectric voltage measurement set-up using an atomic force microscope (AFM). The bottom substrates is heated, whereas the gold-coated silicon AFM probe is held at room temperature by thermally anchoring it to a reservoir (b) The measured thermoelectric voltage of a Au-TPT-Au junction as a function of the applied temperature differential. Reproduced with permission from [18], Copyright 2008 by the American Institute of Physics.

2.4.9 Insights Obtained from the Measurement of the Seebeck Coefficient of Molecular Junctions

In addition to enabling the study of nanoscale energy conversion, thermoelectric measurements provide additional insights into the electronic structure of molecular junctions that cannot be obtained by electrical transport measurements alone. Specifically, conductance measurements alone cannot uniquely identify [21,53] whether the HOMO orbital or the LUMO orbital lies closer to the chemical potential. However, thermoelectric measurements can answer this question. If the transmission function of a molecular junction is relatively smooth and well approximated by a sum of Lorentzian shaped functions, then it can be deduced from Eq. (2.5) that a positive thermopower is associated with a junction where the HOMO is closer to the chemical potential, indicating

hole dominated (p-type) transport. In the other scenario, transport is LUMO dominated (n-type) and is related to a negative thermopower. The two scenarios that thermoelectric measurements can be used to distinguish are shown in Figure 2.13. In the case of the experiments described above, a positive Seebeck coefficient was observed for both Au-BDT-Au and Au-TPT-Au junction suggesting that transport in both these junctions is dominated by the HOMO level.

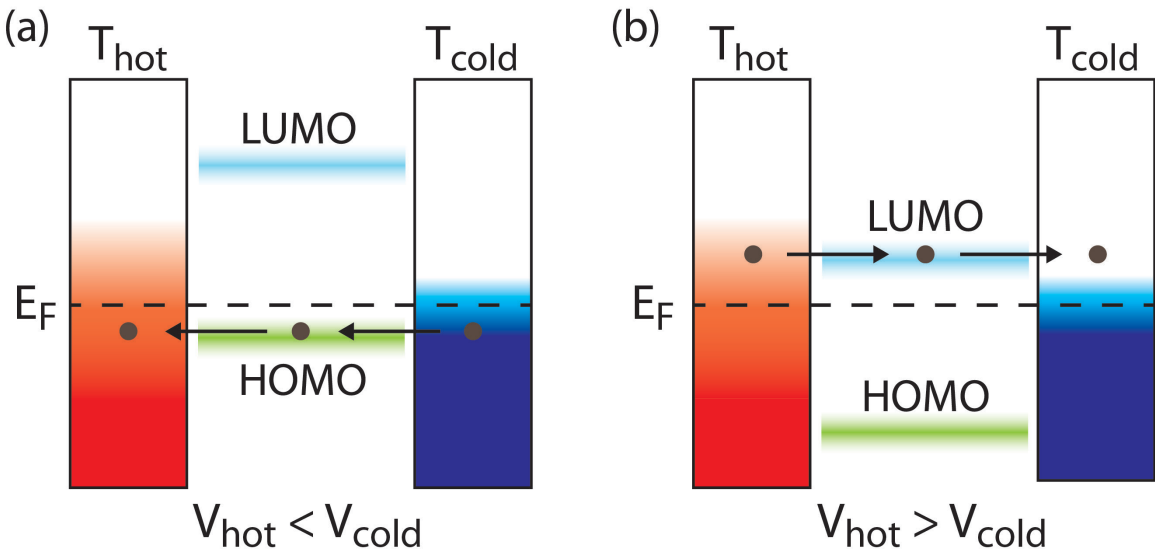

Figure 2.13 The two scenarios that thermoelectric measurements can distinguish. (a) A scenario where the chemical potential is closer to the HOMO orbital and results in the colder electrode being at a higher potential in comparison to the hotter electrode. (b) The chemical potential is closer to the LUMO orbital, which results in the hotter electrode being at a higher potential.

2.5 Experimental Techniques for Probing the Thermal Transport Properties of Single Molecule Junctions and Single Polymer Chains

The study of thermal transport properties of single molecule junctions is very challenging because the expected heat currents are very small, i.e., ~10 pW-100 pW, for an applied

temperature bias of 1K. Therefore, none of the single molecule measurement techniques that are currently available have the desired resolution to perform these studies. In this section, we will first describe pioneering experiments that have been conducted recently to probe thermal transport in monolayers of molecules and polymer fibers with nanoscale diameters. Subsequently, we will briefly outline possible approaches for measuring the thermal transport properties of single-molecule junctions and single-polymer chains.

2.5.1 Thermal Transport in Monolayers of Molecules

Heat transport through molecular layers sandwiched between a liquid and a metal have been recently studied by Wilson *et al*. [102] and Ge *et al*. [103,104]. In these measurements, heat transfer in molecular layers between a metal and a liquid were studied using time-resolved optical absorption and time-domain thermoreflectance techniques. These experiments provided important insights into the effect of the solvent properties and the hydrophobicity/hydrophilicity of the molecular end groups on the interfacial thermal conductance.

Wang *et al.* [105] studied thermal transport in self–assembled monolayers of long-chain alkane molecules on a gold surface using a femtosecond laser. In this experiment, heat transfer through the molecular layer was studied by first exciting the metal underneath the monolayer and probing the resulting thermal signature on the top of the monolayer using a time-resolved sum-frequency generation (SFG) spectroscopic technique. This work demonstrated that the primary thermal resistance to heat transfer was at the metal-molecule interface and the heat transfer through the molecules was ballistic. Further, it was estimated that the thermal conductance associated with a single alkane molecule-metal (gold) interface was ~50 pW/K.

Wang *et al.* [106] recently studied heat transport through gallium arsenide(GaAs)-monolayer-metal junctions. These junctions were made using a nanotransfer printing technique where a gold electrode that is initially deposited on a silicon stamp is transfer printed onto an undoped GaAs substrate with a self assembled monolayer (SAM) of organic molecules on its surface. The gold(Au) layer sticks to the molecular monolayer because the molecular layer on undoped GaAs is terminated with reactive end groups that chemically bind to gold. The heat transport through three different kinds of GaAs molecule-Au junctions was measured in this study where the length of the molecules was systematically increased from eight to ten carbon atoms. These measurements suggested that the thermal conductance of these molecular monolayers was relatively independent of the length of molecular chains, suggesting that the primary source of thermal resistance is at the solid-molecule interface.

In addition to these studies, Losego *et al.* [107] recently studied thermal transport in monolayers of organic molecules sandwiched between a quartz (Qz) substrate and a Au thin-film. Broadly, organic molecules were chosen such that one end group was always a silane whereas the other end group was chosen to be either bromine (-Br), methyl (-CH_3), amine (-NH_2), or thiol (-SH). These molecules were first self-assembled onto a Qz substrate by taking advantage of silane chemistry. Subsequently, a Au thin film was transfer printed onto the monolayer. In such samples, the binding strength between Au surfaces and the end groups (-Br/-CH_3/-NH_2/-SH) of the organic monolayer is controlled by the chemical interaction between the end group and the Au thin-film. Measurements of thermal transport at these interfaces, performed using time-domain thermal reflectance technique (TDTR), revealed that the interfacial thermal conductance is dependent on the

binding strength and could be tuned between 30 and 70 MW/m^{2}K by appropriately tuning the end-group chemistry. The authors of this work also performed complementary measurements to characterize the interfacial bond strength of these samples, details of which can be found in Ref. [107].

Shen *et al*. [77] have recently probed heat transport in ~50-500 nm diameter bundles of polymers containing thousands of polymer chains that are partially aligned along the back-bone of the polymer. These studies performed using a novel bimaterial cantilever-based technique have shown that the thermal conductivity of polymer bundles with microscopic alignment is much larger (~100 W/m·K) than bulk polymer thermal conductivity (~0.1 W/m·K) [108]. This enhancement in thermal conductivity was explained by detailed molecular dynamics simulations that highlighted the effect of molecular alignment on the scattering of phonons.

The work described above represents important progress towards measuring heat transport in molecular junctions. However, a lot more needs to be accomplished: an accurate technique that can reliably measure thermal transport through a variety of single-molecule junctions and single-polymer chains needs to be established. These technical improvements are crucial to differentiate between a variety of fundamental hypotheses regarding the atomistic and molecular mechanisms of transport in molecular junctions and address the specific questions raised by computational studies, as described earlier. Further, single-molecule techniques will enable the elimination of interaction between molecules that are inevitable in monolayer/polymer fiber measurements, which complicate the analysis and interpretation of measurements. Finally, the effect of

molecular structure, molecular confirmation, and the chemical composition of electrodes on the thermal conductance of molecular junctions needs to be elucidated.

In order to achieve these goals, it is necessary to develop novel experimental techniques that enable detection of heat currents with picowatt resolution as the computationally predicted thermal conductance of single-molecule junctions and single-polymer chains is in the range of 10-100 pW/K. Any such technique should have three important capabilities: (1) trap molecules between electrodes to form a molecular junction, (2) apply known temperature differentials of a few Kelvin across electrodes that are separated by about a nanometer, and (3) measure the small heat currents resulting from the temperature differential applied across the electrodes of these junctions. All these capabilities are currently available on individual platforms. For example, the STM-BJ technique described earlier is capable of accomplishing the first two goals and recent developments [109] in calorimetry enable measurement of heat currents with 4 picowatt resolution. We believe that an ingenious combination of these techniques should enable probing heat transfer at the single-molecule level.

2.6 SUMMARY AND OUTLOOK

Molecular junctions provide an excellent platform for probing a variety of nanoscale energy conversion and energy transport phenomena. Computational studies have predicted several interesting thermoelectric and thermal transport phenomena that remain experimentally untested until now. For example, the possibility of realizing reversible thermoelectric energy conversion in molecular junctions and the development of junctions that operate close to the Curzon-Ahlborn limit represent two exciting possibilities that have not received much experimental attention until now. In addition to

this, the decades-old prediction of divergent thermal conductivity in low-dimensional systems such as single-polymer chains has also not been experimentally tested.

The major technical advancements of the past decade in manipulating single molecules and performing nanoscale thermometry and picowatt-resolution calorimetry provide us with a unique opportunity to experimentally test these longstanding predictions. We believe that actively pursuing these challenging experimental studies is critical to the advancement of nanoscale transport theories and predictive modeling of charge and energy transport at the nanoscale. This represents an important challenge as well as an immense opportunity to researchers in the field of nanoscale energy transport.

Chapter 3

Creation of Stable Molecular Junctions with a Custom Designed Scanning Tunneling Microscope

Reproduced with permission from *Nanotechnology*
Woochul Lee, and Pramod Reddy, *Nanotechnology*, 2011, 22, 485703 [89].
Copyright 2011, Institute of Physics.

3.1 INTRODUCTION

Nanoscale molecular junctions provide a unique opportunity to probe quantum transport [26] and are being actively studied due to their potential technological importance in molecular electronics [28] and organic based thermoelectrics [21,43,48]. In fact, a variety of interesting effects including negative differential resistance, rectification, switching, and gating have all been observed [3] in molecular junctions. Further, recent computational studies [37,39] have shown that it may be possible to create molecular junctions with large thermoelectric efficiencies using appropriately tailored organic molecules.

A variety of experimental techniques have been developed recently to study charge transport in single molecule junctions. Some of the widely used techniques include the electromigrated break junction (EBJ) technique [12], the mechanically controllable break junction (MCBJ) technique [83], and the scanning tunneling microscope break junction (STMBJ) technique [11,49,87,110]. These techniques often complement each other and

are uniquely suited for specific studies. The MCBJ and STMBJ techniques are closely related and enable trapping single molecules by mechanically manipulating electrodes [3]. The MCBJ technique is well known for its superb mechanical stability and has been widely used in a variety of two terminal studies of electrical transport in single molecule junctions [111,112]. The STMBJ technique allows for not only two terminal measurements of electrical transport properties but also thermoelectric properties. Further, since the STMBJ technique employs a scanning tunneling microscope [113] it is possible to image the molecules that are being studied, thus enabling more detailed insights [114]. The EBJ technique is well suited for performing three terminal measurements where the electronic structure of the molecular junction is controlled via a gate electrode. However, the EBJ technique involves a substantial effort in micro-fabricating the break junction devices, impeding the study of a large number of molecular junctions in a short time. In contrast to the EBJ technique, the MCBJ and STMBJ techniques provide a convenient approach for performing a large number of two-terminal measurements (>1000) in a short time (<1 hour) enabling a statistical interpretation of results [11].

Recently, the STMBJ technique has been used extensively to study the relationship between the molecular structure and the low bias electrical conductance of molecular junctions [11,49,87,110]. However, the STMBJ technique lacks mechanical stability, resulting in single-molecule junctions that are stable only for short periods of time (<1 second). This poor mechanical stability limits a detailed study of the current-voltage characteristics and the thermoelectric properties of molecular junctions. This apparent limitation of the STMBJ technique is due to the mechanical drift in the scanning

tunneling microscope (STM), which arises from temperature variations and mechanical vibrations.

In this work, we present a custom designed scanning tunneling microscope (STM) that operates at room temperature in a high vacuum environment ($<10^{-6}$ torr) and is capable of stably trapping a molecular junction for more than 1 minute—at least an order of magnitude better than what was reported in previous studies using the STMBJ technique [87]. This improvement in stability is achieved by incorporating four important features into the instrument: (1) a scanner that is designed to suppress drift associated with temperature changes, (2) a temperature controller that allows excellent temperature stability (±1 mK), (3) vibration isolation to attenuate the effect of ground disturbances, and (4) operation in a high vacuum environment to eliminate the effect of acoustic disturbances. We demonstrate that these improvements are sufficient to create single molecule junctions that are stable for long periods (>1 minute). The utility of this instrument is illustrated by performing transition voltage spectroscopy (TVS) [17] on single-molecule junctions, formed by trapping hexanedithiol (HDT), octanedithiol (ODT), decanedithiol (DDT) molecules between gold (Au) electrodes to obtain, approximately, the energetic separation between the Fermi level and closest molecular orbital of the junctions. We believe that this novel instrument will facilitate the study of thermoelectric and thermal transport phenomena in molecular junctions, where it is necessary to perform measurements for long time periods to improve the signal-to-noise ratio.

3.2 STM DESIGN

The STM comprises of a scanner, a temperature controlled radiation shield, control electronics, and a vacuum chamber. Among these the scanner, the temperature controlled radiation shield, and some of the control electronics were custom-built and are described below.

3.2.1 STM Scanner

A detailed schematic of the Besocke scanner [115,116] integrated into the STM is shown in Figure 3.1. The Besocke scanner features four piezoelectric tubes, three of which support a sample plate. A sharp Au tip is mounted on the fourth piezoelectric tube (Figure 3.1), which is at an equidistant position from the other three piezoelectric tubes and is used to scan the sample as well as to trap molecules (explained in detail later). The Besocke scanner is chosen in the present work due to its excellent ability to suppress thermal drift. In general, temperature changes of the entire scanner lead to a thermal expansion/contraction of the piezoelectric tubes. In a Besocke scanner, this expansion/contraction does not translate into large changes in the spacing between the STM tip and the sample plate. This is because the thermal expansion/contraction of the outer piezoelectric tubes supporting the sample plate is almost identical to that of the expansion/contraction of the inner piezoelectric tube resulting in suppression of drift between the tip and the sample. More details regarding the estimated drift of the scanner, scanner fabrication, and vibration isolation are provided in the Section 3.5.

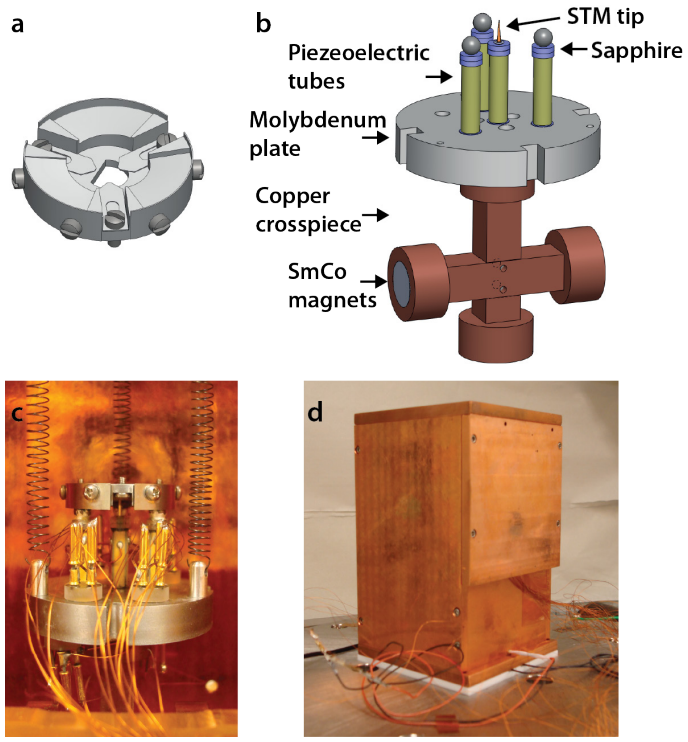

Figure 3.1 STM scanner assembly and radiation shield. (a) The schematic of the sample plate. (b) The schematic of the Besocke scanner featuring four piezoelectric tubes. (c) The assembly of the sample plate and the STM scanner. (d) The copper enclosure (radiation shield) which houses the scanner.

3.2.2 Temperature controlled radiation shield

The Besocke scanner design described above allows for good thermal compensation, ensuring that the scanner is relatively immune to thermal drift. However, the scanner is not completely unaffected by temperature variations. This is primarily due to the mismatch in the thermal expansion coefficient of the STM tip (made of gold) and that of the tungsten balls mounted on the outer piezoelectric tubes (Figure 3.1b). This mismatch results in a drift in the gap between the sample plate and the tip (details in Section 3.5) when the temperature changes with time. Therefore, it is essential to ensure that the temperature variations are very small.

Although the scanner is located in a vacuum environment, it is still thermally coupled to the ambient environment where the temperature varies significantly, ~2 K over a period of 24 hours. This thermal coupling exists because heat can be transported from the ambient environment via the springs and electrical wires that are connected to the scanner (Figure 3.1c) and via thermal radiation. In order to minimize the thermal coupling with the ambient, the scanner is placed in a copper enclosure (Figure 3.1d), which acts not only as a thermal reservoir but also as a radiation shield. Further, the temperature of the enclosure is maintained at a constant value by a custom-built controller (proportional and integral control). The control system senses temperature changes via a thermistor (Omega, 44033-2252Ohm) and attenuates them by modulating the electrical current supplied to an electrical heater integrated into the copper enclosure. Using this approach, it was possible to maintain the temperature of the copper enclosure at a fixed temperature (~5 K above the average ambient temperature) with variations less than ±1 mK in a 3 hour period (details in Section 3.5).

3.2.3 Scanner Control and Calibration

The motion of the STM scanner is controlled by a combination of a customized real time controller and a commercial STM controller (RHK Technology). The commercial STM controller is used for the coarse and fine approach steps that are essential to place the STM tip in close proximity to the sample surface (i.e., the tunneling region). Further, the commercial STM controller is also used for scanning the surface to obtain topographical information. The real-time controller is implemented using hardware from National Instruments (PXI8110) and is used to increase or decrease the separation between the STM tip and the sample in small increments (as small as 3 pm/step). Such control is

essential for the creation of stable molecular junctions and is discussed in detail below. In order to calibrate the piezoelectric tubes of the Besocke scanner, we adopted an approach similar to that used by others in the past [117,118]. Briefly, the X-Y scan parameters of the piezoelectric tubes were adjusted such that the correct topography of a highly oriented pyrolytic graphite (HOPG) sample was observed [117]. Further, the sensitivity of the piezoelectric tube in the Z direction (perpendicular to the sample) was calibrated by measuring the known step height of a Au (111)terrace [118].

3.3 SINGLE-MOLECULE EXPERIMENTS

The stability and use of this STM is demonstrated by studying electron transport in single-molecule junctions created from hexanedithiol (HDT), octanedithiol (ODT), and decanedithiol (DDT) molecules. The protocol used to create the Au-alkanedithiol-Au junctions is described first. Subsequently, the statistical analysis used for determining the conductance of a single molecule junction is presented. Finally, we present results that demonstrate that single-molecule junctions created using this STM are mechanically stable for extended periods (>1 minute).

3.3.1 Creation of single-molecule junctions

The first step in the formation of Au-alkanedithiol-Au junctions is to create a monolayer of alkanedithiol molecules on a flat Au surface. The flat Au surface is created using a template stripping technique [119]. In this technique, ~100 nm of gold is deposited on a pristine silicon wafer. Subsequently, epoxy (Epotek 377) is applied evenly on the gold-coated silicon wafer and a square glass piece (7 mm × 7 mm) is placed on top of the epoxy. Next, the entire wafer is cured in an oven at ~150 ºC for ~1.5 hours. Later, the

glass piece is cleaved off from the silicon wafer, resulting in a very smooth Au film (RMS value <1 nm over a 1 μm^2 area) that adheres to the glass surface because of the strong bond between gold and epoxy. To coat the alkanedithiol molecules on the flat Au surface, the gold substrate is immersed into an ~1 mM solution of alkanedithiol in ethanol for more than 12 hours. During this time, the alkanedithiol molecules chemically bind to the Au surface through a thiol-Au bond [96]. After taking out the alkanedithiol coated gold substrate, the substrate is rinsed with ethanol to remove molecules that are not chemically bound to the gold surface. This concludes the process of creating a monolayer of molecules on the surface.

To create Au-alkanedithiol-Au junctions, the molecule-coated Au surface is mounted onto the sample plate (Figure 3.1a) of the STM scanner. Subsequently, a coarse approach is performed to place the sample in close proximity (~10 nm) of a sharp Au STM tip (Figure 3.2). Once this is accomplished, the STM tip is driven at ~30 nm/s toward the gold substrate. During this process, a voltage bias (0.1 V) is applied between the STM tip and the substrate and the current through the STM tip is constantly monitored. When the tunneling current reaches a large predetermined value indicating a very small separation (<1 nm) between the tip and sample, an additional voltage of ~0.5 V corresponding to a displacement ~1 nm is applied to the piezoelectric tube to ensure that the Au tip crashes into the flat Au surface. This process is known to ensure the formation of a large number of metal (substrate)-molecule-metal (tip) junctions due to the chemical interaction between the thiol end group of the alkane molecules and the Au tip [87].

When the STM tip is withdrawn (at ~30 nm/s) from the substrate, the molecules trapped between the gold electrodes start breaking away until a single molecule is trapped

between the electrodes (Figure 3.2 illustrates this process). During the withdrawal process, the current through the molecular junction is measured using a current amplifier and continuously monitored by a data acquisition system that collects data at a sampling frequency of 40 kHz. Representative conductance traces obtained in such experiments with octanedithiol molecules are shown in Figure 3.3a. These conductance traces show characteristic features (steps) that correspond to the mechanical breaking of the molecular junctions [11,87].

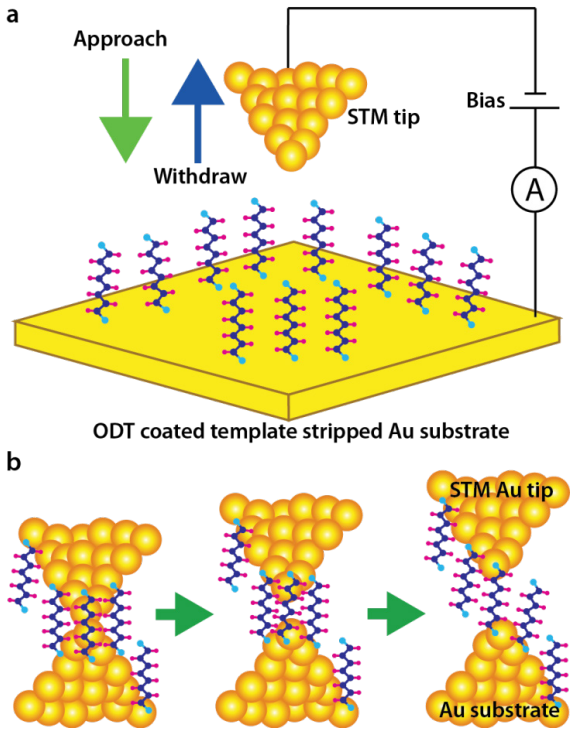

Figure 3.2 Schematic description of the process of creating single-molecule junctions. (a) A Au STM tip and an octanedithiol (ODT)-coated Au sample are shown. A voltage bias (+0.1 V) is applied between the STM tip and the substrate and the current through the STM tip is constantly monitored (a positive bias corresponds to a scenario where the substrate is at a higher potential than the STM tip). The STM tip approaches the surface until it makes mechanical contact and is withdrawn immediately after contact. During this process ODT molecules are trapped between the Au electrodes. (b) As the Au STM tip is withdrawn the ODT molecules bridging the two Au electrodes start to break. Ultimately, one molecule bridges the two Au electrodes resulting in a single molecule junction.

3.3.2 Statistical Analysis

In order to obtain statistically meaningful results, ~1000 experiments were performed for each molecule (HDT/ODT/DDT) to obtain conductance traces. The conductance traces were analyzed by building a histogram following the approach described by Xu *et al.* [11]. The conductance histogram obtained from the conductance traces of 1000 junctions of Au-ODT-Au without any data selection (conventional conductance histogram) is shown in Figure 3.3b. The conductance histograms of Au-HDT-Au and Au-DDT-Au junctions are shown in the supporting information. The most probable values of the conductance of a Au-HDT-Au, Au-ODT-Au junction, and Au-DDT-Au junction were obtained from a Gaussian fit to the histogram and corresponds to a value of $\sim 2.7 \times 10^{-4}$ G_0, $\sim 2.2 \times 10^{-5}$ G_0, and $\sim 5.2 \times 10^{-6}$ G_0, respectively, where $G_0 = 2e^2/h$ is the quantum of electrical conductance (e is the charge of an electron and h is the Planck constant). Further, the full width at half maximum (FWHM) of the histograms were found to be $\sim 5.2 \times 10^{-4}$ G_0 (HDT), $\sim 6.6 \times 10^{-5}$ G_0 (ODT), $\sim 1.38 \times 10^{-5}$ G_0 (DDT) and represent the uncertainty in the measured conductance. In order to verify that the peak arises from the alkanedithiol molecules, a control experiment was performed where measurements were performed on a clean Au surface. The histogram (green) obtained in such an experiment is shown in Figure 3.3b and does not feature a peak. Similar control experiments were performed for Au-HDT-Au and Au-DDT-Au junctions and are presented in Section 3.5. These experiments clearly confirm that the peak in the histogram is obtained only in the presence of alkanedithiol molecules.

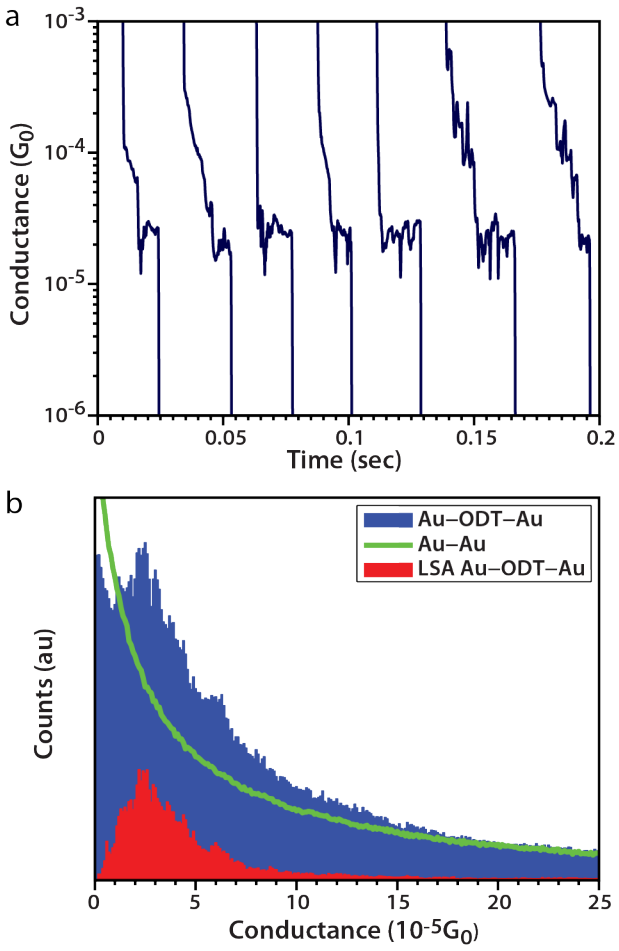

Figure 3.3 Measurement of the electrical conductance of a single-molecule junction. a) Conductance traces obtained while withdrawing the STM tip from the sample at ~30 nm/sec. b) Conductance histogram created from 1000 Au-octanedithiol-Au junctions (blue) shows a peak at ~2.2 × 10^{-5} G_0. Conductance histrogram obtained in a control experiment where ODT molecules were not present (green) shows no peak. Conductance histogram obtained from last step analysis (red) shows a peak at ~2.6 × 10^{-5} G_0.

In addition to this conventional histogram-based analysis, we also performed the last step analysis (LSA) [87], which was introduced by one of us, in collaboration with others, in the past. In this analysis, the magnitude of the last step in the conductance traces, which corresponds to the conductance of a single molecule junction, is measured from a large number (~1000) of conductance traces and is reported in the form of a histogram (Figure

3.3b, and in Section 3.5). The histograms have a peak from the Gaussian fit at ~2.8×10^{-4} G_0 (HDT), ~2.6×10^{-5} G_0 (ODT), and ~5.5×10^{-6} G_0 (DDT). The corresponding uncertainty of FWHM is ~3.1×10^{-4} G_0 (HDT), ~4.3×10^{-5} G_0 (ODT), and ~4×10^{-6} G_0 (DDT). The peak value obtained using LSA corresponds well with the result obtained using the conventional histogram analysis above. In our past work using a commercial STM (Molecular Imaging, pico-STM) that operated in ambient conditions, it was not possible to obtain a clear peak using conventional histogram analysis without data selection. However, using this new ultra-stable STM, a clear peak is observed in the conventional conductance histogram also. We hypothesize that this improvement in the quality results from the superior stability of our STM, which enhances the amount of time that the most probable conductance value of the junction is obtained in a conductance trace.

When the measured electrical resistance of the alkanedithiol junctions is plotted vs the number of carbon atoms in the chain (see Section 3.5), it is apparent that the electrical resistance increases exponentially with the length of the chain. Such an exponential dependence of the electrical resistance on the length of the molecules is expected because electron transport through Au-alkanedithiol-Au molecular junctions occurs via nonresonant tunneling. Therefore, the resistance of a single molecule junctions is proportional to $\exp(\beta N)$, where N is the number of carbon atoms in the alkanedithiol and β is the tunneling decay constant. A curve fit (see Section 3.5) to the measured electrical resistance of the Au-alkanedithiol-Au junctions suggests that β is ~0.99/carbon atom and is in good agreement with previous reports [99].

3.3.3 Demonstration of Mechanical Stability of Junctions

The stability of molecular junctions created using the custom-built STM was tested at room temperature and in a high-vacuum environment. First, single-molecule junctions were created by crashing the STM tip into the substrate as described in Section 3.3.1. Subsequently, the tip was withdrawn from the sample surface at ~0.6 nm/sec until a conductance value below $0.007G_0$ was obtained. After this, the withdraw speed was further decreased to ~0.003 nm/sec. This slow withdrawal process was continued until a conductance plateau was observed around the most probable conductance value as determined from the conductance histograms, suggesting that a single molecule junction was created. At this time, the Z displacement of the piezoelectric tube was stopped to test for the stability of the molecular junction. A representative plot obtained in one such experiment using Au-ODT-Au junctions is presented in Figure 3.4 and shows that the electrical conductance can be maintained at approximately the same value for >100 seconds. In ~50% of the experiments performed with HDT, ODT and DDT molecules following this protocol, it was possible to trap junctions for >100 seconds. This demonstrates that the custom-designed STM is capable of creating molecular junctions that are stable for more than 1 minute.

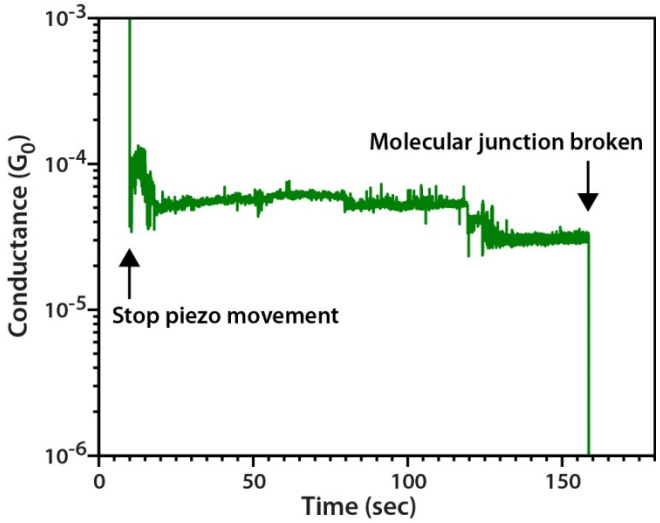

Figure 3.4 To demonstrate the mechanical stability of molecular junctions the withdrawal of the piezoelectric tube is stopped after the conductance reaches the most probable conductance value (conductance of a single molecule junction). Subsequently, the conductance of the molecular junction is monitored until the junction breaks down. A representative trace obtained in measurements of Au-octanedithiol-Au junctions is shown above. The Au-octanedithiol-Au junction is found to be stable for more than 2 minutes, after which the conductance drops rapidly, indicating a breakdown of the junction.

It can be seen in Figure 3.4 that after about 2 minutes the conductance of the ODT junction drops rapidly due to the breakdown of the junction. Understanding the mechanism for the breakdown of the molecular junctions after ~1-2 minutes is critical to explore the possibility of further improving the stability of junctions. Does the junction break due to mechanical drift or due to thermally driven breakdown of the Au-thiol or Au-Au bonds? We believe that the small thermal drift of the STM scanner ultimately results in increasing the separation between the STM tip and the substrate, leading to a mechanical breakdown of the Au-ODT-Au junction. This hypothesis is supported by previous experimental studies [120], where the thermodynamic stability of Au-molecule-Au junctions created from thiol-terminated molecules was studied at room temperature

using a mechanically controllable break junction technique. These studies [120] suggest that the lifetime molecular junctions, created by trapping thiol-terminated molecules between gold electrodes, should be >1 hour if thermal drift is attenuated further. Therefore, it should be possible to further improve the stability of molecular junctions by attenuating the temperature variations below the current level (±1 mK).

3.4 TRANSITION VOLTAGE SPECTROSCOPY OF SINGLE MOLECULE JUNCTIONS

A new experimental technique—transition voltage spectroscopy (TVS)—that can determine, approximately, the energetic separation between the Fermi level and closest molecular orbital of the junctions has been established recently [17,121,122]. In TVS the current-voltage characteristics of molecular junctions are analyzed by plotting a Fowler-Nordheim (FN) curve, $\ln(I/V^2)$ against (I/V). For asymmetric molecular junctions, a FN plot is expected to feature a minimum value for either positive or negative bias voltages[123]. However, if the junction is symmetric the FN plot would feature two minima (one each for positive and negative biases) that have almost the same magnitude[123]. Recently, TVS has been interpreted within a coherent electron transport model (Landauer formalism) by Huisman *et al.* and Araidai *et al.* [122,124]. In this approach, the transmission function of the molecular junction is computed and typically features peaks at energies corresponding to the HOMO and LUMO orbitals of the molecular junction. Within this model it has been suggested that the minima in the FN plot occurs when a certain fraction of the transmission function enters the bias window between the quasi-Fermi levels of the electrodes. The minima obtained using Fowler-Nordheim curves is called the transition voltage (V_{trans}) and is expected to approximately

indicate the energetic separation ($\Delta \sim |eV_{trans}|$) between the closest molecular orbital and the chemical potential (Fermi level).

Recently, several researchers have used transition voltage spectroscopy to qualitatively study the effect of molecular structure, gate voltage, and molecular length on the energetic separation of molecular junctions [18,20,121]. However, most of these studies were performed either in junctions where multiple molecules were trapped between electrodes or in single-molecule junctions created using the electromigrated break junction technique at low temperatures (4.2 K) [19,20]. Here we demonstrate the utility of the ultra-stable STM by performing TVS—in single-molecule junctions—at room temperature.

In order to obtain the I-V characteristics of single molecule junctions, which are necessary for performing TVS, the withdrawal process (described in Section 3.3.3) is stopped when the conductance equals that of a single molecule junction. Subsequently, the voltage bias is varied linearly between –2 to +2 V while monitoring the electric current flowing through the junction. We note that, in our experiments, a positive bias corresponds to a scenario where the substrate is at a higher potential than the STM tip. Figure 3.5a shows a conductance trace for ODT reflecting the procedure described above. The region highlighted in green (Figure 3.5a) represents the location where the voltage sweep is performed. Two representative *I-V* characteristics obtained in such experiments are shown in the inset of Figure 3.5b. The corresponding FN plots obtained using these *I-V* curves are shown in Figure 3.5b. The FN plot (red circles) features a minima on both sides and corresponds to the more symmetric *I-V* curve (solid red line in inset of Figure 5b). The two minima are at –0.697 V^{-1} and 0.6810 V^{-1} and correspond to transition

voltages of –1.43 V and +1.47 V respectively, suggesting an apparent energetic separation of ~1.45 eV (between the Fermi level and the closest molecular orbital) for Au-ODT-Au junctions. The FN plot (blue squares) features only one minima at ~ –0.63 V^{-1}, and corresponds to the less symmetric I-V curve (dashed blue line in inset of Figure 5b). We note that for HDT, ODT and DDT junctions among the 300 I-V curves that were obtained for each junction, only ~50 showed a minimum for both negative and positive voltages. Based on past theoretical works [123,125], we believe that the *I-V* characteristics that show both a positive and negative V_{trans}, with an almost identical magnitude, correspond to molecular junctions that are symmetric in their geometry.

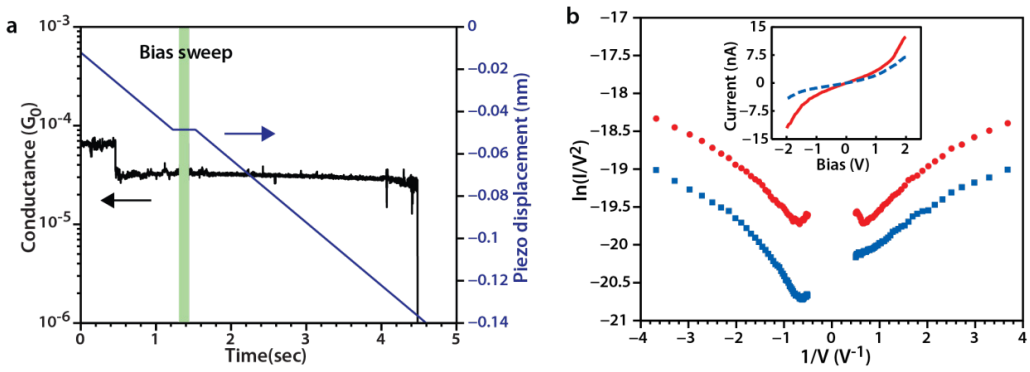

Figure 3.5 Current-voltage (I-V) characteristics and Fowler-Nordhiem plots of Au-ODT-Au junctions. a) The Au STM tip is withdrawn until an electrical conductance of ~2.6 × 10^{-5} G_o (the most probable conductance value) is obtained after which the withdraw process is stopped (the region shown in green) and the voltage is varied from –2 to +2 V to obtain the I-V characteristics. The conductance value remains the same after sweeping the voltage bias, indicating that the molecular junction is not destroyed by the large bias. b) The inset shows two representative I-V curves obtained in measurements. The I-V curve shown in red (solid line) is symmetric and has a Fowler-Nordheim plot (red circles) that features minima at –1.43 V and +1.47 V, respectively. The I-V curve shown in blue (dashed line) is asymmetric and has a Fowler-Nordheim plot (blue squares) that features only one minima at -1.6 V.

In order to obtain statistically meaningful results, positive and negative transition voltages were obtained in ~50 independent experiments each for Au-HDT-Au, Au-ODT-Au, and Au-DDT-Au junctions. The mean value and standard deviation of the obtained transition voltages are presented in Table 1. This data suggests that for each molecular junction the measured positive and negative transition voltages are similar in magnitude, as expected for a geometrically symmetric molecular junction [123]. Further, the relative invariance of the magnitude of the positive and negative transition voltages when the length of the molecular junctions is varied indicates that the energetic separation between the chemical potential and the closest molecular orbital is approximately constant in alkanedithiol junctions. This result is consistent with previous studies [121] on alkanemonothiol junctions, where a similar length independence was observed.

	$+ V_{trans}$	$- V_{trans}$
Au-HDT-Au	1.39 ± 0.21	-1.37 ± 0.23
Au-ODT-Au	1.35 ± 0.14	-1.40 ± 0.17
Au-DDT-Au	1.37 ± 0.18	-1.44 ± 0.17

Table 1 To obtain statistically meaningful results, positive and negative transition voltages were obtained in ~50 independent single molecule experiments each for Au-HDT-Au, Au-ODT-Au and Au-DDT-Au junctions. The mean value and standard deviation of the measured transition voltages are shown.

3.5 SUPPORTING INFORMATION

3.5.1 Fabrication of the Scanner

A detailed schematic of the fabricated scanner is shown in Figure 3.6. Four piezoelectric tubes (#2 type, EBL products) with an outer diameter of 3.18 mm, wall thickness of 0.76 mm, and length of 11.05 mm are assembled on a molybdenum plate as shown in Figure 3.6. All the piezoelectric tubes have four quadrant gold electrodes on the outer surface and one gold electrode that completely covers the inner surface. Sapphire rings (R152.4, Swiss Jewel) are used to electrically isolate the piezoelectric tubes from the molybdenum base plate, from the tungsten balls located on the top of the outer piezoelectric tubes, and from the STM tip socket located on the top of the inner piezoelectric tube.

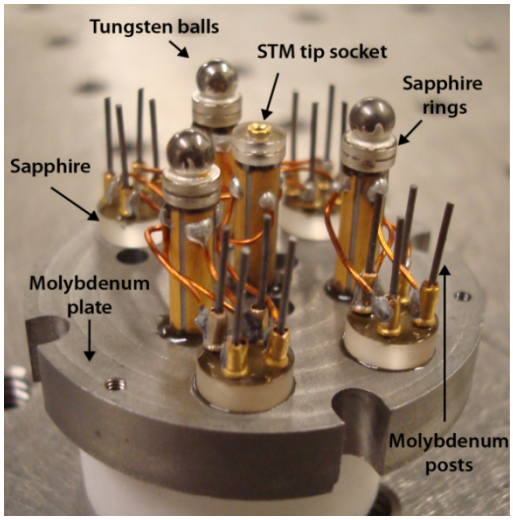

Figure 3.6 The Besocke scanner used in this work. The copper crosspiece with the magnets is not shown in this picture.

All the parts (piezoelectric tubes, sapphire rings, tungsten balls) were assembled with either a thermally conducting but electrically insulating epoxy (H74F, Epotek), or an electrically conducting silver epoxy (H21D, Epotek). Molybdenum posts (see Figure 3.6)

are employed to enable the formation of electrical contact with the piezoelectric tubes while minimizing the mechanical coupling introduced by the electrical contacts. Specifically, polyimide coated copper wires (0.38mm diameter) are connected from the electrodes on the piezoelectric tubes to the molybdenum posts (See Figure 3.6). Later, polyimide coated copper wires that are much thinner (0.13mm diameter, not shown in Figure 3.6) are connected from the molybdenum posts and are thermally anchored to the copper enclosure. The use of the thinner (more compliant) wires decreases the mechanical coupling between the scanner and the copper enclosure. All the wires were soldered using 157, Eutectic Castolin.

3.5.2 Estimation of the Thermal Drift in the Scanner

Any drift between the sample plate and the STM tip is detrimental to the mechanical stability of the molecular junction. Although the Besocke scanner is designed to have good thermal compensation, temperature variations can still affect the tunneling gap distance between the STM tip and the sample plate. This thermal drift arises primarily due to the differences in the thermal expansion coefficients of the gold tip, the tungsten balls and the molybdenum sample plate shown in Figure 3.7. The thermal expansion coefficient of gold, tungsten, and molybdenum are 14.2×10^{-6} /K, 4.5×10^{-6} /K, and 4.8×10^{-6} /K, respectively [126]. Given the length of the STM tip (10.8 mm), the diameter of the tungsten balls (3 mm) and the height of the ramp on the molybdenum sample plate (2.13 mm), the change in the tunneling gap is estimated to be ~130 nm when the temperature of the scanner varies by 1 K. Given the ± 1mK stability achieved using the temperature controller (discussed in more detail in Section 3.5.6), we estimate that the RMS value of the drift in the tunneling gap to be ~0.10 nm.

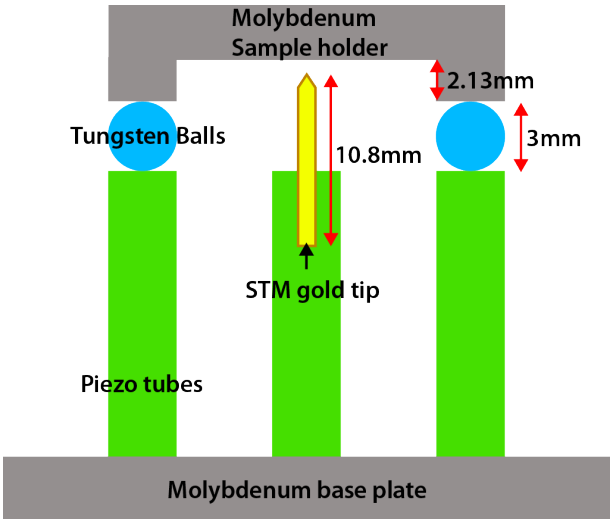

Figure 3.7 Dimensions of the STM tip and tungsten balls are shown. The drift between the STM tip and the sample plate due to temperature variations is estimated to be ~130 nm/K.

3.5.3 Description of Vibration Isolation

In order to suppress the effect of environmental vibrations, the STM scanner is suspended by custom-made stainless steel springs. The natural frequency of the suspended STM head is ~3 Hz. This allows for an effective suppression of all ground vibrations above 3 Hz. Since all the other parts of the scanner are designed to have resonant frequencies >1 kHz, vibrations with frequencies <3 Hz that propagate through the springs do not affect the stability of the scanner [113,116]. Further, ground vibrations that couple to the scanner are attenuated by an eddy current damper (Figure 3.1) that is integrated into the scanner. The strategy adapted by us here has been described in detail elsewhere [113,116] and was found to be effective in attenuating the effect of ground vibrations.

To minimize the effect of acoustic vibrations on the STM scanner, the scanner was placed in a vacuum chamber. The entire STM was located on a vibration isolation table to

further attenuate the effect of ground vibrations. In addition, the STM was operated in the basement of a building with low intensity of ground vibrations (identified by measuring the power spectral density of vibrations using an accelerometer).

3.5.4 Relative Contribution of Conduction and Radiation to the Thermal Conductance between the STM Scanner and the Ambient

In order to minimize the effect of ambient temperature variations on the drift of the scanner, it is necessary to identify the primary modes/channels of heat transport from the STM scanner to the ambient. Since the experiment is conducted under a high vacuum environment ($<10^{-6}$ torr), heat transfer by convection is negligible. However, heat transfer via conduction and radiation are appreciably large. Heat is transported through the copper wires and stainless steel springs attached to the scanner via conduction. We estimated the combined thermal conductance of the springs and wires to be ~1 mW/K (using Fourier's law of heat conduction [100]). The effective thermal conductance, due to radiation, between the scanner surface and the ambient was estimated to be ~50 mW/K (using Stefan-Boltzman law [100]). In order to reduce the effective thermal coupling with the ambient, we used a copper enclosure (Figure 3.8) whose temperature was actively controlled (explained in Section 3.5.6). All the wires and springs attached to the scanner were thermally anchored to the copper enclosure, thus effectively eliminating heat transport via conduction from the scanner to the ambient. Further, the copper enclosure acted as a radiation shield, which reduced the thermal coupling between the scanner and the ambient to < 0.5 mW/K (computed using a simple resistance network model of radiative transport [100]). Therefore, by employing the copper enclosure the effective thermal coupling with the ambient is reduced dramatically.

3.5.5 Description of Radiation Shield (copper enclosure)

Maintaining the temperature of the entire radiation shield at a constant value is the key to minimizing the temperature change and temperature related drift in the STM scanner. In order to accomplish this, we constructed a radiation shield using high thermal conductivity OFHC copper. Further, a low thermal conductivity Teflon plate was used to isolate the copper enclosure form the stainless steel base plate as shown in Figure 3.8. In order to actively control the temperature of the radiation shield, we integrated an electrical heater and a temperature sensor (thermistor) into the copper enclosure (Figure 3.8). The thermistor and the heater were located in close proximity to each other to minimize the delay in the detection of temperature changes in the heater. The strategy adapted for controlling the temperature of the radiation shield is described next.

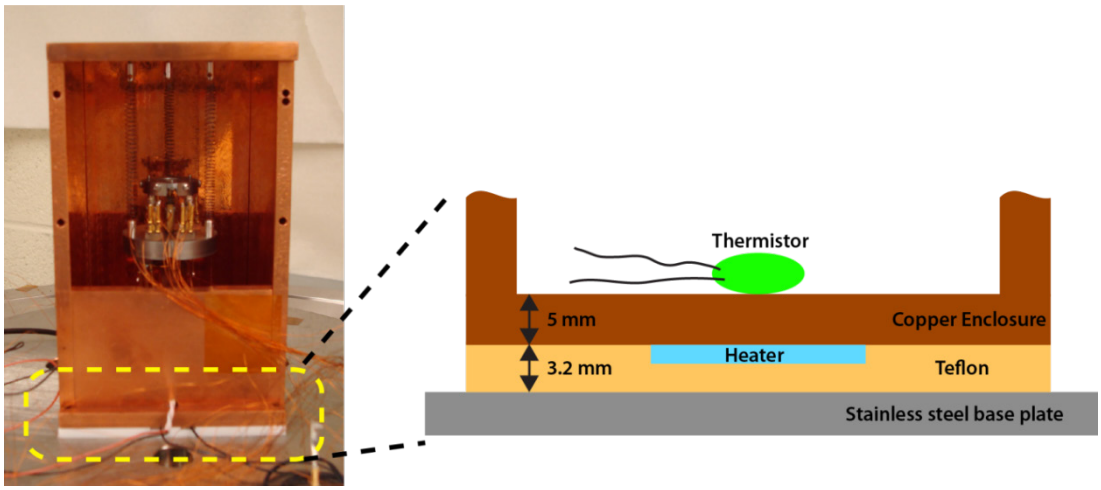

Figure 3.8 The schematic of the thermistor and the heater embedded in the radiation shield. The thermistor is located close to the heater to minimize the delay of temperature response. The Teflon separator serves to thermally isolate the radiation shield from the stainless steel base plate.

3.5.6 Design and Performance of the Temperature Controller

The control circuit employed for maintaining the temperature of the radiation shield at a temperature that is ~5 K above the average ambient temperature (25 K) is shown in Figure 3.9. The circuit shows a thermistor that is used to monitor the temperature changes of the copper enclosure. A PI (proportion and integral) controller implemented on a personal computer detects changes in the temperature of the copper enclosure and modulates the electrical current supplied to the heater to annul the temperature changes. A thermistor was chosen to detect temperature changes because it has more sensitivity than other temperature sensors such as resistive thermal devices (RTD), thermocouples, and integrated circuit temperature sensors. With the circuits and PI controller described above, it was possible to maintain the temperature of the copper enclosure at 30 K ± 1 mK for more than 3 hours.

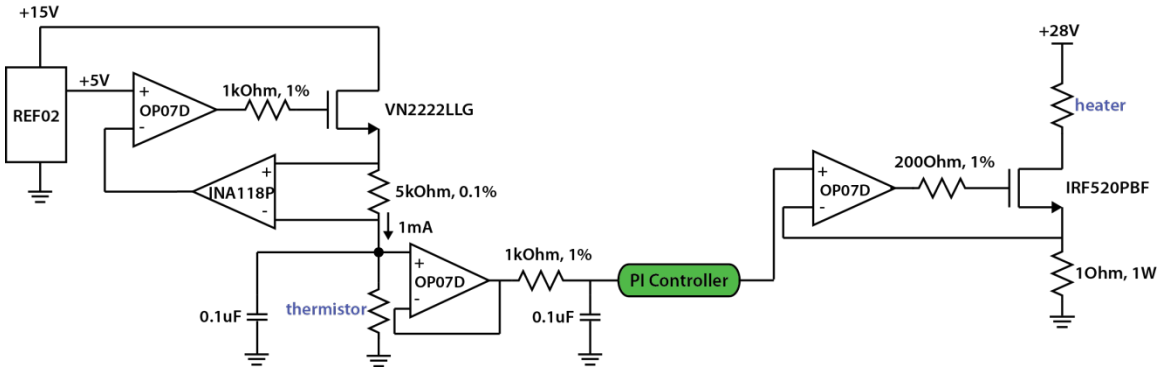

Figure 3.9 The circuit employed for temperature control. The proportional and integral controller measures the temperature of the copper radiation shield and outputs a voltage that modulates the current flow through the heater located on the bottom of the radiation shield. The modulation of the electrical current acts to annul the temperature changes of the copper enclosure.

3.5.7 Histograms corresponding to Au-HDT-Au and Au-DDT-Au Junctions

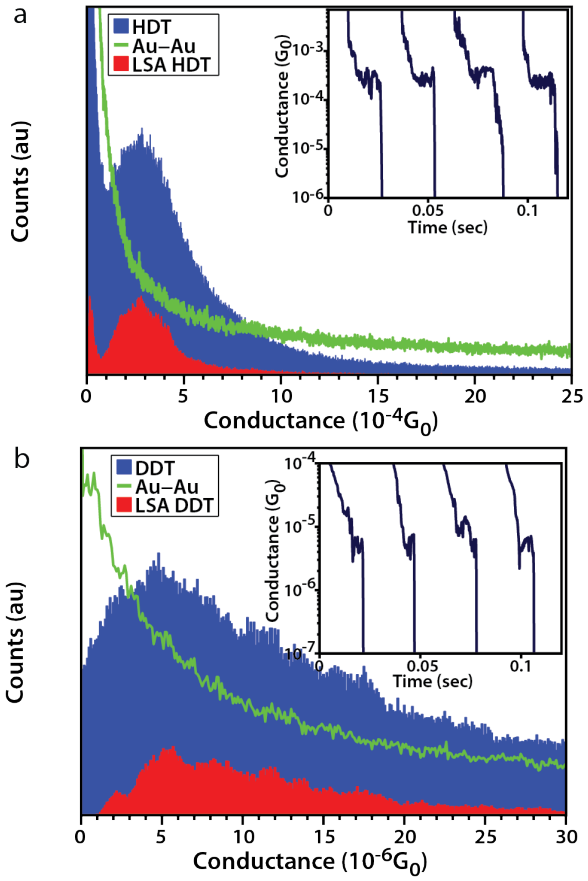

Figure 3.10 Histograms used to obtain the electrical conductance of Au-HDT-Au and Au-DDT-Au single-molecule junctions. Conductance histogram were created from 1000 experiments each on Au-hexanedithiol-Au junctions, Au-decanedithiol-Au junctions. The conventional conductance histograms show peaks at ~2.7 ×10^{-4} G_0(HDT) and ~5.2 × 10^{-6} G_0(DDT), respectively. Conductance histograms obtained in a control experiment where molecules were not present (green) shows no peak. Conductance histograms obtained from last step analysis (red) show a peak at ~2.8 × 10^{-4} G_0(HDT) and ~5.5 × 10^{-6} G_0(DDT), respectively. Representative conductance traces obtained in experiments with HDT, DDT molecules are shown in the insets (withdrawal rate ~30 nm/sec).

3.5.8 Length Dependence of the Resistance of Au-Alkanedithiol-Au Junctions

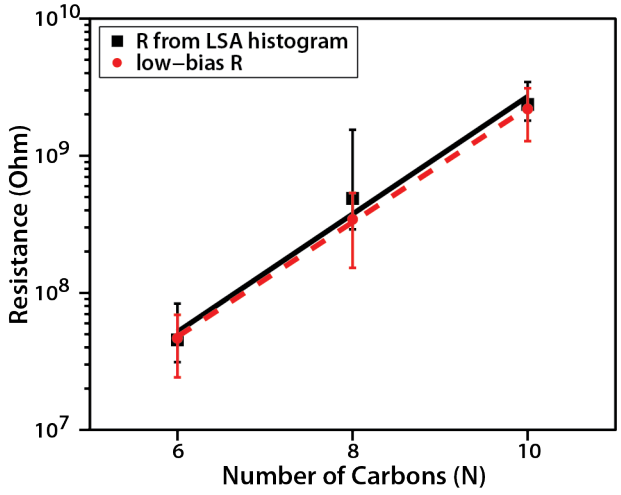

Figure 3.11 Resistance of Au-single molecule-Au junctions vs the number of carbon atoms in alkanedithiol chains (HDT has 6 carbon atoms, ODT has 8 carbon atoms, DDT has 10 carbon atoms). The black squares represent the resistance obtained from the conductance histogram (LSA analysis), whereas the red dots represent the resistance obtained by averaging the low-bias resistances obtained from symmetric I-V curves (i.e. I-V curves that show V_{trans} of similar magnitude for positive and negative bias). The measured resistance is found to increase exponentially with length. The exponential decay constant (β) is 0.99 for the black line fit and 0.96 for the red dashed line fit.

3.6 Discussion and Conclusion

We described a custom built STM, which enables the formation of molecular junctions that are mechanically stable for time periods as long as two minutes at room temperature. This represents at least an order-of-magnitude improvement over the stability observed in past STMBJ measurements. This improvement is accomplished by incorporating a Besocke scanner, which is relatively immune to temperature variations, by active control of the temperature, and by attenuating the effect of acoustic and ground vibrations. We demonstrated the utility of this stable instrument by performing transition voltage

spectroscopy at the single-molecule level. We believe that this improved stability will not only enable more detailed electrical transport studies such as transition voltage spectroscopy at the single-molecule level but will also facilitate the study of thermoelectric and thermal transport phenomena in molecular junctions, where it is necessary to perform measurements for long time periods to improve the signal-to-noise ratio. In fact, one of the major goals of our future work is to integrate this ultra-stable STM with a picowatt-resolution calorimeter [109] to probe heat transport in molecular junctions with picowatt resolution.

Chapter 4

Heat Dissipation in Atomic-Scale Junctions

Reproduced with permission from *Nature*
Woochul Lee, Kyeongtae Kim, Wonho Jeong, Linda Angela Zotti, Fabian Pauly, Juan Carlos Cuevas, and Pramod Reddy, *Nature*, 2013, 498, 209 [127].
Copyright 2013, Nature Publishing Group.

4.1 ABSTRACT

Atomic and single-molecule junctions represent the ultimate limit to the miniaturization of electrical circuits [1]. They are also ideal platforms for testing quantum transport theories that are required to describe charge and energy transfer in novel functional nanometer-scale devices. Recent work has successfully probed electric and thermoelectric phenomena [11,20,21,49,95,128,129] in atomic-scale junctions. However, heat dissipation and transport in atomic-scale devices remain poorly characterized owing to experimental challenges. Here we use custom-fabricated scanning probes with integrated nanoscale thermocouples to investigate heat dissipation in the electrodes of single-molecule ('molecular') junctions. We find that if the junctions have transmission characteristics that are strongly energy dependent, this heat dissipation is asymmetric—that is, unequal between the electrodes—and also dependent on both the bias polarity and the identity of the majority charge carriers (electrons versus holes). In contrast, junctions consisting of only a few gold atoms ('atomic junctions') whose transmission

characteristics show weak energy dependence do not exhibit appreciable asymmetry. Our results unambiguously relate the electronic transmission characteristics of atomic-scale junctions to their heat dissipation properties, establishing a framework for understanding heat dissipation in a range of mesoscopic systems where transport is elastic—that is, without exchange of energy in the contact region. We anticipate that the techniques established here will enable the study of Peltier effects at the atomic scale, a field that has been barely explored experimentally despite interesting theoretical predictions [5,40,81]. Furthermore, the experimental advances described here are also expected to enable the study of heat transport in atomic and molecular junctions—an important and challenging scientific and technological goal that has remained elusive [68,130].

4.2 HEAT DISSIPATION IN ATOMIC-SCALE JUNCTIONS

Charge transport is always accompanied by heat dissipation (Joule heating). This process is well understood at the macroscale, where the power dissipation (heat dissipated per unit time) is volumetric and is given by $j^2\rho$, where j is the magnitude of the current density and ρ is the electrical resistivity. Heating in atomic-scale junctions is expected to be fundamentally different, as charge transport through such junctions is largely elastic [131,132]. Recent experiments have probed the local non-equilibrium electronic and phononic temperatures in molecular junctions [22-24] to obtain insights into the effect of electron-electron and electron-phonon interactions on heat dissipation at the atomic scale. However, experimental challenges in quantitatively measuring atomic-scale heat dissipation have impeded the elucidation of a fundamental question: What is the relationship between the electronic transmission characteristics of atomic and molecular junctions (AMJs) and their heat dissipation properties?

In this work, we overcome this challenging experimental hurdle by using custom-fabricated nanoscale–thermocouple integrated scanning tunneling probes (NTISTPs) shown in Figure 4.1a and b. The NTISTPs feature an outer gold (Au) electrode that is electrically isolated but thermally well connected to the integrated gold-chromium thermocouple via a thin (70 nm) silicon nitride film (see Section 4.4.1 for fabrication details). To probe heat dissipation, we first created a series of AMJs (see Figure 4.1c) between the outer Au electrode of the NTISTP and a flat Au substrate. Application of a voltage bias across such AMJs results in a temperature rise of the integrated thermocouple due to heat dissipation in the NTISTP's apex on a length scale comparable to the inelastic mean free path of electrons in Au[15]. The power dissipation in the probe (Q_P) and the temperature rise of the thermocouple (ΔT_{TC}), located ~300 nm away from the apex, are directly related by $Q_P = \Delta T_{TC} / R_P$ (see Methods), where R_P is the thermal resistance of the NTISTP (see Figure 4.1b). Further, ΔT_{TC} is related to the thermoelectric voltage output of the thermocouple (ΔV_{TC}) by $\Delta V_{TC} = -S_{TC} \times \Delta T_{TC}$, where S_{TC} is the effective Seebeck coefficient of the thermocouple. We note that R_P and S_{TC} were experimentally determined to be 72800 ± 500 K/W and 16.3 ± 0.2 μV/K, respectively (see Section 4.4).

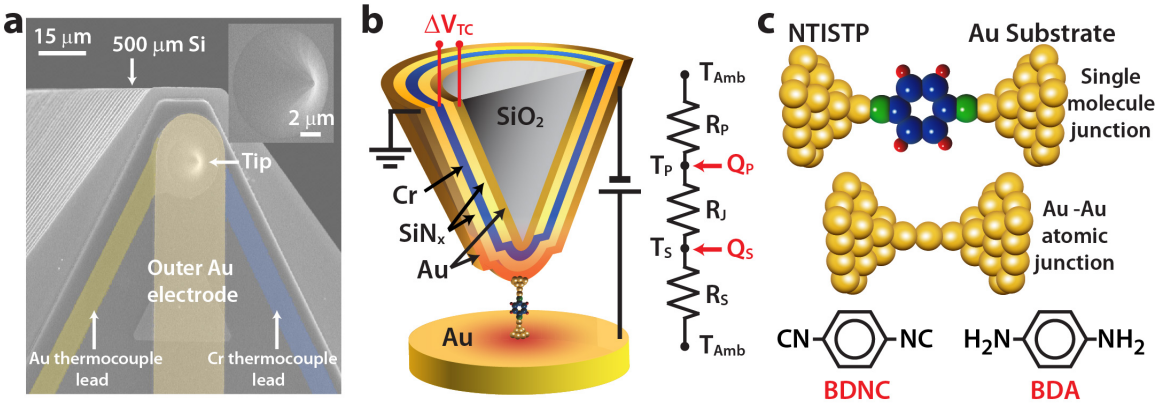

Figure 4.1 Nanoscale thermocouple probes and atomic and molecular junctions studied in this work. ***(a)*** *Scanning electron microscope (SEM) image of a NTISTP. The electrodes are false-colored. Inset, magnified image of the tip.* ***(b)*** *Diagram of a junction created between the NTISTP (cross-sectional view) and a Au substrate (bottom) along with a thermal resistance network (right) that represents the dominant resistances to heat flow.* ***(c)*** *Diagrams of molecular and atomic junctions (top) along with the structures of the molecules studied. (All diagrams are not drawn to scale or proportion).*

We began our experimental studies, at room temperature, by trapping single molecules of 1,4-benezenediisonitrile (BDNC, see Figure 4.1c) between the Au electrodes of the NTISTP and the substrate using a break junction technique[11,89]. We first obtained electrical conductance versus displacement traces by monitoring the electrical current under an applied bias while the NTISTP-substrate separation was systematically varied. Figure 4.2a shows representative conductance traces along with a histogram obtained from 500 such curves. The histogram features a peak at ~0.002G_0 ($G_0 = 2e^2/h \approx$ (12.9 kΩ)$^{-1}$), which represents the most probable low-bias conductance of Au-BDNC-Au junctions ($G_{Au\text{-}BDNC\text{-}Au}$) and is in good agreement with past work[133].

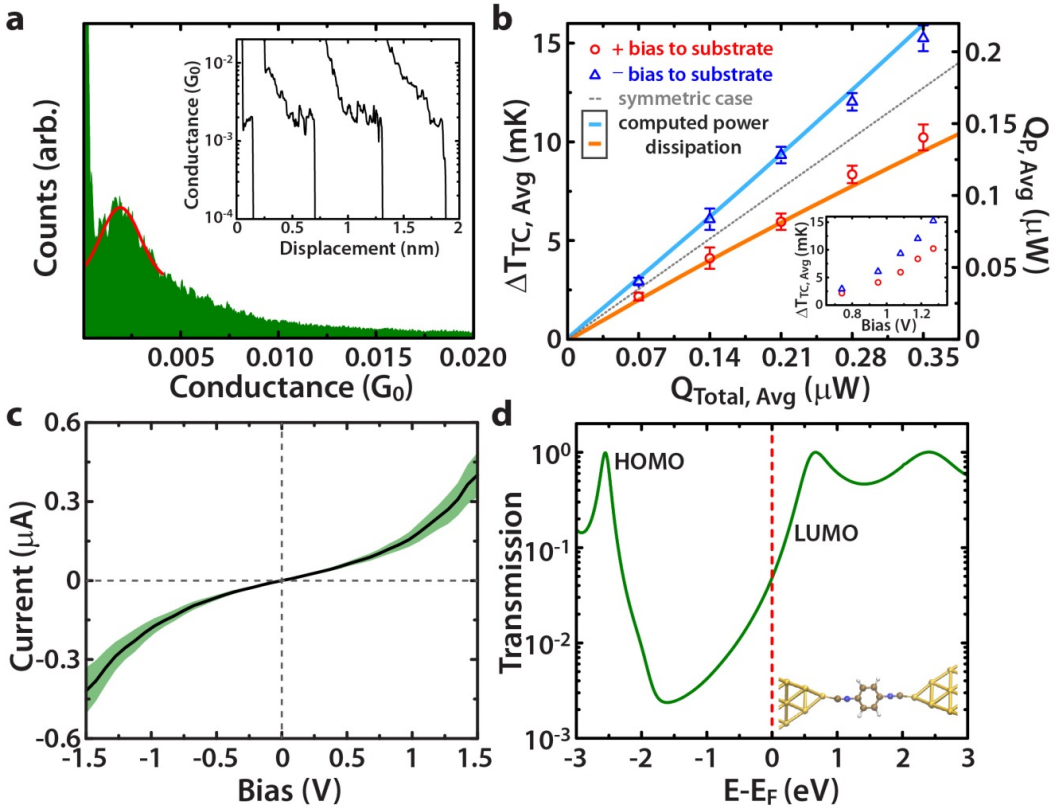

Figure 4.2 Relationship between heat dissipation asymmetries and electronic transmission characteristics in Au-BDNC-Au junctions. ***(a)*** *Horizontally offset conductance traces (inset) of BDNC junctions, along with a histogram obtained from 500 traces(main panel). The red line represents a Gaussian fit to the histogram.* ***(b)*** *Main panel, measured time-averaged temperature rise of the thermocouple ($\Delta T_{TC,\,Avg}$) and the time-averaged power dissipation in the probe ($Q_{P,\,Avg}$) as a function of the time-averaged total power dissipation in the junction ($Q_{Total,\,Avg}$) for positive and negative biases. Error bars represent the estimated uncertainty in $\Delta T_{TC,\,Avg}$ (see Section 4.4 for details of uncertainty estimation). The computationally predicted relationship between Q_P and Q_{Total} is shown by solid lines, which illustrates that $Q_P = f \times Q_{Total}$, where f is dependent on both Q_{Total} and the polarity of the applied bias, and is in general not equal to 0.5. The dotted line corresponds to the expected temperature rise of the probe if the heating was symmetric (that is, f=0.5). Inset, measured $\Delta T_{TC,\,Avg}$ as a function of the magnitude of the applied voltage bias. Uncertainties are not shown in the inset, for visual clarity.* ***(c)*** *I-V characteristics of Au-BDNC-Au junctions obtained by averaging 100 individual I-V curves (solid curve). The shaded region represents the standard deviation of the I-V curves.* ***(d)*** *Computed zero-bias transmission function corresponding to the Au-BDNC-Au junction shown in the inset. HOMO, highest occupied molecular orbital; LUMO, lowest unoccupied molecular orbital.*

To probe heat dissipation, we created stable Au-BDNC-Au junctions with a conductance that is within 10% of the most probable low-bias conductance[89]. We studied heat dissipation in 100 distinct Au-BDNC-Au junctions, at each bias, to obtain the time-averaged temperature rise ($\Delta T_{TC,\ Avg}$) and the time-averaged power dissipation in the NTISTP ($Q_{P,\ Avg}$) for both positive and negative biases. Here, a positive (negative) bias corresponds to a scenario where the probe is grounded, while the substrate is at a higher (lower) potential. We note that a modulated voltage bias was applied to the junctions to obtain $\Delta T_{TC,\ Avg}$ —with high resolution—for both positive and negative biases (see Section 4.3 and Section 4.4). This modulation scheme enables rejection of broadband noise and plays a critical role in performing high-resolution thermometry.

The circles (triangles) in Figure 4.2b represent the measured $\Delta T_{TC,\ Avg}$ as well as the estimated $Q_{P,\ Avg}$ for positive (negative) biases as a function of the time-averaged toal power dissipation in the junctions ($Q_{Total,\ Avg}$) at each bias voltage. Here, $Q_{Total,\ Avg}$ represents all the power dissipated in the junction, at a given bias voltage, and can be readily obtained from the measured current (I) and the known voltage bias (V) applied to the junction (see Section 4.3). We note that the current-voltage (I-V) characteristics of Au-BDNC-Au junctions are nonlinear (Figure 4.2c), therefore, in general $Q_{Total,\ Avg} \neq G_{Au-BDNC-Au}V^2$. The dotted line in Figure 4.2b corresponds to the expected temperature rise of the probe if the heating was symmetric, that is, if half of the total power was dissipated in the probe ($\Delta T_{Symmetric} = Q_{Total,\ Avg} / 2R_P$). It can be clearly seen that for a given $Q_{Total,\ Avg}$ the power dissipation in the probe is larger under a negative bias than a positive bias. We also conclude that the time-averaged power dissipation in the substrate, $Q_{S,\ Avg}$, is smaller under a negative bias than under a positive bias, because $Q_{P,}$

$_{Avg}$+ $Q_{S,\,Avg}$=$Q_{Total,\,Avg}$. To clarify the voltage biases used in the experiments, we present (in the inset of Figure 4.2b) $\Delta T_{TC,\,Avg}$ as a function of the magnitude of the applied voltage bias. These results unambiguously demonstrate that heat dissipation in the electrodes of Au-BDNC-Au junctions is bias polarity dependent and unequal.

This observation raises an important question: Why is the heat dissipation in the electrodes unequal in spite of the symmetric geometry of the molecular junctions? To address this question, we resort to the Landauer theory of quantum transport, which has successfully described charge transport in numerous nanostructures[15]. Within this theory, the power dissipated in the probe and the substrate, $Q_P(V)$ and $Q_S(V)$, respectively, is given by[134]

$$\begin{aligned} Q_P(V) &= \frac{2}{h}\int_{-\infty}^{\infty}(\mu_P - E)\tau(E,V)[f_P - f_S]dE \\ Q_S(V) &= \frac{2}{h}\int_{-\infty}^{\infty}(E - \mu_S)\tau(E,V)[f_P - f_S]dE \end{aligned} \quad . \tag{4.1}$$

Here, μ_P and μ_s are the chemical potentials of the probe and substrate electrodes, respectively, $f_{P/S}$ represent the Fermi-Dirac distribution of the probe/substrate electrodes, and $\tau(E,V)$ is the energy (E) and voltage bias (V) dependent transmission function. Eq. (4.1) suggests that the power dissipation in the two electrodes is, in general, unequal, that is, $Q_P(V) \neq Q_s(V)$, and bias polarity dependent, that is, $Q_{P/S}(V) \neq Q_{P/S}(-V)$. Specifically, it is straightforward to show that:

$$\begin{aligned} Q_P(V) - Q_P(-V) &\approx 2GTSV + O(V^3) \\ Q_P(V) - Q_S(V) &\approx 2GTSV + O(V^3) \end{aligned} \tag{4.2}$$

Here, G is the low bias electrical conductance of the junctions, T is the absolute temperature, and S is the Seebeck coefficient of the junction, whose sign is related to the first energy derivative of the zero-bias transmission $\tau'(E = E_F, V = 0)$ at the Fermi energy (E_F), resulting in a positive Seebeck coefficient for a negative first derivative and vice versa[53]. To test if the observed heating asymmetry can be understood within this framework, we computed $\tau(E, V = 0)$ for Au-BDNC-Au junctions using a transport method[135] based on density functional theory (DFT; see Section 4.4). The computed transmission function (Figure 4.2d) exhibits a positive slope at the Fermi energy, in agreement with past work[51], indicating a negative Seebeck coefficient, which by virtue of Eq. (4.2) leads to higher power dissipation in the NTISTP when negative voltages are applied to the substrate. Further, the solid lines in Figure 4.2b represent the relationship between Q_P and Q_{Total} (Q_P + Q_s = Q_{Total}) as computed from Eq. (4.1) under the assumption that $\tau(E,V)$ is well approximated by $\tau(E, V = 0)$. Notice that although our DFT approach overestimates the linear conductance, it describes correctly the relationship between Q_P and Q_{Total}. The reasons for this agreement are discussed further in the Section 4.4, where we show in particular that this relation is relatively insensitive to the details of the junction geometry. The good agreement of the computed and measured relation between power dissipations provides strong support to the applicability of the Landauer theory of heat dissipation at the atomic scale.

To prove conclusively the relationship between electronic structure and heat dissipation, we performed additional studies in 1,4-benzenediamine (BDA, see Figure 4.1c) junctions, which are expected to exhibit hole-dominated electrical transport, as suggested by our calculations (Figure 4.3d) and past experiments[94]. Following a procedure similar to

that described above, we first determined that the most probable low-bias conductance of Au-BDA-Au junctions was ~0.005G_0 (Figure 4.3a), a value consistent with past work[136]. Measurements of heat dissipation in BDA junctions (Figure 4.3b) show a remarkably different asymmetry. In particular, the BDA junctions show larger power dissipation in the probe for a positive bias than for a negative one—in strong contrast to that observed in BDNC junctions. To understand this important difference we computed the transmission function of the Au-BDA-Au junction displayed in Figure 4.3d, which shows that $\tau'(E = E_F, V = 0)$ is negative resulting in a positive Seebeck coefficient. This, in turn, leads to larger power dissipation in the NTISTP at positive biases. Further, the computed relationship between Q_P and Q_{Total} is in good agreement with our experimental observations (solid lines in Figure 4.3b).

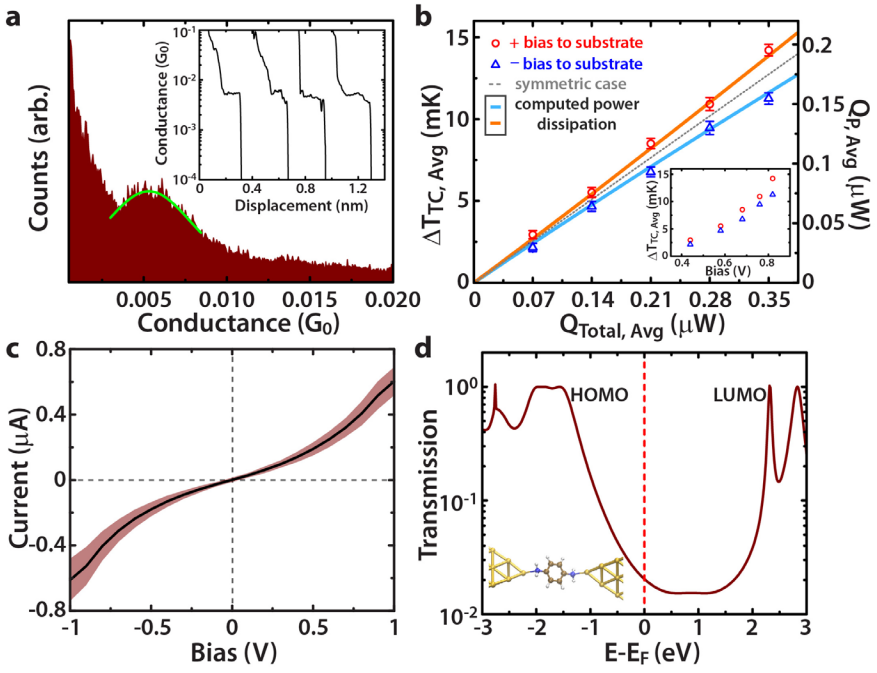

Figure 4.3 Heat dissipation asymmetry for Au-BDA-Au junctions. (a - d) Same as Figure 4.2 but for Au-BDA-Au junctions. In contrast to Au-BDNC-Au junctions, the heat dissipated in the probe is found to be larger for positive biases than for negative ones.

Finally, to prove the fact that no appreciable asymmetries are obtained if the transmission is weakly dependent on energy, we studied heat dissipation in Au-Au atomic junctions. We began our analysis by studying the conductance of Au-Au atomic junctions, which were found to have a most probable conductance of $\sim G_0$, in accordance with past studies[11,137] (see Section 4.4). Subsequently, we created 100 Au-Au atomic junctions with a low-bias conductance of $G_0 \pm 0.1G_0$ and probed heating in them. The measured $\Delta T_{TC,\ Avg}$ (Figure 4.4a) is seen to be proportional to $Q_{Total,\ Avg}$ and is identical for both positive and negative biases (within experimental uncertainty, ~0.1 mK), clearly demonstrating that there is no detectable asymmetry in the power dissipation. Further, additional experiments performed at larger values of $Q_{Total,\ Avg}$ also show no detectable asymmetry (see inset of Figure 4.4a).

Symmetric heat dissipation is indeed expected in Au-Au atomic junctions because of the weak energy dependence of their transmission function[138], which is reflected in the fact that their average thermopower vanishes[129]. In Figure 4.4b we present the computed zero-bias transmission, corresponding to the Au-Au atomic junction shown in inset-i. The transmission is practically energy independent over 1 eV around the Fermi energy. This weak energy dependence results in symmetric power dissipation (from Eqs (4.1) and (4.2)) as well as linear *I-V* characteristics, as evidenced by the experimentally obtained *I-V* curves shown in inset-ii of Figure 4.4b.

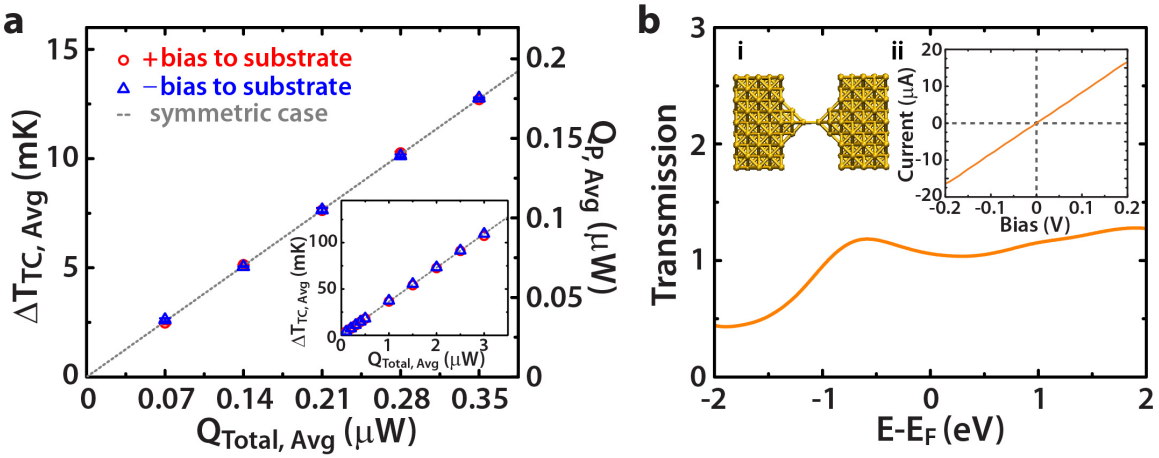

Figure 4.4 No detectable heating asymmetry in Au-Au atomic junctions. ***(a)*** *The measured* $\Delta T_{TC,\ Avg}$ *and* $Q_{P,\ Avg}$ *in Au-Au atomic junctions for positive and negative biases as a function of* $Q_{Total,\ Avg}$ *(uncertainty of* $\Delta T_{TC,\ Avg}$ *is <0.1 mK for all voltage biases). Inset, results of similar measurements for a larger range of powers (uncertainty is <0.1 mK and is imperceptible in the figure). The measured temperature rise is found to be linearly dependent on* $Q_{Total,\ Avg}$ *and is independent of the bias polarity within experimental uncertainty. Further,* $Q_{P,\ Avg} = Q_{Total,\ Avg} / 2$ *irrespective of the bias.* ***(b)*** *The computed transmission function corresponding to the Au-Au atomic junction shown in inset-i features a weak energy dependence around the Fermi energy (*E_F*). Inset-ii shows the experimentally obtained I-V characteristics of Au-Au atomic junction created by averaging over 100 independent I-V curves.*

The good agreement between the measured and computed asymmetries in the heat-dissipation characteristics of AMJs unambiguously confirms that heat dissipation is indeed intimately related to the transmission characteristics of the junctions, as predicted by the Landauer theory. We note that our results contradict recent claims[139] of asymmetric heat dissipation in Au atomic junctions that are not in agreement with theoretical predictions. The insights obtained here regarding heat dissipation should hold for any mesoscopic system where charge transport is predominantly elastic. Such systems

include semiconductor nanowires, two-dimensional electron gases, semiconductor heterostructures, carbon nanotubes, and graphene.

4.3 EXPERIMENTAL METHODS

Single-molecule and atomic junctions were created by displacing the NTISTP towards a Au substrate at 5 nm/s and withdrawing from the substrate at 0.1 nm/s after contact formation (indicated by an electrical conductance greater than $5G_0$). The Au substrate was coated with the desired molecules for molecular experiments and was pristine for the atomic junction studies. To obtain the conductance traces, a voltage bias of 100 mV was applied and the current is monitored during the withdrawal process. The obtained traces were analyzed by creating histograms to identify the most probable conductance of AMJs. Stable single-molecule junctions with a desired conductance were created by stopping the withdrawal when a conductance plateau with a conductance within 10% of the most probable conductance was obtained. All the experiments were performed in an ultrahigh-vacuum scanning probe microscope at ambient temperature. Further, high-resolution temperature measurements were enabled by a modulation scheme where a time-dependent voltage, $V_M(t)$, consisting of a periodic series of three level voltage pulses ($+V_M$, 0 V, $-V_M$; Figure 4.5) was applied to the AMJs while monitoring the thermoelectric voltage output of the NTISTP. The zero-bias transmission functions, (Figure 4.2-4.4) were computed with the *ab initio* method described in Ref. [135]. More detailed methods are given in following sections.

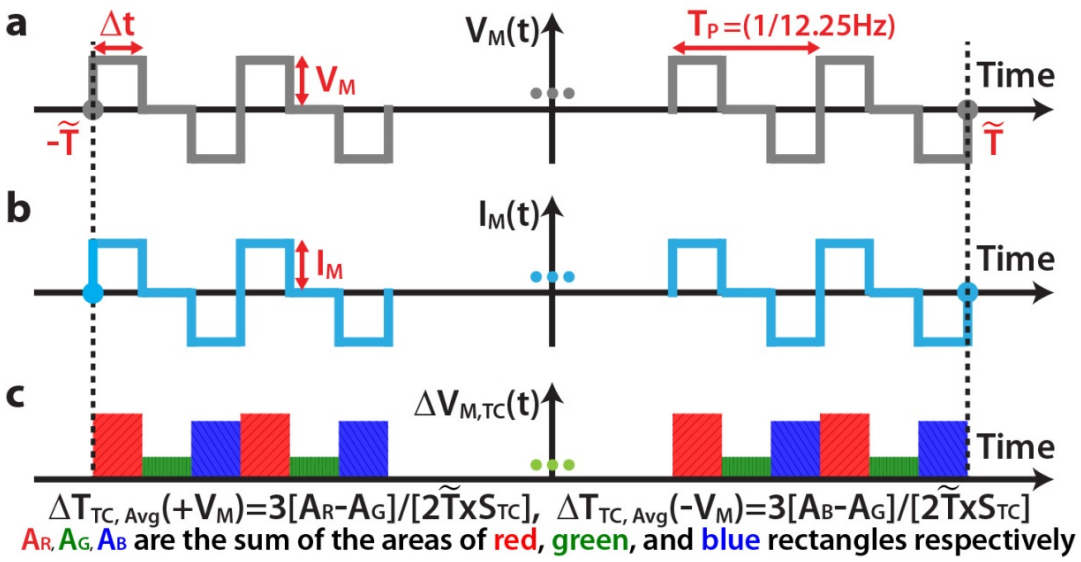

*Figure 4.5 Schematics of the modulation scheme used in this work. (**a**) The modulated periodic voltage signal $V_M(t)$ applied to AMJs. (**b**) The resulting modulated current $I_M(t)$. (**c**) The modulated voltage output $\Delta V_{M,TC}(t)$ from the integrated thermocouple, which is related to the time-averaged temperature rise $\Delta T_{TC,Avg}$ by the relationship shown at the bottom of the figure.*

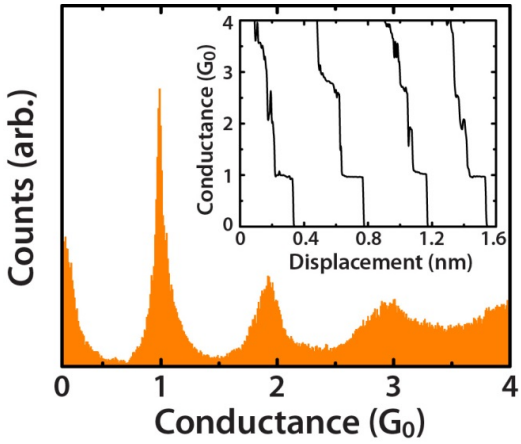

Figure 4.6 The conductance traces (inset) of Au-Au atomic junctions are shown along with a histogram obtained from 500 such traces. The histogram features a prominent peak at G_0 showing the most probable conductance of Au-Au atomic junctions.

4.3.1 Creation of atomic and molecular junctions

All the AMJs were created between NTISTP and a Au-coated substrate by displacing the NTISTP towards a Au substrate (which was coated with the desired molecules in molecular experiments and was pristine in atomic junction experiments) at 5 nm/s and withdrawing from the substrate at 0.1 nm/s after contact formation as indicated by an electrical conductance greater than $5G_0$. To create the desired monolayers, 1 mM solutions of BDNC and BDA molecules, obtained commercially from Sigma Aldrich with a purity of ~99%, were created in toluene/ethanol. Subsequently, a Au coated mica substrate (electron beam evaporation) was placed in one of the solutions to allow self-assembly of molecules on the Au surface. After exposing the substrates for 12 hours in a glove box filled with nitrogen gas, they were rinsed in ethanol and dried in nitrogen gas. For the experiments involving Au-Au atomic junctions, the Au-coated substrates were cleaned with ultraviolet-radiation ozone to eliminate any organic contamination on the surface. The NTISTPs were also cleaned with ultraviolet-radiation ozone in all studies and loaded into the UHV scanning probe microscope instrument. The measurement of electrical current was performed using a current amplifier (Keithley 428), whereas thermoelectric voltage measurements were performed using a voltage amplifier (Stanford Research System 560). All the data was collected at a sampling frequency of 2 kHz using a data acquisition system (National Instruments 6281). The approach, withdraw, and hold sequences were accomplished by employing a real-time controller (National Instruments PXI8110).

4.3.2 Measurement of $\Delta T_{TC, Avg}$ using a modulation scheme

High-resolution temperature measurements are enabled by a modulation scheme where a time-dependent voltage, $V_M(t)$, consisting of a periodic series of three level voltage pulses $+V_M$, 0 V, $-V_M$, (Figure 4.5) is applied. In all the experiments performed in this work, the period (T_P) of the voltage pulses was chosen to be ~0.08 s (1/12.25 Hz). The selected modulation frequency is found to optimize the signal-to-noise ratio and is experimentally feasible owing to the small thermal time constants (~10 μs) of the micrometer sized NTISTPs, which enables high-fidelity tracking of temperature changes. The applied $V_M(t)$ results in both a modulated current ($I_M(t)$; see Figure 4.5) and a modulated temperature change of the thermocouple ($\Delta T_{M, TC}(t)$) due to Joule heating. Using the equation at the bottom of Figure 4.5, the temperature rise corresponding to a positive bias $\Delta T_{TC, Avg}(+V_M)$ or a negative bias $\Delta T_{TC, Avg}(-V_M)$ can be directly related to the modulated thermoelectric voltage output ($\Delta V_{M, TC}(t)$) of the thermocouple. In probing heat dissipation in AMJs we applied the modulated voltage signal with appropriately chosen amplitude V_M for a period of ~5 s to each AMJ. The resulting thermoelectric voltage signal $\Delta V_{M, TC}(t)$ was simultaneously recorded. This was repeated on ~100 junctions to collect data for ~500 s for each V_M. The obtained data was concatenated and analyzed to estimate $\Delta T_{TC, Avg}$ corresponding to positive and negative biases as described above. This modulation scheme enables temperature measurements with submillikelvin resolution, as described in Section 4.4. The time-averaged total power dissipation ($Q_{Total, Avg}$), at each bias, was obtained by using the 500-s-long data corresponding to each V_M. Specifically, the data (measured current and know applied bais) were used to first compute the total heat dissipated at positive and negative biases. Subsequently, $Q_{Total, Avg}(+V_M / -V_M)$ was

obtained by dividing the estimated total heat dissipation (corresponding to a positive or a negative bias) by the total time during during which a positive bias ($+V_M$) or negative bias ($-V_M$) was applied (~500/3 s). The amplitudes (V_M) of the three level voltage pulses used in our studies were chosen to be 30 mV, 43 mV, 52 mV, 60 mV, and 67 mV for Au-Au junctions; 0.74 V, 0.95 V, 1.08 V, 1.18V, and 1.27V for Au–BDNC–Au junctions; and 0.44 V, 0.58 V, 0.68 V, 0.76V and 0.82V for Au–BDA–Au junctions. Representative traces obtained in the experiments are shown in Section 4.4.6.1.

4.3.3 Estimating $Q_{P,\,Avg}$ from the measured $\Delta T_{TC,\,Avg}$

To relate the temperature rise of the thermocouple to the time-averaged power dissipation in the probe $Q_{P,\,Avg}$, it is necessary to quantify the thermal resistance of the NTISTP. To elaborate, consider the resistance network shown in Figure 4.1, where the thermal resistances to heat flow in the probe (R_P), junction (R_J), and the substrate (R_S) are identified. R_P was experimentally determined to be 72800 ± 500 K/W (see Section 4.4). The thermal resistances of AMJs (R_J) are estimated to be at least 10^7 K/W for all the AMJs studied here (see Section 4.4 for more details). Thus, $R_J >> R_P$ and therefore, $\Delta T_{TC,\,Avg}$ depends only on the power dissipated in the tip and is unaffected by the heating in the substrate. Thus, from a knowledge of, $\Delta T_{TC,\,Avg}$ and R_P, the time-averaged power dissipation, $Q_{P,\,Avg}$, can be estimated as $Q_{P,\,Avg} = \Delta T_{TC,\,Avg} / R_P$.

4.3.4 Computation of the transmission function

The zero-bias transmission functions shown in Figure 4.2-4.4 were computed with the *ab initio* method described in detail elsewhere [135]. It is based on a combination of non-equilibrium Green's function techniques and density functional theory (DFT) and was

implemented in the quantum-chemistry software package Turbomole. More details can be found in the Section 4.4.

4.3.5 Computing the relationship between Q_P and Q_{Total}

We computed the power dissipated in the probe $Q_P(V)$ and the total power dissipated in the junction Q_{Total} ($Q_P(V) + Q_S(V) = Q_{Total}(V)$) using Eq. (4.1) and the zero-bias transmission curves of the molecular junctions (shown in Figure 4.2d and Figure 4.3d). Subsequently, Q_P was plotted as a function of Q_{Total} as the relationship between Q_P and Q_{Total} is robustly predicted by our calculations (see Section 4.4).

4.4 SUPPLEMENTARY DISCUSSION

4.4.1 Fabrication of Probes

The steps involved in the fabrication of the custom-fabricated NTISTPs are shown in Figure 4.7 and are described next. (Step 1) fabrication begins by depositing a ~500 nm thick low-stress low-pressure chemical vapor deposition (LPCVD) SiN_x on both sides of a silicon wafer. (Step 2) An 8 μm thick layer of low temperature silicon oxide (LTO) is deposited on both sides of the wafer and is annealed at 1000°C for 1 hour to reduce the residual stress of SiN_x and LTO layers (this LTO layer is eventually patterned to create the probe tip). Subsequently, a 100 nm thick chromium (Cr) cap is lithographically patterned by Cr etching: this Cr cap facilitates the creation of the probe tip from the LTO layer by etching. (Step 3) The LTO probe tip is fabricated by etching in buffered HF (HF : NH_4F = 1:5), which takes ~100 minutes. In order to obtain a sharp tip the etching status of the tip is monitored, at 10 minute intervals, by using an optical microscope. (Step 4)

After fabrication of a sharp LTO tip, a gold (Au) line (Cr/Au: 5/90 nm) is lithographically defined by sputtering and Au etching. This Au line is the first metal layer of the NTISTP.

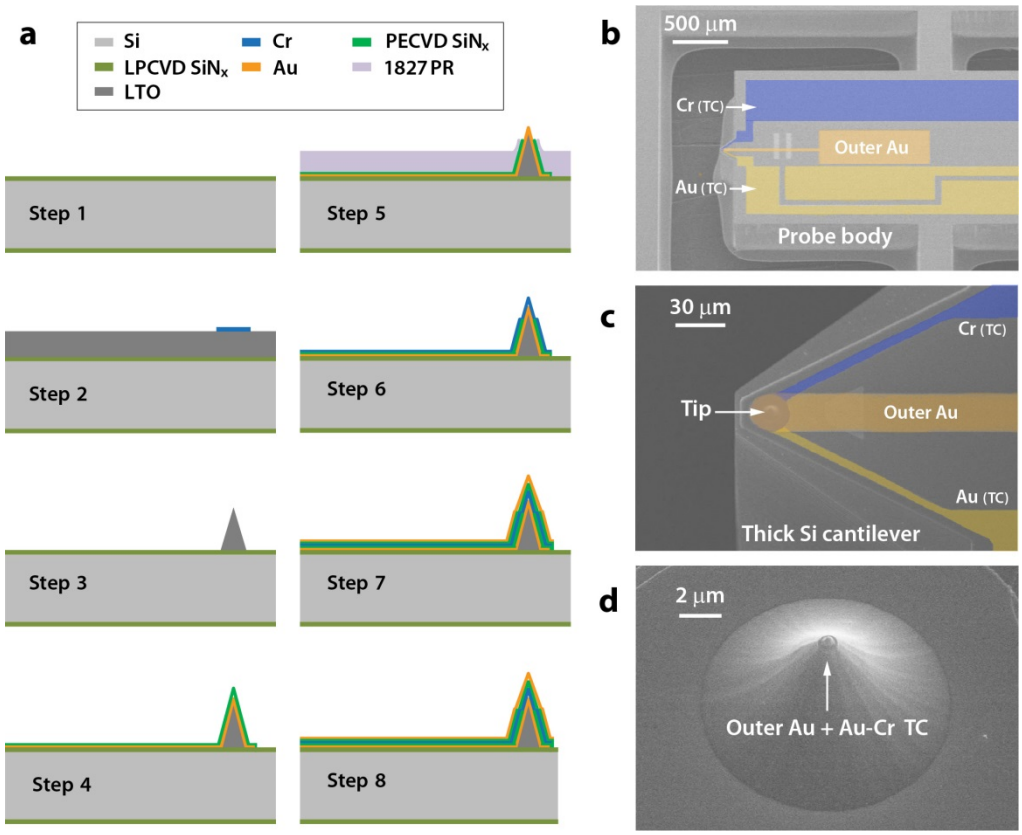

*Figure 4.7 Fabrication of the NTISTPs. **(a)** The fabrication steps involved in the creation of NTISTPs are shown. (**b** & **c**) Scanning electron microscope (SEM) images of fabricated probes. The false coloring identifies the metal layers (Au, Cr) that comprise the thermocouple (TC) and the outermost Au metal layer that is used to create atomic-scale junctions. (**d**) SEM image of the tip of a fabricated NTISTP.*

Subsequently, a 70 nm thick layer of plasma enhanced chemical vapor deposition (PECVD) SiN_x is deposited to insulate the two metal layers (Au which is deposited in step 4 and Cr that is deposited in step 6) everywhere except at the tip of the probe: these metal layers comprise of the nanoscale thermocouple. (Step 5) In order to create a nanoscale thermocouple junction on the apex of the probe tip, a 6 μm thick Shipley

Microposit S1827 photoresist is deposited on the probe. The photoresist and PECVD SiN_x is slowly plasma etched until a very small portion of the Au layer is exposed. (Step 6) A Cr line (~90 nm thick) is deposited by sputtering and is etched after lithography. This Cr line is the second metal layer of the NTISTP and contacts the Au layer only at the apex of the tip. (Step 7) 70 nm thick PECVD SiN_x is deposited to insulate the Cr-Au thermocouple junction from the third metal layer. Finally, a Au layer (Cr/Au: 5/90 nm) is lithographically defined by sputtering and Au etching. This Au layer represents the outermost electrode of the probe and is critical for creating Au-Au atomic junctions and Au-single molecule-Au junctions. (Step 8) In the last step, the NTISTPs are released by deep reactive ion etching (DRIE). Figure 4.7b, c, and d show scanning electron micrograph images of a fabricated NTISTP. We note that the fabricated probes ***are designed to be much stiffer than traditional scanning thermal microscopy probes***[140] so as to enable stable trapping of AMJs.

4.4.2 Landauer Approach: General Considerations

As explained in Section 4.2, within the Landauer approach to coherent transport, the power dissipation (heat dissipation per unit time) in the electrodes of atomic-scale junctions is given by Eq. (4.1). From those expressions, it is straightforward to draw some general conclusions about the symmetry of the dissipated heat (with respect to both the electrodes and the bias polarity). The first question that we want to address concerns the conditions under which the power is equally dissipated in both electrodes $[Q_P(V) = Q_S(V)]$. To answer this question, we assume (without loss of generality) that all the energies are measured with respect to the equilibrium chemical potential, which

we set to zero (μ = 0). Moreover, we assume a symmetric biasing scheme: $\mu_P = eV/2$ and $\mu_S = -eV/2$. Obviously, the conclusions drawn below are independent of this choice since the measurable quantities must be gauge-invariant, *i.e.* independent of the biasing scheme. With this choice, the power dissipated in the probe electrode is given by

$$Q_P(V) = \frac{2}{h}\int_{-\infty}^{\infty}(eV/2 - E)\tau(E,V)[f(E - eV/2) - f(E + eV/2)]dE. \qquad (4.3)$$

Making use of the change of variable $E \to -E$, the previous expression becomes:

$$Q_P(V) = \frac{2}{h}\int_{-\infty}^{\infty}(E + eV/2)\tau(-E,V)[f(E - eV/2) - f(E + eV/2)]dE. \qquad (4.4)$$

Here, we have used the relation $f(-x) = 1 - f(x)$. Eq. (4.4) has to be compared with the corresponding expression for the power dissipated in the substrate,

$$Q_S(V) = \frac{2}{h}\int_{-\infty}^{\infty}(E + eV/2)\tau(E,V)[f(E - eV/2) - f(E + eV/2)]dE. \qquad (4.5)$$

Thus, we conclude that $Q_P(V) = Q_S(V)$ if $\tau(E,V) = \tau(-E,V)$, *i.e.* if the transmission function has inversion symmetry with respect to the chemical potential, or in other words, if the transport is electron-hole symmetric. This in turn implies a trivial linear relation between $Q_P(V)$ and the total power dissipated in the junction $Q_{Total}(V) = I \times V$, namely $Q_P(V) = Q_{Total}(V)/2$. Notice that this relation is independent of the bias dependence of these two powers. Obviously, if the transmission is energy-independent in the transport window, then the power dissipation is the same in both electrodes. This explains the observed heat dissipation properties of Au junctions.

Another central question in our work is related to the asymmetry of the power dissipated in an electrode with respect to the bias polarity. Following a similar line of reasoning as above, one can show that $Q_P(V) = Q_P(-V)$ if $\tau(E,V) = \tau(-E,-V)$ is satisfied. This means, in particular, that if the transmission does not depend significantly on the bias voltage, the power dissipated in an electrode is symmetric with respect to the inversion of the bias as long as there is electron-hole symmetry. Obviously, if the transmission is independent of both the energy and the bias, then the heating is symmetric. This is what occurs in the Au atomic junctions for not too high voltages.

Finally, let us say that, analogously, one can show that the relation $Q_P(V) = Q_S(-V)$ is satisfied if $\tau(E,V) = \tau(E,-V)$. Furthermore, this relation leads naturally to the following one: $Q_P(V) + Q_P(-V) = Q_P(V) + Q_S(V) = Q_{Total} = I \times V$. This means that if the transmission is symmetric with respect to the inversion of the bias voltage, then the average dissipated heat in an electrode (for positive and negative bias) is equal to half of the total power dissipated in the junction. This is in fact the relation that we have found experimentally in all the AMJs analyzed in this work. This is indeed reasonable since all our AMJs are approximately left-right symmetric and therefore, the voltage profile is expected to be symmetric with respect to the center of the junction. This implies, in turn, that the relation $\tau(E,V) = \tau(E,-V)$ will hold in all our AMJs[141].

From the general considerations above, it is clear that in order to have a heating asymmetry of the type $Q_P(V) \neq Q_P(-V)$, one needs a certain degree of the electron-hole asymmetry. This can be seen explicitly by expanding $Q_P(V)$ in Eq. (4.3) to first order in the bias voltage, which gives:

$$Q_P(V) = \frac{2eV}{h}\int_{-\infty}^{\infty} E\tau(E, V=0)\frac{\partial f(E,T)}{\partial E}dE = GTSV. \quad (4.6)$$

Here, G is the low bias electrical conductance of the junction, T is absolute temperature, and S is the thermopower or Seebeck coefficient of the junction. In the same way, one can show that $Q_S(V) = -GTSV$. These expressions lead immediately to the first order terms in Eq. (4.2). Moreover, we can perform a Taylor's expansion in the previous equation to obtain the leading contribution at low temperatures, which reads:

$$Q_P(V) = -\left(\frac{2e}{h}\right)\frac{\pi^2}{3}(k_B T)^2 \tau'(E_F, V=0)V, \quad (4.7)$$

where $\tau'(E_F, V=0)$ is the energy derivative of the zero-bias transmission at the Fermi energy. Thus, we see that the slope of the transmission function determines, to first order in the bias voltage, both the magnitude and the sign of the heating asymmetry.

Our experimental results show that the temperature rise in the probe, and in turn the power dissipated there, is roughly proportional to the total power dissipated in the junction $Q_{Total} = I \times V$. This can be understood by expanding $Q_P(V)$ in Eq. (4.3) up to second order in the bias voltage. Ignoring the bias dependence of the transmission function, the second-order term is given by $(1/2)GV^2$, which is equal to half of the total power in the linear regime. We note that this is also the second order term for $Q_S(V)$, which implies that there is no quadratic term in the bias in Eq. (4.2). This second-order term dominates over the linear one as long as $|V| > 2T|S|$. Thus for instance, if we assume room temperature (T = 300 K) and a typical value of $|S|$ = 10 μV/K, then the second-order term dominates the contribution to the heating for voltages

$|V| > 6$ mV. This explains why the local heating is roughly proportional to the total power dissipated in the junction, at least in a certain voltage range. Of course, at sufficiently high bias, higher order terms in the voltage expansion (beyond the quadratic one) may give a significant contribution to the local heating. In particular, odd terms, like the cubic one, can then play an important role in the heating asymmetry. We can estimate the voltage at which these higher order terms become relevant by expanding Q_P to third order in the bias. Ignoring the voltage dependence of the transmission, one can show that the cubic term is given by $-(1/12)eG_0\tau'(E_F, V=0)V^3$. Notice first that this term is also determined by the energy derivative of the transmission at the Fermi energy, in the spirit of Eq. (4.7). Comparing this contribution with the linear one of Eq. (4.7), we see that the third order term would dominate the contribution to the heating asymmetry at room temperature for biases above approximately 0.2 V. Thus, contributions of non-linear terms to the heating asymmetry of our molecular junctions are indeed expected to show up in the voltage range explored in our experiments, as it indeed occurs (see insets of Figure 4.2b and Figure 4.3b). We note that all these contributions are completely taken into account by the exact expressions for the power dissipated in the electrodes (Eq. (4.1)), as we have done in all the calculations presented in Section 4.2 and in the next section.

4.4.3 *Ab Initio* Calculations: Atomic and Molecular Junctions

The goal of this section is to describe the procedure that we have followed in the *ab initio* calculations of the transmission curves of the different systems discussed in the main text: gold atomic junctions and single-molecule junctions. We have employed our transport method based on density functional theory (DFT), which has been described in

great detail[135]. This method is built upon the quantum-chemistry code TURBOMOLE[142]. The first step in this method is the description of the electronic structure of the junctions within DFT. In all the calculations described here we have used the BP86 exchange-correlation functional[143] and the Gaussian basis set def-SVP[144]. The total energies were converged to a precision of better than 10^{-6} atomic units, and structure optimizations were carried out until the maximum norm of the Cartesian gradient fell below 10^{-4} atomic units.

The final step in our method is the transformation of the information on the electronic structure of the junctions obtained with DFT into the elastic transmission of the junctions. This is done with the help of non-equilibrium Green's function techniques, as explained in detail in the past work[135]. In what follows, we shall separately address the analysis of gold atomic junctions and single-molecule junctions.

4.4.3.1 *Gold Atomic Junctions*

The analysis of the transmission curves of gold atomic junctions was already reported [145]. Thus, we just present a brief description of the transmission calculations and focus on the consequences for the local heating in these junctions. To study a Au atomic junction we first define an ideal geometry like the example shown in Figure 4.8a, which corresponds to the junction shown in the inset-i of Figure 4.4b. It consists of two pyramids grown along the $\langle 100 \rangle$ direction of an fcc lattice and facing each other such that they form an atom dimer in the narrowest part of the junction. We relax the positions of the atoms located both in the dimer and in the two neighboring layers (consisting of

four atoms each). The other atoms in the junction are kept fixed, and the lattice constant is set to 0.408 nm, the experimental value for gold.

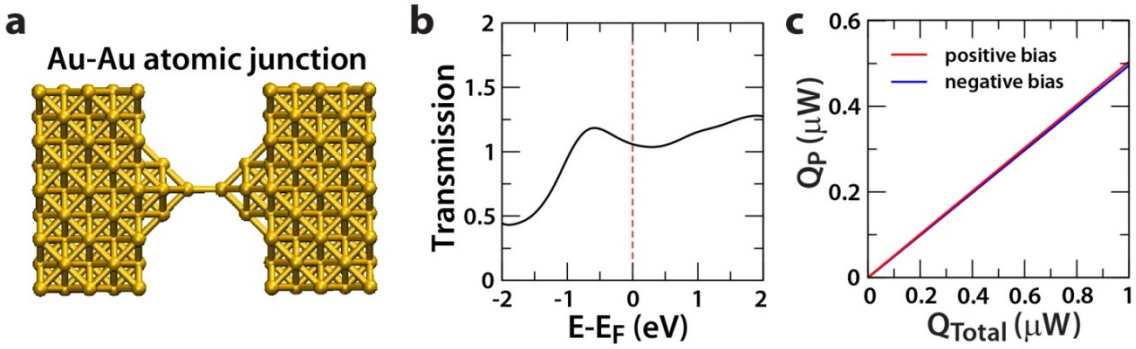

*Figure 4.8 Ab initio calculations of the transmission and heat dissipation in gold atomic junctions. (**a**) The model of a Au atomic junction with a conductance close to $1G_0$. (**b**) The transmission (as computed from our DFT approach) as a function of the energy for the atomic junction. (**c**) The computed results for the heating in the probe electrode for positive and negative bias voltages as a function of the total power dissipated in the junction.*

We present in Figure 4.8b the zero-bias transmission as a function of the energy for the junction shown in Figure 4.8a. The corresponding results for the heating in the probe electrode as a function of the total power dissipated in the junction are shown in Figure 4.8c (for positive and negative bias). The heating has been calculated using Eq. (4.3) and the zero-bias transmission function, *i.e.* we have assumed that the transmission is independent of the bias, which is justified in view of the linearity of the experimental I-V curves (see inset-ii of Figure 4.4b). This assumption has also been used, together with the Landauer formula, to compute the total power. As one can see, the power dissipated in the probe electrode is symmetric with respect to the inversion of the bias, which is in perfect agreement with our experimental results (see Figure 4.4a). This is a consequence

of the weak energy dependence of the transmission in the transport window and of the negligible slope at the Fermi energy (*i.e.* the thermopower vanishes).

4.4.3.2 ***Single-Molecule Junctions***

We now describe our DFT-based calculations of the transmission and heating in Au-1,4-benzenediisonitrile-Au (Au-BDNC-Au) and Au-1,4-benzenediamine-Au (Au-BDA-Au) junctions. In this case, we first relax the isolated molecules. Then, we construct the single-molecule junctions by placing the relaxed molecules in between two gold clusters with 20 (or 19) atoms. Subsequently, we perform a new geometry optimization by relaxing the positions of all the atoms in the molecule as well as the four (or three) outermost gold atoms on each side, while the other gold atoms are kept frozen. Afterwards, the size of the gold cluster is increased to about 63 atoms on each side in order to describe correctly both the metal-molecule charge transfer and the energy level alignment. Finally, the central region, consisting of the molecule and one or two Au layers is coupled to ideal gold surfaces, which serve as infinite electrodes and are treated consistently with the same functional and basis set within DFT[135].

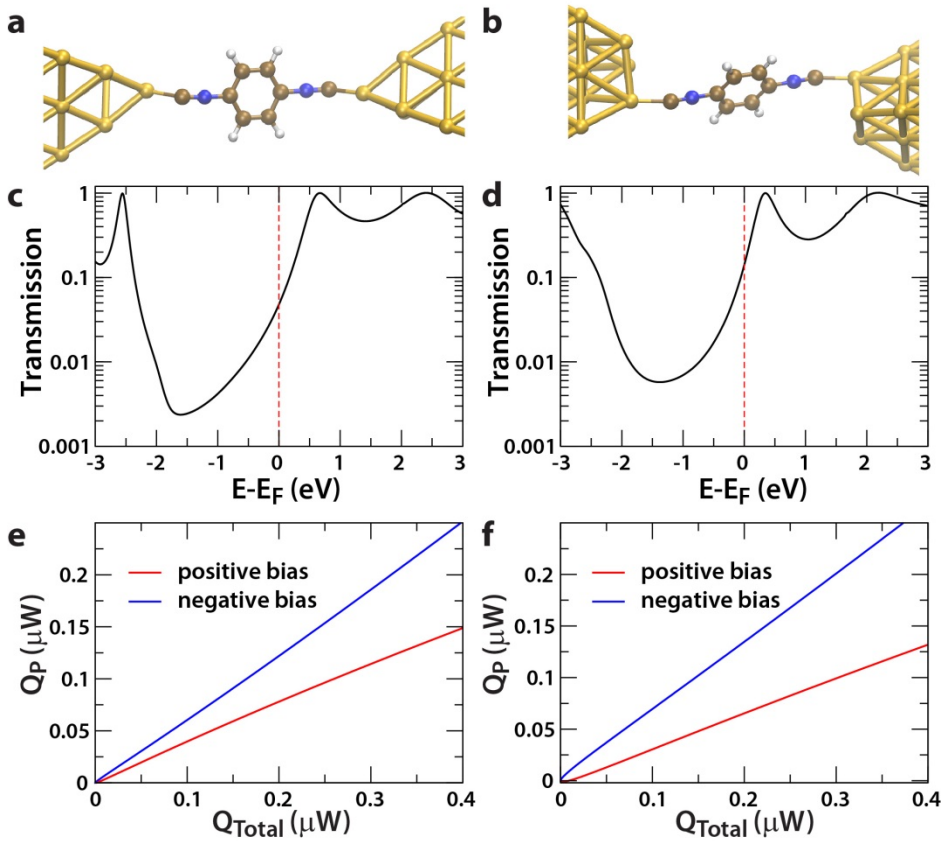

*Figure 4.9 Ab initio results for the transmission and local heat dissipation in Au-BDNC-Au junctions. **(a-b)** The two atop Au-BDNC-Au junction geometries investigated here. **(c-d)** The computed zero-bias transmission as a function of the energy for the two geometries. For clarity, the position of the Fermi level has been indicated with vertical lines. **(e-f)** The corresponding results for the heating in the probe electrode, for positive and negative biases, as a function of the total power dissipated in the Au-BDNC-Au junction.*

Au-BDNC-Au Junctions: First of all, we have studied the most probable geometries of the Au-BDNC-Au junctions and we have found that the isonitrile group binds preferentially to low-coordinated gold atoms in atop positions. This is in agreement with previous studies of adsorption of isocyanides on gold surfaces[146]. Two representative examples of the atop geometries found in our analysis are shown in the Figure 4.9a and b.

Notice that in both cases the C atom is directly bound to a single Au atom and the main difference between the two geometries lies in the shape of the electrodes. The results for the zero-bias transmission as a function of energy for these two junctions are shown in Figure 4.9c and d. In both cases the conductance, determined by the transmission at the Fermi energy, is dominated by the LUMO. This is in qualitative agreement with previous results[51,147]. The conductance values in these two examples are $0.048G_0$ (left junction) and $0.14G_0$ (right junction). These values are clearly higher than the preferential value of $0.002G_0$ found in our experiments. We attribute this discrepancy to the intrinsic deficiencies of the existent DFT functionals that tend to underestimate the HOMO-LUMO gap.

On the other hand, making use of Eq. (4.3), we have also computed the power dissipated in the probe electrode for these two junctions as a function of the total power dissipated in the junction and the results for positive and negative bias are shown in Figure 4.9e and f. In these calculations we have approximated the transmission curves by the zero-bias functions shown in Figure 4.9c and d. This approximation is justified by the fact that the highest bias explored in our experiments is still quite low as compared to the HOMO-LUMO of the molecules. Moreover, in our relatively weakly-coupled and symmetric molecular junctions the voltage is expected to drop mainly at the metal-molecule interfaces. This means that the relevant orbitals in the molecule are not significantly shifted by the bias and thus, the transmission is expected not to vary appreciably with the voltage, see for instance Ref. [141]. As one can see in Figure 4.9e and f, the heating in the probe is clearly asymmetric and it is larger for negative voltages as a result of the positive slope of the transmission functions at the Fermi energy, which gives rise to a

negative Seebeck coefficient. We note that although the DFT calculations overestimate the linear conductance, they correctly reproduce the observed relation between the power dissipated in the probe and the total power (see Figure 4.2b). In particular, the heating asymmetry is well described because it is determined by the slope of the transmission at the Fermi energy which is less prone to the details like the junction geometry[53]. Indeed, it is important to note that the relations between Q_P and Q_{Total} is very similar for both geometries, which illustrates the insensitivity of this relation to junction details.

In order to understand this insensitivity to contact details in simple terms, we have performed additional numerical and analytical calculations using the so-called *single-level model*, also referred to as resonant tunneling model[15]. In this model one assumes that the transport is dominated by a single molecular orbital, which is basically what occurs in our molecular junctions. The corresponding transmission is a Lorentzian function with two parameters: the level position and the strength of the metal-molecule coupling (or level broadening). Our calculations show that in off-resonant situations (as is the case in our molecular junctions) the relation between Q_P and Q_{Total} does not depend significantly on the exact level position, but only on the level broadening. This broadening, on the other hand, is robust since it depends solely on the symmetry of the dominant molecular transport state that couples to a rather energy-independent density of states of the gold electrodes. Thus, these toy-model calculations (nots hown here to avoid redundancy) suggest that DFT-based approaches should be able to correctly predict the relationship between Q_P and Q_{Total}. More detailed explanation can be found in our recent work [148]. Indeed, this is precisely what we find in for the molecular junctions studied in this work

Au-BDA-Au Junctions: We have explored different binding geometries for the benzenediamine molecule between gold electrodes and found that the amine group only binds to undercoordinated Au sites, as it has been reported in the literature[136,149,150]. We show two examples of atop geometries for the Au-BDA-Au junctions in the Figure 4.10a and b. The corresponding results for the zero-bias transmission as a function of energy are shown in Figure 4.10c and d. These two junctions have conductance values equal to $0.020G_0$ (left junction) and $0.011G_0$ (right junction), which are slightly higher than the preferential value of $0.005G_0$ found experimentally. Again, this overestimation of the conductance can be attributed to the correlations effects that are not properly described within the DFT framework with conventional exchange-correlation functionals. Such functionals tend to underestimate the HOMO-LUMO gap and therefore they overestimate the conductance[149,151]. On the other hand, the transmission curves indicate that the HOMO of the molecule dominates charge transport in these junctions, which results in a negative slope at the Fermi energy. This slope is reflected (see Figure 4.10e and f) in the form of larger heat dissipation for positive bias in the probe electrode, contrary to the case of Au-BDNC-Au junctions. Notice that in this case the magnitude of the heating asymmetry is smaller than in Au-BDNC-Au junctions due to the smaller slope of the transmission at the Fermi energy and, in general, to the smaller electron-hole asymmetry around the Fermi energy. Finally, we emphasize that the magnitude of the computed heating asymmetry is very similar for both geometries and is in good agreement with the experimental findings (see Figure 4.3b).

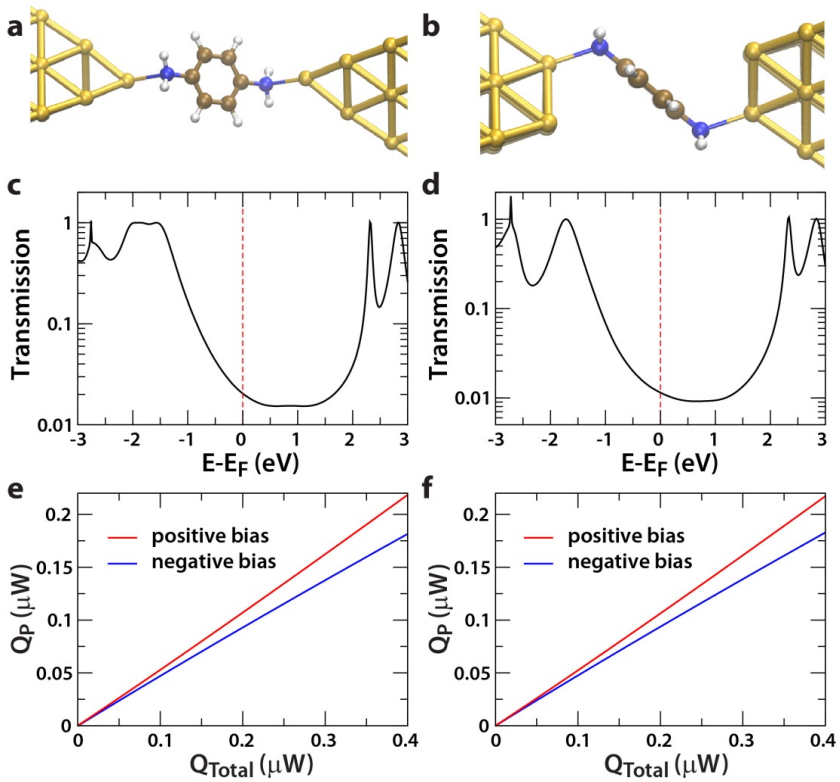

*Figure 4.10 Ab initio results for the transmission and heat dissipation in Au-BDA-Au junctions. **(a-b)** The two atop Au-BDA-Au junction geometries investigated here. **(c-d)** The computed zero-bias transmission as a function of the energy for the two geometries. For clarity, the position of the Fermi level has been indicated with vertical lines. **(e-f)** The corresponding results for the heating in the probe electrode, for positive and negative biases, as a function of the total power dissipated in the Au-BDA-Au junction.*

4.4.4 Characterization of Thermal Resistance, Thermal Time Constant, and Seebeck Coefficients of the NTISTP

In this section we provide a description of our measurements of the thermal resistance and thermal time constant of the NTISTP along with a description of the characterization of the Seebeck coefficient of the integrated nanoscale thermocouple.

4.4.4.1 *Thermal Resistance of the NTISTP*

The thermal resistance of the probe can be experimentally obtained from the data shown in Figure 4.4a. This is possible due to the fact that for Au-Au atomic junctions the heat dissipation in the NTISTP and in the substrate is identical (see Section 4.4.2 for details). This in turn implies that $Q_{P,\ Avg}(V) + Q_{S,\ Avg}(V) = 2Q_{P,\ Avg}(V) = Q_{Total,\ Avg}(V)$. Since $Q_{P,\ Avg}(V) = \Delta T_{TC,\ Avg}(V) / R_P$ one can directly estimate R_P by using the data shown in Figure 4.4a in conjunction with the above equations. By performing this analysis, we determined R_P to be 72800 ± 500 K/W. The uncertainty in R_P is related to the uncertainty in the measured temperature rise of the thermocouple (~0.1 mK for each of the data points shown in Figure 4.4a, more details in Section 4.4.6).

4.4.4.2 *Time Constant of the NTISTP*

To measure the thermal time constant of the NTISTP we followed an approach developed in the past[152]. In this approach, a sinusoidal current at a frequency f was passed through the integrated thermocouple, while the NTISTP was not in contact with the substrate (Figure 4.11a). This resulted in Joule heating in the thermocouple junction at a frequency $2f$, which in turn resulted in temperature oscillations of the integrated thermocouple at $2f$ that were recorded by monitoring the voltage output of the thermocouple using a lock-in amplifier. The amplitudes of the normalized temperature oscillations are shown in Figure 4.11b as a function of the heating frequency ($2f$). The cut-off frequency (f_c), defined as the frequency at which the amplitude is attenuated to $1/\sqrt{2}$, is found to be ~20 kHz clearly showing that the integrated thermocouple has a very fast response time. Specifically, the thermal time constant ($\tau = 1/2\pi f_c$) was estimated

to be ~10 μs.

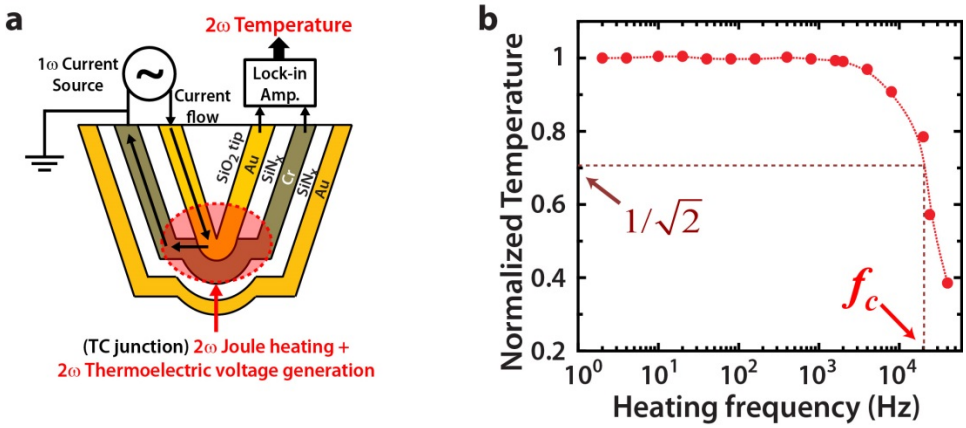

*Figure 4.11 Experimentally estimating the thermal time of the NTISTP. **(a)** Schematic diagram of a setup where a sinusoidal electrical current at a frequency f is supplied through the TC of the NTISTP (when it is not in contact with a substrate). **(b)** The normalized temperature (amplitude of temperature oscillation divided by the amplitude at the lowest frequency), obtained from the measured thermoelectric voltage at 2f across the TC, is shown as a function of the heating frequency indicating a cut-off frequency of ~20 kHz.*

4.4.4.3 *Seebeck Coefficient of the NTISTP*

The approach taken by us to measure the Seebeck coefficient of the nanoscale thermocouples was described in our past work[140]. Briefly, the NTISTP was placed in mechanical contact with a heated substrate. Excellent thermal contact was achieved between the substrate and the tip of the NTISTP by using a thermally conducting epoxy. Further, two thermocouples were attached to the thick Si cantilever of NTISTP and the substrate to monitor the temperature of the cantilever (T_C) and the substrate (T_S). In order to quantify the Seebeck coefficient (S_{TC}) of the Au-Cr thermocouple the temperature of the substrate was increased in known steps while measuring the temperature of the

cantilever. The thermoelectric voltage across the Au-Cr junctions (V_{TE}) was simultaneously recorded. Given the excellent thermal contact between the tip and the substrate, the tip temperature (T_{tip}) can be assumed to be the same as the substrate temperature ($T_S = T_{tip}$). Therefore, the measured thermoelectric voltage (V_{TE}) can be directly related to the Seebeck coefficient of the junction by $V_{TE} = S_{TC} \times (T_S - T_C)$. From these measurements, the S_{TC} was estimated to be 16.3 ± 0.2 μV/K.

4.4.5 Estimation of a Lower Bound for the Thermal Resistance (R_J) of Atomic and Molecular Junctions

We noted that the thermal resistance at the tip-substrate junction is at least 10^7 K/W for all the AMJs studied in this work. Here, we provide a detailed justification for this assertion. The thermal resistance of atomic and molecular junctions has not been experimentally studied. However, computational studies of heat transport in single-molecule junctions[72], and experimental studies of thermal transport in monolayers[106,107] indicate that the thermal resistance of molecular junctions is indeed very large. Specifically, Segal *et al.*[72] reported that the thermal resistance of Au-alkanedithiol-Au junctions is in the range of 10^{10} - 10^{11} K/W for alkane chain lengths ranging from 4-20 carbon atoms. Further, recent experimental studies[107] on monolayers of alkane chains trapped between a Au thin film and a quartz substrate suggest that the thermal resistance per molecule is indeed in the range predicted by Segal *et al*. In addition to this, computations by Sergueev *et al*.[153] on Al-biphenylydithiol-Al junctions also suggests that the thermal resistance is ~5×10^{11} K/W at room temperature. This suggests that the phononic contribution to the thermal resistance of all single molecule junctions and (by extension) atomic chains is indeed much larger than 10^7 K/W

(the lower bound assumed in the manuscript for the thermal resistance of atomic and molecular junctions). ***One can also estimate the electronic contribution to the thermal resistance of Au atomic junctions which have an electrical conductance of ~1G_0 by using the Wiedemann-Franz law*[154].** Such a calculation suggests that the electronic contribution to thermal resistance is ~2×10^9 K/W at room temperature—a value much larger than 10^7 K/W. We also note that recent measurements of thermal resistance of a nanoscale point contact between solids[155] suggests that the point contact thermal resistance between an InAs nanowire and a SiN_x membrane is ~6×10^8 K/W, showing that the phonon thermal resistance of point contacts is indeed much larger than 10^7 K/W.

Recent studies of near-field radiative heat transport between Au-coated surfaces suggest a possible approach for estimating a lower limit on the thermal resistance due to near-field radiative phenomena. Specifically, Shen *et al.*[156] studied thermal transport between a micro-scale (~50 μm diameter) Au coated silica sphere and a Au substrate and found that the thermal resistance is ~10^9 K/W for gap sizes of ~10 nm. Since the diameter of the NTISTPs used in this study is much smaller (~100 nm), the effective area for near field heat transfer is much smaller. Therefore, a simple proximity theorem[156] based estimation would suggest that the expected thermal resistance to heat flow due to near-field radiation between the NTISTP and substrate is at least 10^9 K/W. Taken together, all the estimates presented above suggest that our assumption that R_J is at least 10^7 K/W is very conservative and well justified for all the AMJs studied in this work.

4.4.6 Analysis of the Modulation Scheme and Quantification of the Uncertainty in the Measurements

In order to study local heating in molecular junctions one can in principle apply a DC voltage bias and measure the resultant temperature change as reported by the thermoelectric voltage across the thermocouple ($\Delta V_{TC}(t)$) of the NTISTP. However, such a direct implementation has a poor temperature resolution as the thermoelectric voltage signal of interest is contaminated by electronic noise $V_N(t)$, which can be stochastic or periodic (e.g. 60 Hz noise). In order to improve the temperature resolution it is necessary to effectively reject the electric noise by reducing the bandwidth of the measurement. One potential approach to reducing the bandwidth of a measurement is to apply a sinusoidal voltage (offset by an appropriate DC value) across the molecular junction and employ a regular lock-in amplifier for detecting thermoelectric voltage oscillations from the thermocouple at the second harmonic. However, implementation of such a scheme is rendered difficult by the inherently non-linear *I-V* characteristics of molecular junctions: such non-linearities result in temperature oscillations at both the second harmonic as well as higher harmonics.

A second approach is to apply a DC voltage bias and measure the thermoelectric voltage across the junction for a sufficiently long time to enable time-averaging. However, such an approach requires measurements for very long times to eliminate the effect of the low frequency noise (described in more detail below). In order to successfully improve the resolution of our measurements we employed a modulation scheme where a three level voltage bias was applied across the junctions (Figure 4.5), while monitoring the thermoelectric voltage signal from the nanoscale thermocouple integrated into the probe.

The recorded thermoelectric voltage is subsequently analyzed to extract the temperature rise in the thermocouple corresponding to a positive and negative bias (explained in detail below). In order to highlight the utility of the modulation scheme, in Appendix 1 we analyze the noise reduction achieved in both the modulation scheme and the simple time-averaging scheme described above.

4.4.6.1 *Unprocessed and Processed Data Obtained in the Experiments*

The discussion given in Appendix 1 provides simple expressions (eq. (A1.10) and (A1.15)) for estimating the time averaged temperature rise of the thermocouple from the measured data. However, such an approach does not enable easy visualization of the temperature asymmetry. In this section we address the following question: can the asymmetric temperature response of the thermocouple be visually accessed from the raw data, at least for high power dissipations, where the temperature rises corresponding to positive and negative biases $\Delta T_{TC,Avg}(+V_M)$ and $\Delta T_{TC,Avg}(-V_M)$ respectively, as well as their differences are relatively large?

In order to answer this question, we begin by noting that the largest temperature rise (corresponding to molecular junctions) reported in the manuscript is ~15 mK. This implies that the corresponding modulated thermoelectric voltage output is $S_{TC} \times$ 15 mK = 245 nV, where S_{TC} = 16.3 ± 0.2 μV/K. Given the power spectral density of the electronic noise from the thermocouple (Figure 4.15, see Section 4.4.6.2 for details) the RMS value of noise in a 1 kHz bandwidth can be estimated to be a few microvolts (i.e. the RMS value of temperature noise is a few hundred millikelvin). We note that all the thermoelectric voltage measurements were performed at a sampling rate of 2 kHz after

low pass filtering the signal at a cut-off frequency of 1 kHz to prevent aliasing of higher frequency noise into the signal (hence the choice of the 1 kHz bandwidth above). Given that the RMS value of voltage noise is an order of magnitude larger than the temperature signal it is to be expected that it would not be possible to visually see the modulated temperature signal from a time trace of the thermoelectric voltage obtained in one period of the measurement (1/12.25 s).

In order to demonstrate the assertions made above we show one-period of a three-level voltage signal corresponding to a modulation amplitude of 1.27 V in Figure 4.12a. This represents the voltage bias applied across Au-BDNC-Au junctions in measurements with the highest power dissipation ($Q_{Total,\ Avg}$ = 0.35 μW). A representative electrical current measured in such an experiments is shown in Figure 4.12b. In Figure 4.12c, we show a measured thermoelectric voltage signal (converted to temperature from the known S_{TC}), which was offset to ensure that the mean value of the voltage corresponding to the region where no bias is applied (region shaded in green) is zero: this offset arises from the small temperature difference that exists between the NTISTP and the ambient. As expected, it is not possible to visually delineate the temperature signal corresponding to the applied biases from the data shown in Figure 4.12c. However, it is clear that if the noise is random it would be possible to dramatically increase the signal-to-noise ratio by averaging all the temperature signals obtained in individual experiments such as those shown in Figure 4.12c. In order to demonstrate this, we show in Figure 4.12d an averaged temperature signal obtained from 122 individual experiments (~10 seconds of data). The averaging is performed by first superimposing the measured temperature signals from a series of experiments such that the start and end points align. Subsequently, the voltages

corresponding to each point on the *x*-axis are averaged to obtain the desired curve. It can be clearly seen that the noise on the temperature signal decreases upon averaging.

In Figure 4.12e we present the averaged temperature data obtained from 100 seconds of data (1225 individual experiments). It can be clearly seen that the noise is significantly attenuated and the temperature signal corresponding to positive and negative biases is different. Finally, in Figure 4.12f we present the temperature data obtained from 500 seconds of data (6125 individual experiments). From this data, it can be clearly seen that the temperature rise corresponding to positive and negative biases is different and is ~15 mK for a positive bias and ~10 mK corresponding to a negative bias. More accurate numbers can be obtained by averaging the temperature rise corresponding to positive and negative biases (see discussion in the last paragraph below). Such an analysis suggests that the average temperature rise corresponding to a positive bias is 10.3 mK (represented by a blue long-dashed line in Figure 4.12f) and that corresponding to a negative bias is 15.2 mK (represented by a green short-dashed line in Figure 4.12f). Further, the standard deviations corresponding to these averages are 0.6 mK for both positive and negative biases. These values are in excellent agreement with those reported in Figure 4.2b.

In Figure 4.13 and Figure 4.14, we present otherwise identical data, corresponding to the highest average power dissipation (0.35 μW), obtained in the case of Au-BDA-Au and Au-Au junctions, respectively. In Figure 4.13 it can be immediately seen that the temperature rise corresponding to a positive bias (+0.82 V) is larger than the temperature rise corresponding to a negative bias (-0.82 V). In contrast, for the Au-Au data shown in Figure 4.14, the temperature rise corresponding to both positive (+0.067 V) and negative (-0.067 V) biases is identical within experimental uncertainty. Further, the temperature

rise corresponding to positive and negative biases obtained by averaging the data shown in Figure 4.13 & Figure 4.14 as well as the standard deviations corresponding to the averages are in excellent agreement with those reported in Figure 4.3b & Figure 4.4a.

Before we conclude, we would like to emphasize an important point. It can be seen from the data shown in Figure 4.12f, Figure 4.13f, & Figure 4.14f that the temperature change corresponding to the positive and the negative biases is relatively constant at all periods of time—this is a reflection of the extremely fast thermal time constant of the NTISTP (estimated to be ~10 μs in Section 4.4.4.2). This suggests that further averaging can be performed on the data to accomplish greater noise reduction. For example, it is possible to average the 22 data points from the 2 ms – 24 ms (two data points at the beginning and at the end of the data can be excluded to roll-off effects from the low pass filter) to obtain a more accurate estimate of the temperature response corresponding to a positive bias. Similarly, it is possible to average 22 data points from 46 ms – 78 ms to get a more accurate estimate of the temperature response due to a negative bias. This is very similar to what is accomplished by Eq. (A1.10) and (A1.15), enabling us to determine the temperature changes in the thermocouple with excellent resolution (<0.3 mK)—this is key to extracting the temperature change of the thermocouple in measurements at the lowest power dissipation (0.07 μW). In the next sections, we describe a series of measurements that were performed to unambiguously determine the noise floor of our measurement scheme.

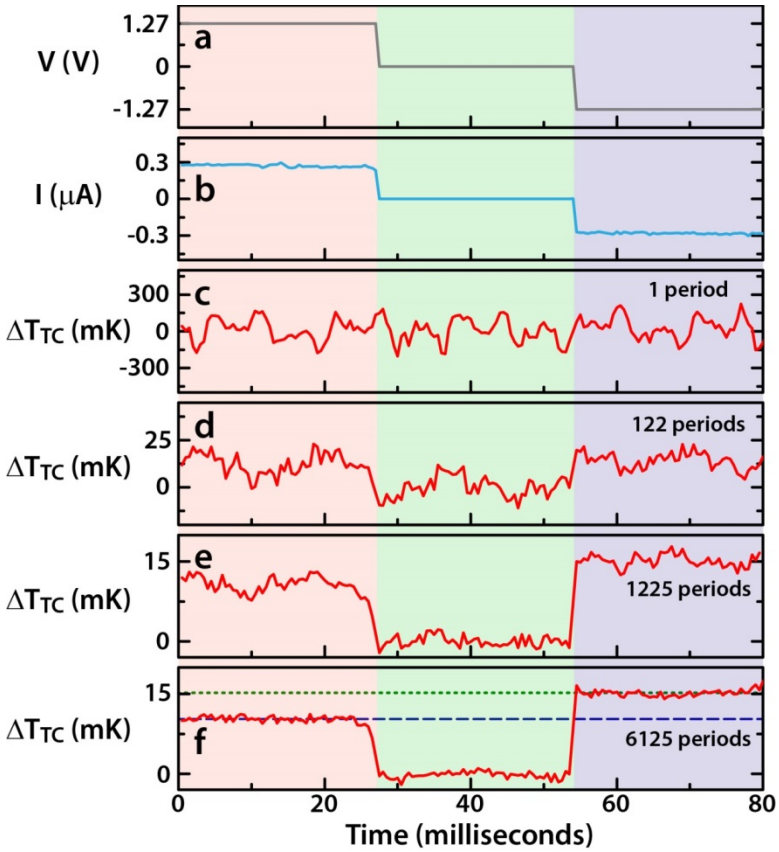

*Figure 4.12 Raw and averaged data obtained in heat dissipation studies of Au-BDNC-Au junctions corresponding to a $Q_{Total,\ Avg}$ of 0.35 μW. (**a**) The three level voltage signal with an amplitude of 1.27 V. (**b**) The resultant current and (**c**) The temperature signal from the thermocouple (voltage output of the thermocouple divided by S_{TC}) in one period. The temperature signal obtained by averaging 10 s of data (~122 periods), 100 s of data (1225 periods), and 500 s of data (6125 periods) are shown in (**d**), (**e**), and (**f**), respectively. It can be seen that the average temperature rise is larger for a negative bias than a positive bias. From (**f**) the average temperature rise corresponding to a positive bias (blue long-dashed line) is estimated to be 10.3 mK and that corresponding to a negative bias (green short-dashed line) is estimated to be 15.2 mK. Further, the standard deviations corresponding to these averages are 0.6 mK for both positive and negative biases. These values are in excellent agreement with those reported in Figure 4.2b.*

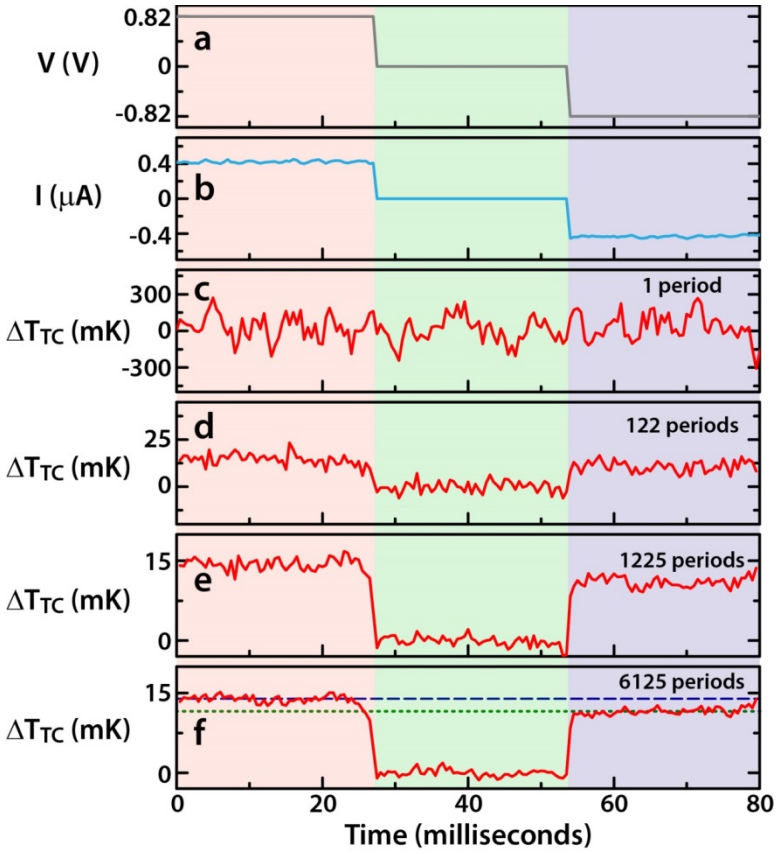

*Figure 4.13 Same as Figure 4.12 but for Au-BDA-Au junctions. From (**f**) the average temperature rise corresponding to a positive bias is 13.9 mK (blue long-dashed line) and that corresponding to a negative bias is 11.6 mK (green short-dashed line). Further, the standard deviations corresponding to these averages are 0.6 mK for both positive and negative biases. These values are in excellent agreement with those reported in Figure 4.3b.*

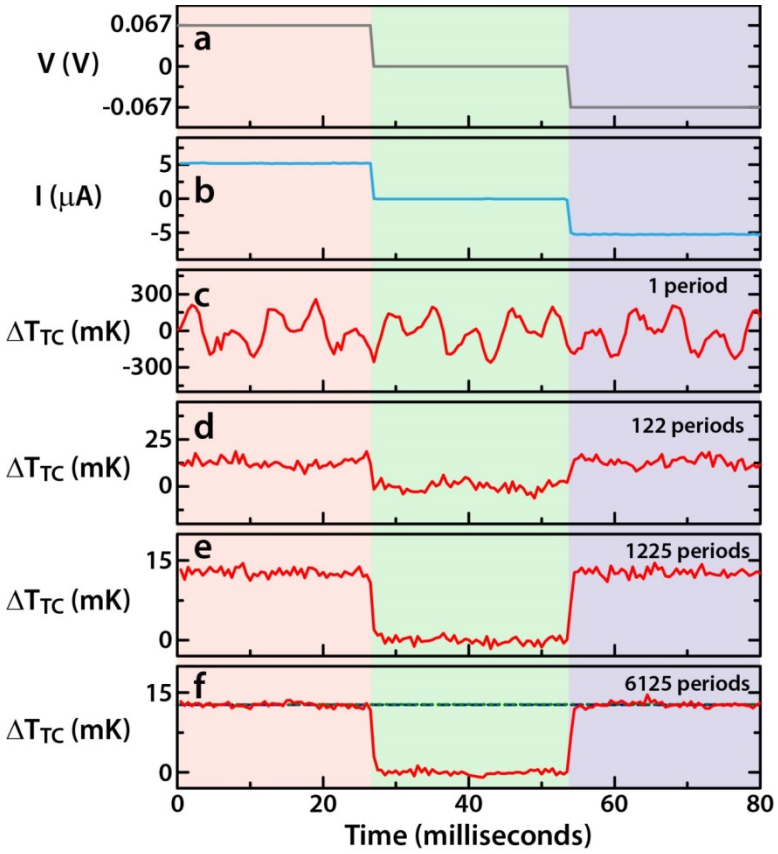

Figure 4.14 Same as Figure 4.12 but for Au-Au atomic junctions. From ***(f)*** *the average temperature rise corresponding to both positive and negative biases is 12.7 mK (the blue and green dashed lines representing the means overlap). Further, the standard deviations corresponding to these averages are 0.4 mK for both positive and negative biases. These values are identical to that reported in Figure 4.4a.*

4.4.6.2 *Experimentally Measured Power Spectral Density of Voltage Noise of the Thermocouple and Estimate of $\Delta T_{Noise,\ RMS}$*

In order to estimate the temperature noise using Eq. (A1.14) it is necessary to measure the power spectral density (PSD) of the thermoelectric voltage noise of the integrated thermocouple. Figure 4.15 shows the measured PSD of the thermocouple, obtained using a commercially available spectrum analyzer (SR760, Stanford Research System). The

measured PSD is found to be large at low frequencies, showing a $1/f$ behavior. Using Eq. (A1.14) in conjunction with the measured PSD we estimate that $\Delta T_{Noise,\ RMS}$ associated with the nanoscale thermocouple is ~50 μK. In performing these estimates, the values of $2\tilde{T}$ and Δt were chosen to be 500 seconds and 27.2 ms = 1/(3×12.25 Hz), respectively, so as to correspond well to the values of $2\tilde{T}$ and Δt used in the experiments.

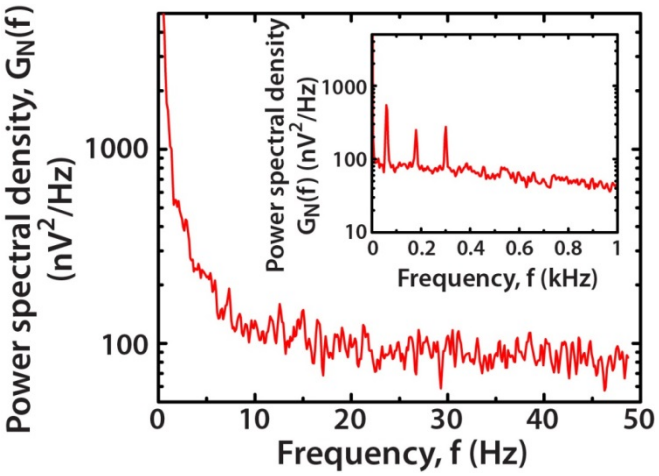

Figure 4.15 The measured one-sided power spectral density (PSD) of the thermocouple voltage noise (0 – 50 Hz). The inset shows the measured PSD in a larger range frequencies (0 – 1 kHz).

In order to check the accuracy of the estimate we analyzed the RMS value of the measured noise using a second approach. Specifically, we recorded the noise voltage from the thermocouple for a period of 500 seconds, in a bandwidth of 1 kHz, and computed $\overline{V}_{noise,\ M}$ (the voltage noise in the modulation scheme) using Eq. (A1.11). This was repeated ten times to obtain $\overline{V}_{noise,\ M}(i),\ i = 1{:}10$ to compute the RMS values of the

voltage noise $\left\langle \bar{V}^2_{noise,\,M} \right\rangle^{1/2} = \left[\sum_{i=1}^{10} \left(\bar{V}_{noise,\,M}(i) \right)^2 \Big/ 10 \right]^{1/2}$ and the corresponding temperature noise which were found to be 0.5 nV and ~30 μK respectively. This value is in reasonable agreement with the estimated RMS temperature resolution from the frequency domain analysis and confirms the validity of Eq. (A1.14). Taken together, these estimates suggest that the ***uncertainty in the measured temperature due to electronic noise is ~50 μK***.

4.4.6.3 *Quantification of the Effect of Capacitive Coupling*

In addition to the electronic noise described above the capacitive coupling between the thermocouple leads and the substrate also results in a spurious signal. The effect of capacitive coupling is to generate a noise signal that is indistinguishable from the thermoelectric voltage signal of the thermocouple. Figure 4.16a schematically shows a circuit diagram that represents the capacitive coupling between the substrate and the NTISTP by three capacitors: the capacitor C_1 represents the capacitive coupling between the substrate and the outer Au electrode, C_2 represents the capacitive coupling between the outer Au electrode and the Cr electrode of the thermocouple, and C_3 represents the capacitive coupling between the Cr and inner Au electrode. The resistors R_1, R_2, and R_3 shown in Figure 4.16a represent the electrical resistances in the leads of the NTISTP. The data provided below are well accounted for by this simple model.

In order to quantify the effect of capacitive coupling, we performed a series of experiments in which the tip of the NTISTP was placed in close proximity of the substrate (~5 nm), while a modulated ***sinusoidal*** signal was supplied to the substrate as shown in Figure 4.16b. Here, a sinusoidal signal is chosen instead of the three level

modulation scheme due to the simplicity of analyzing sinusoidal signals. In the first set of experiments the frequency of modulation was chosen to be 12.25 Hz and the sinusoidal voltage output from the thermocouple was monitored using a lock-in amplifier (SR 830) as the amplitude of the input sinusoidal signal was systematically varied (0 V – 7.5 V). Figure 4.16c shows the results obtained in these experiments where the voltage output is seen to increase proportionally with the voltage input. We note that in these experiments the resistance between the tip and the substrate is very large (>1 GΩ), therefore, the electrical current through the tip-substrate junction is negligible resulting in insignificant amount of Joule heating. Hence, the measured voltage output is primarily due to capacitive coupling and electronic noise.

In addition to these experiments, we studied the frequency dependence of capacitive coupling. Specifically, we performed an experiment where the amplitude of the sinusoidal signal supplied to the substrate was held constant at 1.5 V while the frequency of the sinusoidal signal was systematically varied. The voltage output measured across the thermocouple junction in these experiments is shown in Figure 4.16d. It can be seen that the voltage output increases quadratically with frequency. This result may seem surprising at first sight as one would naively expect a linear dependence on frequency when the coupling is capacitive[157]. The quadratic dependence can be understood by noting that in our set up there are multiple levels of capacitive coupling: first the substrate is coupled to the outer electrode of the NTISTP (via C_1, see Figure 4.16a) and the outer electrode is subsequently capacitively coupled to the inner Cr electrode via capacitor C_2 and finally there is resistive (through the contact at the apex) and capacitive coupling between the Cr and inner Au electrode. A detailed analysis of this circuit configuration

shows that the voltage output across the thermocouple should indeed be quadratically dependent on the frequency.

Finally, we performed experiments on ~5 nm NTISTP-substrate gaps using a three level modulation scheme (Figure 4.16e). These experiments aim to quantify the dependence of measured (capacitively coupled) voltage noise on both the voltage bias and the time period of measurements. First, to understand the effect of the total time of measurement $2\tilde{T}$ (see Figure 4.5a) on the voltage noise due to capacitive coupling we applied a three-level modulation signal with V_M = 1.5 V for 500 seconds. This was repeated 10 times while recording the voltage output from the thermocouple. The data obtained in each of these experiments was analyzed to compute $\overline{V}_{noise,\ M}(+V_M / -V_M)$ and $\left\langle \overline{V}^2_{noise,\ M}(+V_M / -V_M) \right\rangle^{1/2}$ from which the apparent RMS temperature due to capacitive coupling $(\Delta T_{App,\ Capacitive,\ RMS}(+V_M / -V_M))$ was obtained using $\left\langle \overline{V}^2_{noise,\ M}(+V_M / -V_M) \right\rangle^{1/2} = S_{TC} \times \Delta T_{App,\ Capacitive,\ RMS}(+V_M / -V_M)$. This was repeated for a range of modulation voltages and time periods to obtain the data shown in Figure 4.16f where $\Delta T_{App,\ Capacitive,\ RMS}(+V_M)$ is shown for various time periods of measurements and bias voltages. We note that the RMS values for negative biases are identical and not shown. It can be seen that the RMS values decrease as the total time of the measurement increases but eventually becomes constant for measurements longer than ~200 seconds (as expected from Eq. (A1.14)). It can be seen that the largest RMS value occurs for an amplitude of 1.5 V and is ~0.3 mK.

In the inset of Figure 4.16f, we plot $\Delta T_{App,\ Capacitive,\ RMS}$ obtained from experiments where the modulation voltages were systematically varied while keeping the frequency of modulation and the total time of measurement fixed at 12.25 Hz and 500 seconds respectively. It can be seen from the figure that the RMS noise voltages increase linearly as the applied bias voltage is increased. Further, it can be seen that for a modulation voltage of ~1.5 V (the largest bias applied in the experiments) the RMS temperature noise is ~0.3 mK. Therefore, it is clear that the largest uncertainty introduced by capacitive coupling is ~0.3 mK and occurs at the largest applied bias. We also note that when V_M = 0 V the measured RMS noise in the temperature is ~30 μK and is consistent with the analysis provided in the earlier section. Taken together these experiments suggest that capacitive coupling does not contribute significantly if a sufficiently low modulation frequency is employed. However, if a higher modulation frequency is selected the effect of capacitive coupling can become substantial.

The data shown in the inset of Figure 4.16f along with the discussion provided in Section 4.4.6.2 unambiguously proves that the noise equivalent temperature for the chosen modulation scheme is ***~0.3 mK at the highest voltage bias (1.5 V), ~0.1 mK at the lowest bias (0.45 V) employed in studying heat dissipation in molecular junctions, and ~50 - 100 μK at the lowest biases (30 mV) employed for probing heat dissipation in Au-Au junctions***.

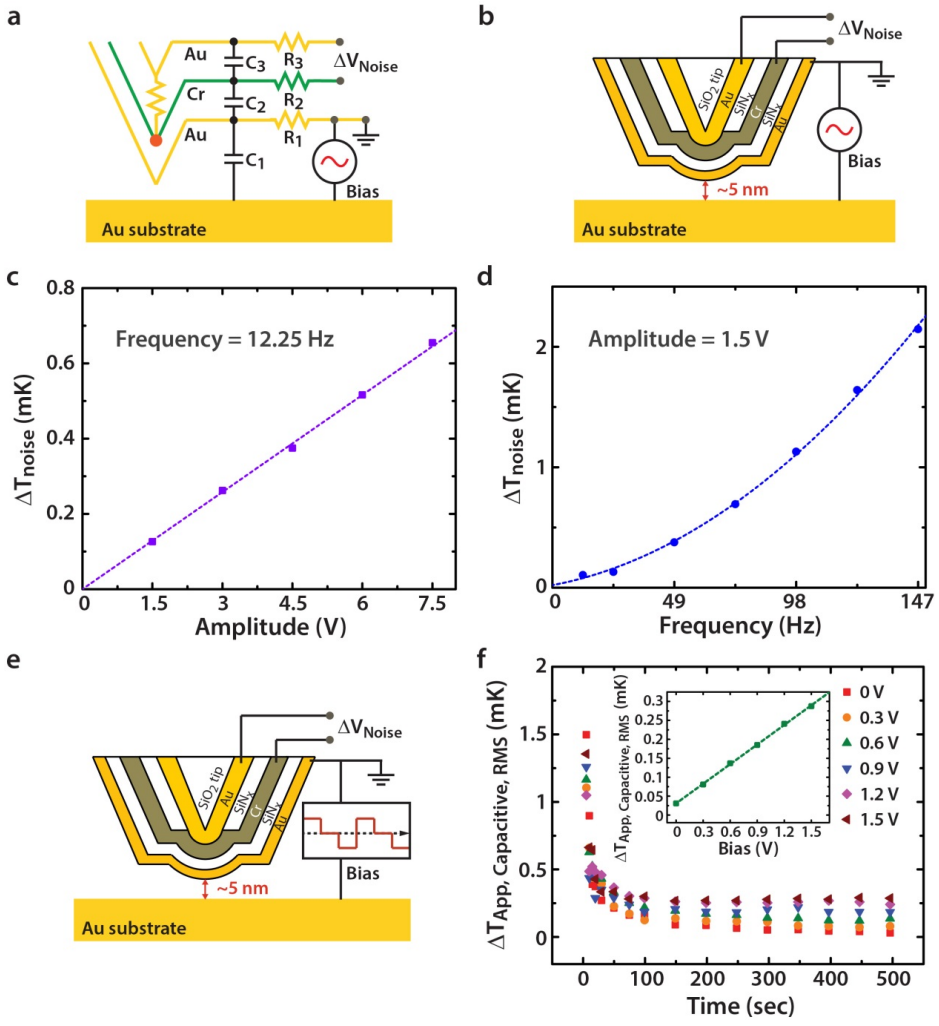

*Figure 4.16 Quantification of the effect of capacitive coupling. (**a**) Schematic of a simplified circuit diagram describing the origin of capacitive coupling. (**b**) Experimental setup to quantify the capacitive coupling: A sinusoidal voltage is applied across the junction. (**c**) Measured amplitude of the voltage output across the thermocouple as the amplitude of the sinusoidal signal (12.25 Hz) is increased. (**d**) Measured amplitude of the voltage output across the thermocouple as the frequency of the sinusoidal signal is increased while keeping the amplitude fixed at 1.5 V. (**e**) Experimental setup to quantify the capacitive coupling when a three level modulation scheme is used. (**f**) Measured RMS temperature noise as a function of the total time of the measurement for various voltage biases (0 V – 1.5 V). The inset shows the measured RMS temperature noise as a function of the amplitude of modulation voltages for 500 seconds long measurements.*

4.4.6.4 *Quantification of the Statistical Variations in $\Delta T_{TC,Avg}(+V_M)$ and $\Delta T_{TC,Avg}(-V_M)$ due to Fluctuations in the Microscopic Characteristics of Atomic-scale Junctions*

The overall uncertainty in the reported temperature rise shown in Figure 4.2, Figure 4.3, and Figure 4.4 arises from electronic noise, capacitive coupling and stochastic fluctuations in the transmission characteristics of molecular junctions. The contributions of the electronic noise and capacitive coupling have been quantified above. Here, we discuss the variations introduced by stochastic fluctuations on the measured $\Delta T_{TC,Avg}(+V_M)$ and $\Delta T_{TC,Avg}(-V_M)$.

As described earlier, the heat dissipation per unit time in the left electrode of the junction $(Q_L(V))$ is given by:

$$Q_L(V) = \frac{2}{h}\int_{-\infty}^{\infty}(\mu_L - E)\tau(E,V)[f(E,\mu_L) - f(E,\mu_R)]dE \tag{4.8}$$

Further, a similar expression can be obtained for the power dissipation in the right electrode $(Q_R(V))$. However, in the experiments the power dissipated in each of the electrodes fluctuates due to the microscopic variations in the junctions. Specifically, since the transmission function $\tau(E,V,t)$ is time dependent (due to variations in junction geometry) the instantaneous power dissipation given by:

$$Q_L(V,t) = \frac{2}{h}\int_{-\infty}^{\infty}(\mu_L - E)\tau(E,V,t)[f(E,\mu_L) - f(E,\mu_R)]dE \tag{4.9}$$

The effect of stochastic fluctuations can be quantified by considering a series of experiments where the heat dissipation in molecular junctions is studied using a

modulation scheme for a time period of $2\tilde{T}$ seconds in each of the experiments. Even if the amplitude of the modulation scheme (V_M) is kept constant to ensure that the averaged total power dissipation is the same in each experiment the averaged power dissipation in any given electrode can vary from one experiment to another due to fluctuations in the transmission characteristics. This, in turn, results in fluctuations in the measured $\Delta T_{TC,Avg}(+V_M)$ and $\Delta T_{TC,Avg}(-V_M)$ from one experiment to another.

In order to quantify these fluctuations, we reanalyzed the data obtained in the measurements of heat dissipation in AMJs. The 500 s long data corresponding to each of the data points in Figure 4.2b, Figure 4.3b, and Figure 4.4a was split into five equal parts (each 100 s long). Subsequently, we analyzed each of the five sets of data using Eqs. (A1.10) and (A1.15) to obtain five different values of $\Delta T_{TC,\,Avg}$. From these data, we computed the mean and standard deviation of $\Delta T_{TC,\,Avg}$ for positive and negative biases. We note that the mean values obtained in this analysis are identical to the values obtained by analyzing the ~500 s long data as reported in Figure 4.2b, Figure 4.3b, and Figure 4.4a.

The results of this analysis for Au atomic junctions are shown in Figure 4.17a. As can be seen from the data, the standard deviations are imperceptible and are <0.1 mK for Au atomic junctions. The results obtained by analyzing the data for BDNC and BDA junctions are shown in Figure 4.17b & c, respectively. It can be seen from the data that the largest standard deviation for BDNC junctions is ~0.6 mK (for the highest power) and is <0.5 mK for all other data points. Further, for the BDA junctions the standard deviation is <0.4 mK for all the data points. This analysis proves that the statistical

variation in the averaged data is indeed very small enabling us to unambiguously probe the asymmetries in the heat dissipation of AMJs.

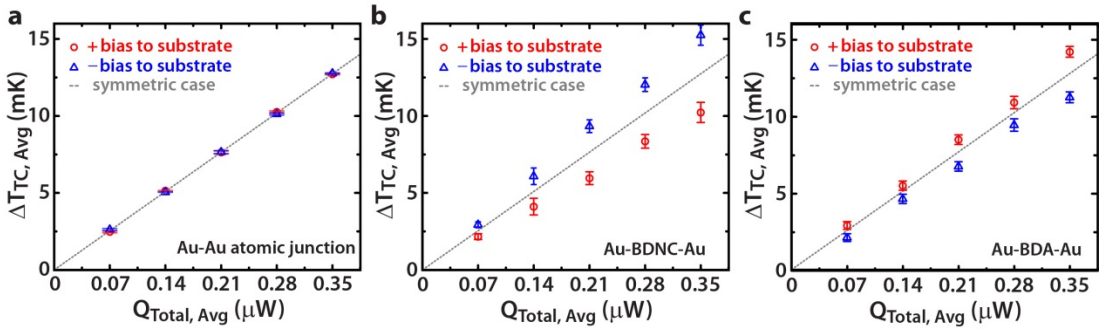

Figure 4.17 Quantification of the variation in the measured $\Delta T_{TC,Avg}$ *due to stochastic fluctuations in the transmission properties of the junctions.* ***(a)*** *Au-Au atomic junctions from Figure 4.4a,* ***(b)*** *Au-BDNC-Au contact from Figure 4.2b, and* ***(c)*** *Au-BDA-Au contact from Figure 4.3b.*

Chapter 5

Conclusions and Future Work

5.1 CONCLUSIONS

Molecular electronics has attracted increasing attention to advance science and technology since unique charge and thermal transport characteristics resulting from quantum mechanical effects are expected [1]. Over the past 40 years or so, advances in experiments and theories in the field of molecular electronics have revealed a deeper understanding of fundamental transport process at the molecular and atomic length scale [6]. Molecular electronics has also demonstrated functions of electronic components such as the switch, rectifier, and transistor made out of single-molecule, and holds great potential for next generation of technological applications [2].

While initial significant advances have been made in understanding charge transport in atomic-scale junctions, our understanding of charge transport properties in such junctions is still at very beginning stage. Further investigations of charge transport properties in atomic-scale junctions are required to better understand the nature of charge transport at molecular and atomic scale. In all charge transport processes, heat dissipation is ubiquitous. Dissipated heat in nanoscale electronics substantially increases the local temperature, which degrades the reliability and performance [158]. Therefore, understanding heat dissipation in atomic-scale junctions is crucial for developing atomic-

scale electronic devices. However, heat dissipation in atomic-scale junctions remains largely unexplored due to the lack of appropriate experimental tools.

This dissertation presents the development of ultra-stable scanning tunneling microscope (STM) and custom-fabricated nanoscale-thermocouple integrated scanning tunneling probes to enable experimental studies of charge transport and heat dissipation in atomic-scale junctions. This dissertation also discusses useful insights obtained from experimental studies of charge transport and heat dissipation in atomic-scale junctions.

I designed and built scanning tunneling microscope (STM) operating at room temperature to stably trap atomic-scale junctions long enough. First, I adapted the Besocke STM design because this design offers the excellent ability to reduce thermal drift. Second, to minimize thermal drift in STM to a greater extent, the STM is placed in a copper enclosure which functions as a radiation shield and the temperature of copper enclosure is actively feedback controlled to maintain at the constant temperature. With the active feedback temperature controller, the temperature variations of the copper enclosure were less than ±1 mK. Third, the effect of ground vibration into STM is minimized by the combination of the two stages: the STM head suspended by custom-made springs (low resonant frequency of ~3 Hz) and the STM piezoelectric scanners (high resonant frequency of >1 kHz). In addition to this two-stage vibration isolation, eddy current damper is integrated into the STM to further improve the stability of STM. Finally, STM is operated under high vacuum to prevent acoustic disturbances into the STM. Using this custom-designed STM, I showed that the duration of trapping single-molecule junctions is several tens of seconds, at least two orders of magnitude more stable than what previous studies have demonstrated [11,49,87].

With the custom-designed STM, I employed scanning tunneling microscope break junction (STMBJ) technique and obtained electrical resistance of single Au-hexanedithiol-Au, Au-octanedithiol-Au, and Au-decanedithiol-Au junctions. I found that electrical resistance of these single-alkanedithiols bridged between gold electrodes exponentially increases with increasing the chain length, suggesting that charge transport mechanism in Au-alkanedithiol-Au junctions is nonresonant tunneling. Experimental results show that tunneling decay constant (β) is 0.99/carbon atoms and is in good agreement with the previous study [99].

I also employed recently introduced transition voltage spectroscopy to approximately estimate the energetic separation between the Fermi level and the closest molecular orbital of Au-alkanedithiol-Au junctions. My experimental results show that the absolute values of transition voltages for Au-hexanedithiol-Au, Au-octanedithiol-Au, and Au-decanedithiol-Au junctions for positive and negative voltage biases are all more or less same, ~1.4 V. Experimental results suggest that the energetic separation between Fermi level and the closest molecular orbital is constant regardless of the length of alkanedithiol moelcules. This data also suggest that the coupling strengths between both gold electrodes and alkanedithiol molecules are identical.

In order to study heat dissipation in atomic-scale junctions, stiff nanoscale-thermocouple integrated scanning tunneling probes have been developed. The tip of probes has three metal layers: two metal layers (Au and Cr) are used to create nanoscale-thermocouple, and third metal layer (Au) is insulated from nanoscale-thermocouple by thin SiN_x film (~70 nm) and is used to form atomic-scale junctions. These probes were designed to be

very stiff by making the cantilever of probes thick (~500 μm) to enable stable trapping of atomic-scale junctions.

Finally, I studied unique heat dissipation characteristics in atomic-scale junctions using custom-fabricated nanoscale-thermocouple integrated scanning tunneling probes. These custom-fabricated probes are employed to create atomic and molecular junctions between gold metal electrodes as well as to measure heat dissipation as charge is transported through these atomic and molecular junctions. With a unique measurement scheme with three-step bias modulation, I studied heat dissipation in Au-Au atomic junctions, Au-Benzenediisonitrile-Au junctions, and Au-Benzenediamine-Au junctions. My results show that if junctions have electrical transmission characteristics that are strongly energy dependent, heat dissipation is asymmetric—that is, unequal between the electrodes—and also dependent on both the bias polarity and the identity of the major charge carriers (electrons versus holes). In contrast, my results show that Au-Au atomic junctions, whose transmission characteristics are weakly energy dependent, do not exhibit appreciable asymmetry in heat dissipation. I also showed that experimental results are in excellent agreement with computational results using both the Landauer model and the electronic transmission function calculated from density functional theory.

5.2 FUTURE WORK

Atomic-scale junctions not only represent the ultimate smallest scale of nanoelectronics but also hold great promise for various technologically important applications such as energy conversion devices. I will describe some interesting research topics related to thermoelectric energy conversion devices based on atomic-scale junctions. Efficient and

inexpensive thermoelectric conversion devices can be realized in the near future by employing unique transport properties of atomic-scale junctions.

5.2.1 Peltier Cooling in Atomic-Scale Junctions

My study on heat dissipation in atomic-scale junctions demonstrated that as charge transports through atomic-scale junctions, both electrodes get heated but the amount of heat dissipation in the two electrodes can be either symmetric or asymmetric depending on the electronic structure of particular atomic-scale junctions. One of the key findings is that heat dissipation in electrodes is asymmetric in molecular junctions where electronic transmission characteristics are strongly dependent on the energy.

In light of this interesting observation, we note that Landauer model suggests that one electrode of atomic-scale junctions can be cooled down below the initial temperature when sufficiently low bias is applied. This indicates that Peltier cooling can be observed at the single-molecule level. In particular, within Landauer theory the heat dissipation in one electrode is expressed by [127]

$$Q = -GTSV + \frac{1}{2}GV^2 + O(V^3). \tag{5.1}$$

Eq. (5.1) suggests that Peltier cooling occurs in the electrode when the applied voltage satisfies the following condition, given by $V < 2TS$, where T is the absolute temperature and S is the Seebeck coefficient of atomic-scale junction. Considering the fact that previous studies have measured the Seebeck coefficient of single-molecule junctions at ~10 $\mu V/K$ at ambient temperature [21,94], voltage should be smaller than ~6 mV to access the Peltier cooling regime at ambient temperature. To roughly estimate the maximum cooling power, I could assume the electrical conductance of single-molecule junctions to

be 0.1 G_0. Then, the estimated maximum cooling power one can obtain is about 35 *pW*, which is too small to measure experimentally.

This interesting refrigeration, one example of thermoelectric energy conversions, in atomic-scale devices can be realized through novel approaches. One possible approach is to design a new type of probe to improve the power resolution for measuring significantly small amounts of cooling. This could be accomplished by increasing the thermal resistance of the probe and employing two dissimilar materials that have large Seebeck coefficients to create the nanoscale-thermocouple located at the end of the tip. Another approach is to engineer the electronic structure of molecular junctions, for example via modifying the molecular structure, such that the Seebeck coefficient and electrical conductance have high values. One prominent theoretical prediction examined by Finch *et al.*[39] suggested that the electronic transmission can be sharply peaked around the chemical potential by rotating the side group. Employing this approach of tuning electronic structures will enable much larger Peltier cooling that can ultimately be utilized to cool down technologically relevant atomic-scale devices.

5.2.2 Thermal conductance measurement of single-molecule junctions

Molecular junctions are one of the promising candidates for thermoelectric energy conversion devices due to their novel transport properties arising from their low dimensional system. The efficiency of thermoelectric devices is related to the figure of merit, *ZT*, defined as $S^2\sigma T/k$, where S is the Seebeck coefficient, σ is the electrical conductivity, k is the thermal conductivity, and T is the absolute temperature. The figure of merit, *ZT*, can also be expressed as $S^2 G_{electrical} T/G_{thermal}$, where $G_{electrical}$ is the electrical conductance and $G_{thermal}$ is the thermal conductance of the device. In order to increase the

efficiency of thermoelectric devices made of molecular junctions, we first need to experimentally measure all transport properties included in figure of merit *ZT* for the characterization. Moreover, measurement of transport properties in single-molecule junctions is desirable to isolate interactions between adjacent molecules and to fundamentally understand transport characteristics of individual single-molecule junctions. Although measurements of electrical conductance and Seebeck coefficient in single-molecule junctions are now possible because novel nanoscale metrology tools and techniques have recently been developed, thermal conductance measurement of single-molecule junctions have not yet been possible because thermal conductance of single-molecule junctions is expected to be very small, in the tens of *pW* range. We aim to measure the thermal conductance of single-molecule junctions with a novel experimental approach that we are currently developing. This thermal conductance measurement will enable the full characterization of the figure of merit of single-molecule junctions, providing significant opportunities to create inexpensive and efficient organic molecule based thermoelectric devices.

Appendix

APPENDIX 1. ANALYSIS OF THE MODULATION SCHEME

A1.1 Noise Reduction due to Time-Averaging

When a DC voltage bias is applied across an atomic-scale junction, the measured voltage across the thermocouple integrated into the probe is given by:

$$V(t) = V_{TC} + V_N(t) \tag{A1.1}$$

where V_{TC} is the thermoelectric voltage resulting from the DC bias applied across the junction, whereas $V_N(t)$ is the voltage noise superimposed on the signal. The signal-to-noise ratio can be improved by obtaining a signal for an extended time $\left[-\tilde{T}, \tilde{T}\right]$ and performing a time-average to obtain the time-averaged signal $\overline{V}$:

$$\overline{V} = \frac{1}{2\tilde{T}} \int_{-\tilde{T}}^{\tilde{T}} \left[V_{TC} + V_N(t)\right] dt = \underbrace{V_{TC}}_{Signal} + \underbrace{\frac{1}{2\tilde{T}} \int_{-\tilde{T}}^{\tilde{T}} V_N(t) dt}_{Noise} \tag{A1.2}$$

The time averaged noise signal $\overline{V}_{noise}$ is given by:

$$\overline{V}_{noise} = \frac{1}{2\tilde{T}} \int_{-\tilde{T}}^{\tilde{T}} V_N(t) dt \,, \tag{A1.3}$$

and tends to zero as $\tilde{T} \to \infty$. It is insightful to rewrite Eq. (A1.3) as follows:

$$\bar{V}_{noise} = \frac{1}{2\tilde{T}} \int_{-\tilde{T}}^{\tilde{T}} \left[\int_{-\infty}^{\infty} V_N(f) e^{i2\pi ft} df \right] dt = \frac{1}{2\tilde{T}} \int_{-\infty}^{\infty} V_N(f) \left[\int_{-\tilde{T}}^{\tilde{T}} e^{i2\pi ft} dt \right] df \,, \qquad \text{(A1.4)}$$

where we have performed a Fourier transformation of $V_N(t)$. This implies that

$$\bar{V}_{noise} = \int_{-\infty}^{\infty} V_N(f) \underbrace{\frac{Sin(2\pi f\tilde{T})}{(2\pi f\tilde{T})}}_{Sinc\ function} df \,. \qquad \text{(A1.5)}$$

Further, it can be shown that the root mean square (RMS) value of the noise voltage ($\left\langle \bar{V}^2_{noise} \right\rangle^{1/2}$) is given by:

$$\left\langle \bar{V}^2_{noise} \right\rangle^{1/2} \sim \left[\int_{-\infty}^{\infty} \tilde{G}_N(f) \left[\frac{Sin(2\pi f\tilde{T})}{(2\pi f\tilde{T})} \right]^2 df \right]^{1/2} = \left[\int_{0}^{\infty} G_N(f) \left[\frac{Sin(2\pi f\tilde{T})}{(2\pi f\tilde{T})} \right]^2 df \right]^{1/2} , \text{ (A1.6)}$$

where $\tilde{G}_N(f)$ and $G_N(f)$ are the two-sided and one sided power spectral densities, respectively, of $V_N(t)$. Since the Sinc function in Eq. (A1.6) has an appreciable magnitude only in a narrow band of frequencies, $\sim \left[-\frac{1}{2\tilde{T}}, \frac{1}{2\tilde{T}} \right]$, it is clear that time averaging is equivalent to reducing the bandwidth to a narrow band of frequencies centered at 0 Hz. In general, 1/*f* noise has large contributions at low frequencies, therefore, it is desirable to develop a scheme where further attenuation is achieved at low frequencies enabling additional attenuation in $\left\langle \bar{V}^2_{noise} \right\rangle^{1/2}$. Next, we describe how the three level modulation scheme described above accomplishes this goal.

A1.2 Noise Reduction in the Modulation Scheme

A three level modulation signal $V_M(t)$, shown in Figure 4.5, which features a periodic series of voltages at $+V_M$, 0 V, and $-V_M$ is applied across the AMJs for an extended period of time ($2\tilde{T}$). The applied voltage results in a modulated electrical current $I_M(t)$ (Figure 4.5b) as well as a modulated temperature rise in the thermocouple $\Delta T_{M,\,TC}(t)$, which in turn results in a thermoelectric voltage output $\Delta V_{M,\,TC}(t)$ as shown in Figure 4.5c. In general, the voltage signal ($V(t)$) recorded from the nanoscale thermocouple integrated into the probe is given by:

$$V(t) = \Delta V_{M,\,TC}(t) + V_N(t) \tag{A1.7}$$

where $V_N(t)$ is a noise signal superimposed on the desired signal $\Delta V_{M,\,TC}(t)$.

In order to quantify the amplitude of the thermoelectric signal (and thus the temperature rise of the thermocouple) due to an applied bias $+V_M$ we consider the following summation:

$$S_+(V(t)) = \frac{3}{2\tilde{T}}\left[\int_{-\tilde{T}}^{-\tilde{T}+\Delta t} V(t)dt - \int_{-\tilde{T}+\Delta t}^{-\tilde{T}+2\Delta t} V(t)dt + \int_{-\tilde{T}+3\Delta t}^{-\tilde{T}+4\Delta t} V(t)dt - \int_{-\tilde{T}+4\Delta t}^{-\tilde{T}+5\Delta t} V(t)dt + \ldots\ldots + \int_{\tilde{T}-3\Delta t}^{\tilde{T}-2\Delta t} V(t)dt - \int_{\tilde{T}-2\Delta t}^{\tilde{T}-\Delta t} V(t)dt\right] \tag{A1.8}$$

where, $2\tilde{T}$ is total time of the signal and $3N\Delta t = 2\tilde{T}$. Eq. (A1.8) can be written as:

$$S_+(V) = S_+(V_{M,\,TC}) + S_+(V_N) \tag{A1.9}$$

It can be easily shown that $\Delta T_{TC,Avg}(+V_M)$ is related to $S_+(V_{M,\,TC})$ by:

$$S_+(V_{M,\,TC}) = S_{TC} \times \Delta T_{TC,Avg}(+V_M) = \frac{3}{2\tilde{T}}\left[A_R - A_G\right] \tag{A1.10}$$

where S_{TC} is the Seebeck coefficient of the thermocouple, $\Delta T_{TC,Avg}(+V_M)$ is the time averaged temperature rise of the thermocouple corresponding to a positive voltage bias $+V_M$, and A_R, A_G are the total areas of the red and green regions in Figure 4.5c. Equation (A1.9) suggests that when measuring $S_+(V_{M,\,TC})$ one has to always contend with ***voltage noise in the modulation scheme*** ($\overline{V}_{noise,\,M} = S_+(V_N)$), which is defined by:

$$\overline{V}_{noise,\,M} = S_+(V_N) = \frac{3}{2\tilde{T}}\left[\int_{-\tilde{T}}^{-\tilde{T}+\Delta t} V_N(t)dt - \int_{-\tilde{T}+\Delta t}^{-\tilde{T}+2\Delta t} V_N(t)dt + ... + \int_{\tilde{T}-3\Delta t}^{\tilde{T}-2\Delta t} V_N(t)dt - \int_{\tilde{T}-2\Delta t}^{\tilde{T}-\Delta t} V_N(t)dt\right]. \quad \text{(A1.11)}$$

In order to simplify this expression we perform a Fourier transform, to obtain:

$$\overline{V}_{noise,\,M} = \frac{3}{2\tilde{T}}\int_{-\infty}^{\infty}\left[V_N(f)df\left(\int_{-\tilde{T}}^{-\tilde{T}+\Delta t} e^{i2\pi ft}dt - \int_{-\tilde{T}+\Delta t}^{-\tilde{T}+2\Delta t} e^{i2\pi ft}dt + ... + \int_{\tilde{T}-3\Delta t}^{\tilde{T}-2\Delta t} e^{i2\pi ft}dt - \int_{\tilde{T}-2\Delta t}^{\tilde{T}-\Delta t} e^{i2\pi ft}dt\right)\right], \quad \text{(A1.12)}$$

which can be simplified after some algebra to obtain the following expression:

$$\overline{V}_{noise,\,M} = 3\int_{-\infty}^{\infty} V_N(f)\left[\frac{Sin(2\pi f\tilde{T})}{(2\pi f\tilde{T})}\right]\times\left[\frac{2Sin(\pi f\Delta t)}{1+2Cos(2\pi f\Delta t)}\right]\times e^{-i(2\pi f)\Delta t}\times e^{-i(\pi/2)}df\,. \quad \text{(A1.13)}$$

Further, it can be shown that the RMS value of the noise voltage ($\left\langle \overline{V}^2_{noise,\,M}\right\rangle^{1/2}$) is given by:

$$\left\langle \overline{V}^2_{noise,\ M} \right\rangle^{1/2} = S_{TC} \times \Delta T_{Noise,\ RMS}(+V_M) \sim \left[\int_{-\infty}^{\infty} \tilde{G}_N(f) \left[\frac{Sin(2\pi f\tilde{T})}{(2\pi f\tilde{T})} \right]^2 \times \left[\frac{6Sin(\pi f \Delta t)}{1+2Cos(2\pi f \Delta t)} \right]^2 df \right]^{1/2}$$

$$= \left[\int_{0}^{\infty} G_N(f) \left[\frac{Sin(2\pi f\tilde{T})}{(2\pi f\tilde{T})} \right]^2 \times \left[\frac{6Sin(\pi f \Delta t)}{1+2Cos(2\pi f \Delta t)} \right]^2 df \right]^{1/2}, \quad \text{(A1.14)}$$

where $\tilde{G}_N(f)$ and $G_N(f)$ are the power spectral densities of $V_N(t)$ as defined earlier and $\Delta T_{Noise,\ RMS}(+V_M)$ is the root mean square value of the noise in the measured temperature.

On comparing Eq. (A1.14) with Eq. (A1.6) it is clear that the difference in the contributions from noise comes primarily from the additional factor $\left[\frac{6Sin(\pi f \Delta t)}{1+2Cos(2\pi f \Delta t)} \right]^2$ that is present in Eq. (A1.14). In order to better illustrate the effect of this term we plot in Figure A1.1 the functions $H_1(f) = \left[\frac{Sin(2\pi f\tilde{T})}{(2\pi f\tilde{T})} \right]^2$, and $H_2(f) = \left[\frac{Sin(2\pi f\tilde{T})}{(2\pi f\tilde{T})} \right]^2 \times \left[\frac{6Sin(\pi f \Delta t)}{1+2Cos(2\pi f \Delta t)} \right]^2$, where $2\tilde{T}$ is chosen to be 500 seconds and Δt is chosen to be 27.2 ms $= 1/(3 \times 12.25$ Hz$)$, so as to correspond well to the experimentally chosen values of $2\tilde{T}$ and Δt.

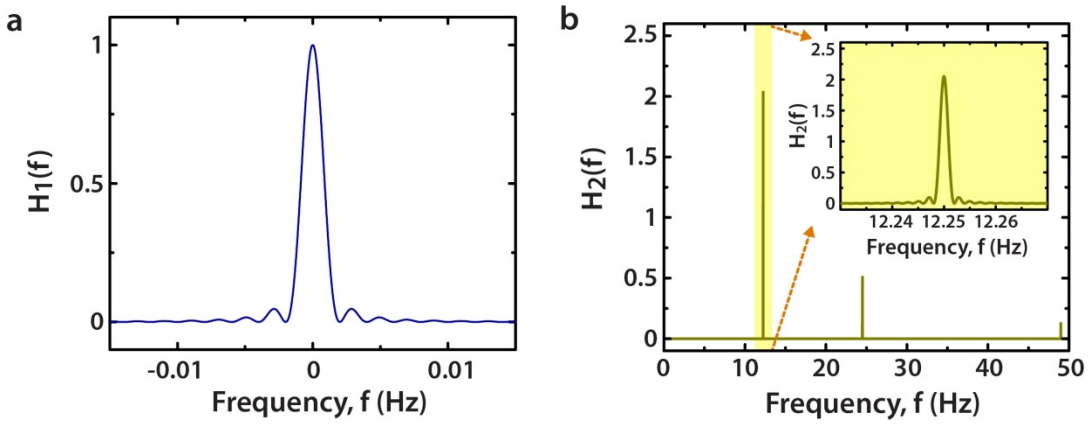

*Figure A1.1 Plots of the functions $H_1(f)$ and $H_2(f)$. (**a**) $H_1(f)$ features a peak at $f = 0$ Hz (**b**) $H_2(f = 0\ Hz) = 0$ enabling significant attenuation of the low frequency contributions in Eq. (A1.14). The inset shows the first peak of $H_2(f)$ which occurs at $f = 12.25$ Hz.*

It can be seen that the function $H_2(f)$ is significantly smaller than the function $H_1(f)$ at low frequencies. As described in the next section, this enables a significant reduction in the root mean square value of the measured noise as the power spectral densities of voltage noise have strong contributions at low frequencies due to *1/f* noise. A similar analysis can be performed to show that the signal to noise ratio can also be improved in the estimation of $\Delta T_{TC,Avg}(-V_M)$: the time averaged temperature rise of the thermocouple corresponding to a negative voltage bias $-V_M$. Finally, we note that $\Delta T_{TC,Avg}(-V_M)$ can be obtained from the following expression:

$$S_{TC} \times \Delta T_{TC,Avg}(-V_M) = \frac{3}{2\tilde{T}}\left[A_B - A_G\right], \tag{A1.15}$$

where A_B and A_G are the total areas of the blue and green regions in Figure 4.5c.

Bibliography

1 Cuevas, J. C. & Scheer, E. *Molecular electronics: an introduction to theory and experiment*. Vol. 1 (World Scientific Publishing Company Incorporated, 2010).

2 Aradhya, S. V. & Venkataraman, L. Single-molecule junctions beyond electronic transport. *Nat Nano* **8**, 399-410, (2013).

3 Tao, N. J. Electron transport in molecular junctions. *Nat Nano* **1**, 173-181, (2006).

4 Ratner, M. A brief history of molecular electronics. *Nat Nano* **8**, 378-381, (2013).

5 Dubi, Y. & Di Ventra, M. Colloquium: Heat flow and thermoelectricity in atomic and molecular junctions. *Reviews of Modern Physics* **83**, 131-155, (2011).

6 Bergfield, J. P. & Ratner, M. A. Forty years of molecular electronics: Non-equilibrium heat and charge transport at the nanoscale. *physica status solidi (b)*, 2249-2266, (2013).

7 Mann, B. & Kuhn, H. Tunneling through Fatty Acid Salt Monolayers. *Journal of Applied Physics* **42**, 4398-4405, (1971).

8 Aviram, A. & Ratner, M. A. Molecular rectifiers. *Chemical Physics Letters* **29**, 277-283, (1974).

9 Binnig, G., Rohrer, H., Gerber, C. & Weibel, E. Tunneling through a controllable vacuum gap. *Appl. Phys. Lett.* **40**, 178-180, (1982).

10 Reed, M. A., Zhou, C., Muller, C. J., Burgin, T. P. & Tour, J. M. Conductance of a Molecular Junction. *Science* **278**, 252-254, (1997).

11 Xu, B. & Tao, N. J. Measurement of Single-Molecule Resistance by Repeated Formation of Molecular Junctions. *Science* **301**, 1221-1223, (2003).

12 Park, H., Park, J., Lim, A. K. L., Anderson, E. H., Alivisatos, A. P. & McEuen, P. L. Nanomechanical oscillations in a single-C60 transistor. *Nature* **407**, 57-60, (2000).

13 Joachim, C., Gimzewski, J. K., Schlittler, R. R. & Chavy, C. Electronic Transparence of a Single C_{60} Molecule. *Physical Review Letters* **74**, 2102-2105, (1995).

14 Wold, D. J. & Frisbie, C. D. Formation of metal-molecule-metal tunnel junctions: Microcontacts to alkanethiol monolayers with a conducting AFM tip. *J. Am. Chem. Soc.* **122**, 2970-2971, (2000).

15 Datta, S. *Electronic Transport in Mesoscopic Systems*. (Cambridge University Press, 1995).

16 Kim, B., Beebe, J. M., Jun, Y., Zhu, X. Y. & Frisbie, C. D. Correlation between HOMO alignment and contact resistance in molecular junctions: Aromatic thiols versus aromatic isocyanides. *J. Am. Chem. Soc.* **128**, 4970-4971, (2006).

17 Beebe, J. M., Kim, B., Gadzuk, J. W., Daniel Frisbie, C. & Kushmerick, J. G. Transition from Direct Tunneling to Field Emission in Metal-Molecule-Metal Junctions. *Physical Review Letters* **97**, 026801, (2006).

18 Tan, A., Sadat, S. & Reddy, P. Measurement of thermopower and current-voltage characteristics of molecular junctions to identify orbital alignment. *Appl. Phys. Lett.* **96**, 013110, (2010).
19 Song, H., Kim, Y., Jeong, H., Reed, M. A. & Lee, T. Coherent tunneling transport in molecular junctions. *Journal of Physical Chemistry C* **114**, 20431-20435, (2010).
20 Song, H., Kim, Y., Jang, Y. H., Jeong, H., Reed, M. A. & Lee, T. Observation of molecular orbital gating. *Nature* **462**, 1039-1043, (2009).
21 Reddy, P., Jang, S.-Y., Segalman, R. A. & Majumdar, A. Thermoelectricity in Molecular Junctions. *Science* **315**, 1568-1571, (2007).
22 Huang, Z., Chen, F., D'Agosta, R., Bennett, P. A., Di Ventra, M. & Tao, N. Local ionic and electron heating in single-molecule junctions. *Nat Nano* **2**, 698-703, (2007).
23 Ioffe, Z., Shamai, T., Ophir, A., Noy, G., Yutsis, I., Kfir, K., Cheshnovsky, O. & Selzer, Y. Detection of heating in current-carrying molecular junctions by Raman scattering. *Nat Nano* **3**, 727-732, (2008).
24 Ward, D. R., Corley, D. A., Tour, J. M. & Natelson, D. Vibrational and electronic heating in nanoscale junctions. *Nat Nano* **6**, 33-38, (2011).
25 Landauer, R. Spatial Variation of Currents and Fields Due to Localized Scatterers in Metallic Conduction. *IBM J. Res. Dev.* **1**, 223-231, (1957).
26 Datta, S. *Quantum Transport: Atom to Transistor*. (Cambridge University Press, 2005).
27 Lee, W., Song, B. & Reddy, P. Measurment of thermoelectric and thermal transport properties of single-molecule junctions. *Annual Review of Heat Transfer* **16**, 259-286, (2013).
28 Nitzan, A. & Ratner, M. A. Electron transport in molecular wire junctions. *Science* **300**, 1384-1389, (2003).
29 Galperin, M., Ratner, M. A., Nitzan, A. & Troisi, A. Nuclear coupling and polarization in molecular transport junctions: Beyond tunneling to function. *Science* **319**, 1056-1060, (2008).
30 Guisinger, N. P., Greene, M. E., Basu, R., Baluch, A. S. & Hersam, M. C. Room temperature negative differential resistance through individual organic molecules on silicon surfaces. *Nano Lett.* **4**, 55-59, (2004).
31 Chen, J., Wang, W., Reed, M. A., Rawlett, A. M., Price, D. W. & Tour, J. M. Room-temperature negative differential resistance in nanoscale molecular junctions. *Appl. Phys. Lett.* **77**, 1224-1226, (2000).
32 Chabinyc, M. L., Chen, X. X., Holmlin, R. E., Jacobs, H., Skulason, H., Frisbie, C. D., Mujica, V., Ratner, M. A., Rampi, M. A. & Whitesides, G. M. Molecular rectification in a metal-insulator-metal junction based on self-assembled monolayers. *Journal of the American Chemical Society* **124**, 11730-11736, (2002).
33 Nijhuis, C. A., Reus, W. F. & Whitesides, G. M. Molecular Rectification in Metal-SAM-Metal Oxide-Metal Junctions. *Journal of the American Chemical Society* **131**, 17814-17827, (2009).

34 Yee, S. K., Sun, J. B., Darancet, P., Tilley, T. D., Majumdar, A., Neaton, J. B. & Segalman, R. A. Inverse Rectification in Donor-Acceptor Molecular Heterojunctions. *Acs Nano* **5**, 9256-9263, (2011).
35 Xu, B. Q., Li, X. L., Xiao, X. Y., Sakaguchi, H. & Tao, N. J. Electromechanical and conductance switching properties of single oligothiophene molecules. *Nano Lett.* **5**, 1491-1495, (2005).
36 Lortscher, E., Ciszek, J. W., Tour, J. & Riel, H. Reversible and controllable switching of a single-molecule junction. *Small* **2**, 973-977, (2006).
37 Bergfield, J. P., Solis, M. A. & Stafford, C. A. Giant Thermoelectric Effect from Transmission Supernodes. *ACS Nano* **4**, 5314-5320, (2010).
38 Bergfield, J. P. & Stafford, C. A. Thermoelectric Signatures of Coherent Transport in Single-Molecule Heterojunctions. *Nano Lett.* **9**, 3072-3076, (2009).
39 Finch, C. M., Garcia-Suarez, V. M. & Lambert, C. J. Giant thermopower and figure of merit in single-molecule devices. *Physical Review B* **79**, (2009).
40 Karlström, O., Linke, H., Karlström, G. & Wacker, A. Increasing thermoelectric performance using coherent transport. *Phys. Rev. B* **84**, 113415, (2011).
41 Macia, E. DNA-based thermoelectric devices: A theoretical prospective. *Physical Review B* **75**, (2007).
42 Chen, G. *Nanoscale energy transport and conversion : a parallel treatment of electrons, molecules, phonons, and photons*. (Oxford University Press, 2005).
43 Malen, J. A., Yee, S. K., Majumdar, A. & Segalman, R. A. Fundamentals of energy transport, energy conversion, and thermal properties in organic-inorganic heterojunctions. *Chemical Physics Letters* **491**, 109-122, (2010).
44 Di Ventra, M. *Electrical transport in nanoscale systems*. (Cambridge University Press, 2008).
45 Xue, Y. Q. & Ratner, M. A. Microscopic study of electrical transport through individual molecules with metallic contacts. I. Band lineup, voltage drop, and high-field transport. *Physical Review B* **68**, (2003).
46 Emberly, E. G. & Kirczenow, G. Molecular spintronics: spin-dependent electron transport in molecular wires. *Chemical Physics* **281**, 311-324, (2002).
47 Rocha, A. R., Garcia-Suarez, V. M., Bailey, S. W., Lambert, C. J., Ferrer, J. & Sanvito, S. Towards molecular spintronics. *Nature Materials* **4**, 335-339, (2005).
48 Tan, A., Balachandran, J., Sadat, S., Gavini, V., Dunietz, B. D., Jang, S. Y. & Reddy, P. Effect of Length and Contact Chemistry on the Electronic Structure and Thermoelectric Properties of Molecular Junctions. *Journal of the American Chemical Society* **133**, 8838-8841, (2011).
49 Venkataraman, L., Klare, J. E., Nuckolls, C., Hybertsen, M. S. & Steigerwald, M. L. Dependence of single-molecule junction conductance on molecular conformation. *Nature* **442**, 904-907, (2006).
50 Yaliraki, S. N., Kemp, M. & Ratner, M. A. Conductance of molecular wires: Influence of molecule-electrode binding. *Journal of the American Chemical Society* **121**, 3428-3434, (1999).
51 Xue, Y. & Ratner, M. A. End group effect on electrical transport through individual molecules: A microscopic study. *Phys. Rev. B* **69**, 085403, (2004).

52 Butcher, P. N. Thermal and Electrical Transport Formalism for Electronic Microstructures with Many Terminals. *J Phys-Condens Mat* **2**, 4869-4878, (1990).
53 Paulsson, M. & Datta, S. Thermoelectric effect in molecular electronics. *Phys Rev B* **67**, 241403, (2003).
54 Esfarjani, K., Zebarjadi, M. & Kawazoe, Y. Thermoelectric properties of a nanocontact made of two-capped single-wall carbon nanotubes calculated within the tight-binding approximation. *Physical Review B* **73**, (2006).
55 Zhang, W., Mingo, N. & Fisher, T. S. Simulation of phonon transport across a non-polar nanowire junction using an atomistic Green's function method. *Physical Review B* **76**, (2007).
56 Ke, S.-H., Yang, W., Curtarolo, S. & Baranger, H. U. Thermopower of Molecular Junctions: An ab Initio Study. *Nano Lett.* **9**, 1011-1014, (2009).
57 Leijnse, M., Wegewijs, M. R. & Flensberg, K. Nonlinear thermoelectric properties of molecular junctions with vibrational coupling. *Physical Review B* **82**, (2010).
58 Nozaki, D., Sevincli, H., Li, W., Gutierrez, R. & Cuniberti, G. Engineering the figure of merit and thermopower in single-molecule devices connected to semiconducting electrodes. *Physical Review B* **81**, (2010).
59 Miroshnichenko, A. E., Flach, S. & Kivshar, Y. S. Fano resonances in nanoscale structures. *Reviews of Modern Physics* **82**, 2257-2298, (2010).
60 Mahan, G. D. & Sofo, J. O. The best thermoelectric. *Proc. Natl. Acad. Sci. U. S. A.* **93**, 7436-7439, (1996).
61 Zhou, Y. & Segal, D. Interface effects in thermal conduction through molecular junctions: Numerical simulations. *J Chem Phys* **133**, (2010).
62 Humphrey, T. E. & Linke, H. Reversible thermoelectric nanomaterials. *Phys Rev Lett* **94**, (2005).
63 Humphrey, T. E., Newbury, R., Taylor, R. P. & Linke, H. Reversible quantum Brownian heat engines for electrons. *Phys Rev Lett* **89**, (2002).
64 Humphrey, T. E., O'Dwyer, M. F. & Linke, H. Power optimization in thermionic devices. *Journal of Physics D-Applied Physics* **38**, 2051-2054, (2005).
65 Nakpathomkun, N., Xu, H. Q. & Linke, H. Thermoelectric efficiency at maximum power in low-dimensional systems. *Physical Review B* **82**, (2010).
66 Curzon, F. L. & Ahlborn, B. Efficiency of a Carnot engine at maximum power output. *American Journal of Physics* **43**, 22-24, (1975).
67 Fermi, E., Pasta, J. & Ulam, S. Studies of non linear problems. *Los Almos Report No. LA1940 (unpublished)*, 978-988, (1955).
68 Lepri, S., Livi, R. & Politi, A. Thermal conduction in classical low-dimensional lattices. *Physics Reports* **377**, 1-80, (2003).
69 Casher, A. & Lebowitz, J. L. Heat Flow in Regular and Disordered Harmonic Chains. *Journal of Mathematical Physics* **12**, 1701-&, (1971).
70 Lepri, S., Livi, R. & Politi, A. Heat conduction in chains of nonlinear oscillators. *Phys Rev Lett* **78**, 1896-1899, (1997).
71 Lepri, S., Livi, R. & Politi, A. On the anomalous thermal conductivity of one-dimensional lattices. *Europhysics Letters* **43**, 271-276, (1998).

72 Segal, D., Nitzan, A. & Hanggi, P. Thermal conductance through molecular wires. *The Journal of Chemical Physics* **119**, 6840-6855, (2003).
73 Galperin, M., Nitzan, A. & Ratner, M. A. Heat conduction in molecular transport junctions. *Phys Rev B* **75**, (2007).
74 Henry, A. & Chen, G. High Thermal Conductivity of Single Polyethylene Chains Using Molecular Dynamics Simulations. *Phys Rev Lett* **101**, (2008).
75 Henry, A. & Chen, G. Anomalous heat conduction in polyethylene chains: Theory and molecular dynamics simulations. *Physical Review B* **79**, (2009).
76 Henry, A., Chen, G., Plimpton, S. J. & Thompson, A. 1D-to-3D transition of phonon heat conduction in polyethylene using molecular dynamics simulations. *Physical Review B* **82**, (2010).
77 Shen, S., Henry, A., Tong, J., Zheng, R. T. & Chen, G. Polyethylene nanofibres with very high thermal conductivities. *Nat Nanotechnol* **5**, 251-255, (2010).
78 Sasikumar, K. & Keblinski, P. Effect of chain conformation in the phonon transport across a Si-polyethylene single-molecule covalent junction. *J Appl Phys* **109**, (2011).
79 Segal, D. & Nitzan, A. Heating in current carrying molecular junctions. *J Chem Phys* **117**, 3915-3927, (2002).
80 Galperin, M., Ratner, M. A. & Nitzan, A. Molecular transport junctions: vibrational effects. *J Phys-Condens Mat* **19**, (2007).
81 Galperin, M., Saito, K., Balatsky, A. V. & Nitzan, A. Cooling mechanisms in molecular conduction junctions. *Phys. Rev. B* **80**, 115427, (2009).
82 Huang, Z., Xu, B., Chen, Y., Di Ventra, M. & Tao, N. Measurement of current-induced local heating in a single molecule junction. *Nano Lett.* **6**, 1240-1244, (2006).
83 Tsutsui, M., Taniguchi, M. & Kawai, T. Local heating in metal-molecule-metal molecule-metal. *Nano Lett.* **8**, 3293-3297, (2008).
84 Schulze, G., Franke, K. J., Gagliardi, A., Romano, G., Lin, C. S., Rosa, A. L., Niehaus, T. A., Frauenheim, T., Di Carlo, A., Pecchia, A. & Pascual, J. I. Resonant Electron Heating and Molecular Phonon Cooling in Single C60 Junctions. *Physical Review Letters* **100**, 136801, (2008).
85 Segal, D. Heat flow in nonlinear molecular junctions: Master equation analysis. *Physical Review B* **73**, (2006).
86 Segal, D. & Nitzan, A. Heat rectification in molecular junctions. *J Chem Phys* **122**, (2005).
87 Jang, S.-Y., Reddy, P., Majumdar, A. & Segalman, R. A. Interpretation of Stochastic Events in Single Molecule Conductance Measurements. *Nano Lett.* **6**, 2362-2367, (2006).
88 Mishchenko, A., Vonlanthen, D., Meded, V., Bürkle, M., Li, C., Pobelov, I. V., Bagrets, A., Viljas, J. K., Pauly, F., Evers, F., Mayor, M. & Wandlowski, T. Influence of Conformation on Conductance of Biphenyl-Dithiol Single-Molecule Contacts. *Nano Lett.* **10**, 156-163, (2009).
89 Lee, W. & Reddy, P. Creation of stable molecular junctions with a custom-designed scanning tunneling microscope. *Nanotechnology* **22**, 485703, (2011).
90 Beebe, J. M., Engelkes, V. B., Miller, L. L. & Frisbie, C. D. Contact Resistance in Metal−Molecule−Metal Junctions Based on Aliphatic SAMs: Effects of Surface

Linker and Metal Work Function. *Journal of the American Chemical Society* **124**, 11268-11269, (2002).
91 Choi, S. H., Kim, B. & Frisbie, C. D. Electrical resistance of long conjugated molecular wires. *Science* **320**, 1482-1486, (2008).
92 Baheti, K., Malen, J. A., Doak, P., Reddy, P., Jang, S.-Y., Tilley, T. D., Majumdar, A. & Segalman, R. A. Probing the Chemistry of Molecular Heterojunctions Using Thermoelectricity. *Nano Lett.* **8**, 715-719, (2008).
93 Malen, J. A., Doak, P., Baheti, K., Tilley, T. D., Majumdar, A. & Segalman, R. A. The Nature of Transport Variations in Molecular Heterojunction Electronics. *Nano Lett.* **9**, 3406-3412, (2009).
94 Malen, J. A., Doak, P., Baheti, K., Tilley, T. D., Segalman, R. A. & Majumdar, A. Identifying the length dependence of orbital alignment and contact coupling in molecular heterojunctions. *Nano Lett* **9**, 1164-1169, (2009).
95 Widawsky, J. R., Darancet, P., Neaton, J. B. & Venkataraman, L. Simultaneous Determination of Conductance and Thermopower of Single Molecule Junctions. *Nano Lett.* **12**, 354-358, (2011).
96 Love, J. C., Estroff, L. A., Kriebel, J. K., Nuzzo, R. G. & Whitesides, G. M. Self-assembled monolayers of thiolates on metals as a form of nanotechnology. *Chemical Reviews* **105**, 1103-1169, (2005).
97 Bohm, D. *Quantum theory*. (Dover Publications, 1989).
98 Shi, L. & Majumdar, A. Thermal Transport Mechanisms at Nanoscale Point Contacts. *Journal of Heat Transfer* **124**, 329-337, (2002).
99 Engelkes, V. B., Beebe, J. M. & Frisbie, C. D. Length-Dependent Transport in Molecular Junctions Based on SAMs of Alkanethiols and Alkanedithiols: Effect of Metal Work Function and Applied Bias on Tunneling Efficiency and Contact Resistance. *Journal of the American Chemical Society* **126**, 14287-14296, (2004).
100 Incropera, F. & DeWitt, D. *Fundamentals of heat and mass transfer*. 6th edn, 10 (WILEY, 2007).
101 Weber, L., Lehr, M. & Gmelin, E. Investigation of the transport properties of gold point contacts. *Physica B* **217**, 181-192, (1996).
102 Wilson, O. M., Hu, X. Y., Cahill, D. G. & Braun, P. V. Colloidal metal particles as probes of nanoscale thermal transport in fluids. *Physical Review B* **66**, (2002).
103 Ge, Z. B., Cahill, D. G. & Braun, P. V. AuPd metal nanoparticles as probes of nanoscale thermal transport in aqueous solution. *Journal of Physical Chemistry B* **108**, 18870-18875, (2004).
104 Ge, Z. B., Cahill, D. G. & Braun, P. V. Thermal conductance of hydrophilic and hydrophobic interfaces. *Phys Rev Lett* **96**, (2006).
105 Wang, Z. H., Carter, J. A., Lagutchev, A., Koh, Y. K., Seong, N. H., Cahill, D. G. & Dlott, D. D. Ultrafast flash thermal conductance of molecular chains. *Science* **317**, 787-790, (2007).
106 Wang, R. Y., Segalman, R. A. & Majumdar, A. Room temperature thermal conductance of alkanedithiol self-assembled monolayers. *Appl. Phys. Lett.* **89**, 3, (2006).
107 Losego, M. D., Grady, M. E., Sottos, N. R., Cahill, D. G. & Braun, P. V. Effects of chemical bonding on heat transport across interfaces. *Nat Mater* **11**, 502-506, (2012).

108 Sperling, L. H. *Introduction to physical polymer science*. 4th edn, (Wiley, 2006).
109 Sadat, S., Chua, Y. J., Lee, W., Ganjeh, Y., Kurabayashi, K., Meyhofer, E. & Reddy, P. Room temperature picowatt-resolution calorimetry. *Appl. Phys. Lett.* **99**, 043106, (2011).
110 Mishchenko, A., Vonlanthen, D., Meded, V., Burkle, M., Li, C., Pobelov, I. V., Bagrets, A., Viljas, J. K., Pauly, F., Evers, F., Mayor, M. & Wandlowski, T. Influence of Conformation on Conductance of Biphenyl-Dithiol Single-Molecule Contacts. *Nano Letters* **10**, 156-163, (2010).
111 van Ruitenbeek, J. M., Smit, R. H. M., Noat, Y., Untiedt, C., Lang, N. D. & van Hemert, M. C. Measurement of the conductance of a hydrogen molecule. *Nature* **419**, 906-909, (2002).
112 Dulic, D., Pump, F., Campidelli, S., Lavie, P., Cuniberti, G. & Filoramo, A. Controlled Stability of Molecular Junctions. *Angewandte Chemie-International Edition* **48**, 8273-8276, (2009).
113 Chen, C. J. *Introduction to scanning tunneling microscopy*. 2nd edn, (Oxford University Press, 2008).
114 Lafferentz, L., Ample, F., Yu, H., Hecht, S., Joachim, C. & Grill, L. Conductance of a Single Conjugated Polymer as a Continuous Function of Its Length. *Science* **323**, 1193-1197, (2009).
115 Besocke, K. An easily operable scanning tunneling microscope. *Surf. Sci.* **181**, 145-153, (1987).
116 Stipe, B. C., Rezaei, M. A. & Ho, W. A variable-temperature scanning tunneling microscope capable of single-molecule vibrational spectroscopy. *Rev. Sci. Instrum.* **70**, 137-143, (1999).
117 Osing, J. & Shvets, I. V. Bulk defects in graphite observed with a scanning tunnelling microscope. *Surf. Sci.* **417**, 145-150, (1998).
118 Hallmark, V. M., Chiang, S., Rabolt, J. F., Swalen, J. D. & Wilson, R. J. Observation of Atomic Corrugation on Au(111) by Scanning Tunneling Microscopy. *Physical Review Letters* **59**, 2879, (1987).
119 Hegner, M., Wagner, P. & Semenza, G. Ultralarge atomically flat template-stripped Au surfaces for scanning probe microscopy. *Surf. Sci.* **291**, 39-46, (1993).
120 Tsutsui, M., Shoji, K., Morimoto, K., Taniguchi, M. & Kawai, T. Thermodynamic stability of single molecule junctions. *Appl. Phys. Lett.* **92**, 223110, (2008).
121 Beebe, J. M., Kim, B., Frisbie, C. D. & Kushmerick, J. G. Measuring relative barrier heights in molecular electronic junctions with transition voltage spectroscopy. *ACS Nano* **2**, 827-832, (2008).
122 Huisman, E. H., Guedon, C. M., van Wees, B. J. & van der Molen, S. J. Interpretation of Transition Voltage Spectroscopy. *Nano Letters* **9**, 3909-3913, (2009).
123 Mirjani, F., Thijssen, J. M. & van der Molen, S. J. Advantages and limitations of transition voltage spectroscopy: A theoretical analysis. *Physical Review B* **84**, 115402, (2011).

124 Araidai, M. & Tsukada, M. Theoretical calculations of electron transport in molecular junctions: Inflection behavior in Fowler-Nordheim plot and its origin. *Physical Review B* **81**, 235114.
125 Chen, J. Z., Markussen, T. & Thygesen, K. S. Quantifying transition voltage spectroscopy of molecular junctions: Ab initio calculations. *Physical Review B* **82**, (2010).
126 *CRC Handbook of Chemistry and Physics*, <http://www.hbcpnetbase.com> (2010-2011).
127 Lee, W., Kim, K., Jeong, W., Zotti, L. A., Pauly, F., Cuevas, J. C. & Reddy, P. Heat dissipation in atomic-scale junctions. *Nature* **498**, 209-212, (2013).
128 Scheer, E., Agrait, N., Cuevas, J. C., Yeyati, A. L., Ludoph, B., Martin-Rodero, A., Bollinger, G. R., van Ruitenbeek, J. M. & Urbina, C. The signature of chemical valence in the electrical conduction through a single-atom contact. *Nature* **394**, 154-157, (1998).
129 Ludoph, B. & van Ruitenbeek, J. M. Thermopower of atomic-size metallic contacts. *Phys Rev B* **59**, 12290-12293, (1999).
130 Li, N. B., Ren, J., Wang, L., Zhang, G., Hanggi, P. & Li, B. W. Colloquium: Phononics: Manipulating heat flow with electronic analogs and beyond. *Rev. Mod. Phys.* **84**, 1045-1066, (2012).
131 Agraït, N., Untiedt, C., Rubio-Bollinger, G. & Vieira, S. Onset of energy dissipation in ballistic atomic wires. *Phys Rev Lett* **88**, 216803-216806, (2002).
132 Kim, Y., Pietsch, T., Erbe, A., Belzig, W. & Scheer, E. Benzenedithiol: A broad-range single-channel molecular conductor. *Nano Lett* **11**, 3734-3738, (2011).
133 Kiguchi, M., Miura, S., Hara, K., Sawamura, M. & Murakoshi, K. Conductance of a single molecule anchored by an isocyanide substituent to gold electrodes. *Appl. Phys. Lett.* **89**, 213104, (2006).
134 Sivan, U. & Imry, Y. Multichannel Landauer formula for thermoelectric transport with application to thermopower near the mobility edge. *Phys. Rev. B* **33**, 551-558, (1986).
135 Pauly, F., Viljas, J. K., Huniar, U., Häfner, M., Wohlthat, S., Bürkle, M., Cuevas, J. C. & Schön, G. Cluster-based density-functional approach to quantum transport through molecular and atomic contacts. *New Journal of Physics* **10**, 125019, (2008).
136 Venkataraman, L., Klare, J. E., Tam, I. W., Nuckolls, C., Hybertsen, M. S. & Steigerwald, M. L. Single-molecule circuits with well-defined molecular conductance. *Nano Lett* **6**, 458-462, (2006).
137 Brandbyge, M., Schiotz, J., Sorensen, M. R., Stoltze, P., Jacobsen, K. W., Norskov, J. K., Olesen, L., Laegsgaard, E., Stensgaard, I. & Besenbacher, F. Quantized conductance in atom-sized wires between two metals. *Phys Rev B* **52**, 8499-8514, (1995).
138 Nielsen, S. K., Brandbyge, M., Hansen, K., Stokbro, K., van Ruitenbeek, J. M. & Besenbacher, F. Current-Voltage Curves of Atomic-Sized Transition Metal Contacts: An Explanation of Why Au is Ohmic and Pt is Not. *Physical Review Letters* **89**, 066804, (2002).
139 Tsutsui, M., Kawai, T. & Taniguchi, M. Unsymmetrical hot electron heating in quasi-ballistic nanocontacts. *Nat. Sci. Rep.* **2**, 217, (2012).

140 Kim, K., Jeong, W., Lee, W. & Reddy, P. Ultra-High Vacuum Scanning Thermal Microscopy for Nanometer Resolution Quantitative Thermometry. *ACS Nano* **6**, 4248-4257, (2012).
141 Taylor, J., Brandbyge, M. & Stokbro, K. Theory of Rectification in Tour Wires: The Role of Electrode Coupling. *Physical Review Letters* **89**, 138301, (2002).
142 Ahlrichs, R., Bär, M., Häser, M., Horn, H. & Kölmel, C. Electronic-structure calculations on workstation computers - the program system turbomole. *Chem Phys Lett* **162**, 165-169, (1989).
143 Perdew, J. P. Density-functional approximation for the correlation-energy of the inhomogeneous electron-gas. *Phys Rev B* **33**, 8822-8824, (1986).
144 Schäfer, A., Horn, H. & Ahlrichs, R. Fully optimized contracted Gaussian basis sets for atoms Li to Kr. *J Chem Phys* **97**, 2571-2577, (1992).
145 Ward, D. R., Huser, F., Pauly, F., Cuevas, J. C. & Natelson, D. Optical rectification and field enhancement in a plasmonic nanogap. *Nat Nano* **5**, 732-736, (2010).
146 Gilman, Y., Allen, P. B. & Hybertsen, M. S. Density-functional study of adsorption of isocyanides on a gold(111) surface. *J Phys Chem C* **112**, 3314-3320, (2008).
147 Dahlke, R. & Schollwöck, U. Electronic transport calculations for self-assembled monolayers of 1,4-phenylene diisocyanide on Au(111) contacts. *Phys Rev B* **69**, 085324, (2004).
148 Zotti, L. A., Bürkle, M., Pauly, F., Lee, W., Kim, K., Jeong, W., Asai, Y., Reddy, P. & Cuevas, J. C. Heat dissipation and its relation to thermopower in single-molecule junctions. *New Journal of Physics* **16**, 015004, (2014).
149 Quek, S. Y., Venkataraman, L., Choi, H. J., Louie, S. G., Hybertsen, M. S. & Neaton, J. B. Amine-gold linked single-molecule circuits: Experiment and theory. *Nano Lett* **7**, 3477-3482, (2007).
150 Li, Z. & Kosov, D. S. Nature of well-defined conductance of amine-anchored molecular junctions: Density functional calculations. *Phys Rev B* **76**, 035415, (2007).
151 Strange, M., Rostgaard, C., Häkkinen, H. & Thygesen, K. S. Self-consistent GW calculations of electronic transport in thiol- and amine-linked molecular junctions. *Phys Rev B* **83**, 115108, (2011).
152 Roh, H. H., Lee, J. S., Kim, D. L., Park, J., Kim, K., Kwon, O., Park, S. H., Choi, Y. K. & Majumdar, A. Novel nanoscale thermal property imaging technique: The 2ω method. I. Principle and the 2ω signal measurement. *Journal of Vacuum Science & Technology B* **24**, 2398-2404, (2006).
153 Sergueev, N., Shin, S., Kaviany, M. & Dunietz, B. Efficiency of thermoelectric energy conversion in biphenyl-dithiol junctions: Effect of electron-phonon interactions. *Phys Rev B* **83**, 195415, (2011).
154 Ziman, J. M. *Principles of the theory of solids*. 2d edn, (University Press, 1972).
155 Zhou, F., Persson, A., Samuelson, L., Linke, H. & Shi, L. Thermal resistance of a nanoscale point contact to an indium arsenide nanowire. *Appl. Phys. Lett.* **99**, 063110, (2011).
156 Shen, S., Mavrokefalos, A., Sambegoro, P. & Chen, G. Nanoscale thermal radiation between two gold surfaces. *Appl. Phys. Lett.* **100**, 233114, (2012).

157 Ott, H. W. *Noise reduction techniques in electronic systems*. 2nd edn, (Wiley, 1988).
158 Pop, E. Energy dissipation and transport in nanoscale devices. *Nano Res.* **3**, 147-169, (2010).